THE THIRD CATALOG OF ACTIVE GALACTIC NUCLEI DETECTED
BY THE *FERMI* LARGE AREA TELESCOPE

M. ACKERMANN[1], M. AJELLO[2], W. B. ATWOOD[3], L. BALDINI[4], J. BALLET[5], G. BARBIELLINI[6,7], D. BASTIERI[8,9],
J. BECERRA GONZALEZ[10,11], R. BELLAZZINI[12], E. BISSALDI[13], R. D. BLANDFORD[14], E. D. BLOOM[14], R. BONINO[15,16],
E. BOTTACINI[14], T. J. BRANDT[10], J. BREGEON[17], R. J. BRITTO[18], P. BRUEL[19], R. BUEHLER[1], S. BUSON[8,9], G. A. CALIANDRO[14,20],
R. A. CAMERON[14], M. CARAGIULO[13], P. A. CARAVEO[21], B. CARPENTER[10,22], J. M. CASANDJIAN[5], E. CAVAZZUTI[23], C. CECCHI[24,25],
E. CHARLES[14], A. CHEKHTMAN[26], C. C. CHEUNG[27], J. CHIANG[14], G. CHIARO[9], S. CIPRINI[23,24,28], R. CLAUS[14], J. COHEN-TANUGI[17],
L. R. COMINSKY[29], J. CONRAD[30,31,32,70], S. CUTINI[23,24,28], R. D'ABRUSCO[33], F. D'AMMANDO[34,35], A. DE ANGELIS[36],
R. DESIANTE[6,37], S. W. DIGEL[14], L. DI VENERE[38], P. S. DRELL[14], C. FAVUZZI[13,38], S. J. FEGAN[19], E. C. FERRARA[10], J. FINKE[27],
W. B. FOCKE[14], A. FRANCKOWIAK[14], L. FUHRMANN[39], Y. FUKAZAWA[40], A. K. FURNISS[14], P. FUSCO[13,38], F. GARGANO[13],
D. GASPARRINI[23,24,28], N. GIGLIETTO[13,38], P. GIOMMI[23], F. GIORDANO[13,38], M. GIROLETTI[34], T. GLANZMAN[14], G. GODFREY[14],
I. A. GRENIER[5], J. E. GROVE[27], S. GUIRIEC[10,2,71], J. W. HEWITT[41,42], A. B. HILL[14,43,68], D. HORAN[19], R. ITOH[40],
G. JÓHANNESSON[44], A. S. JOHNSON[14], W. N. JOHNSON[27], J. KATAOKA[45], T. KAWANO[40], F. KRAUSS[46], M. KUSS[12], G. LA MURA[9,47],
S. LARSSON[30,31,48], L. LATRONICO[15], C. LETO[49], J. LI[50], L. LI[31,51], F. LONGO[6,7], F. LOPARCO[13,38], B. LOTT[52], M. N. LOVELLETTE[27],
P. LUBRANO[24,25], G. M. MADEJSKI[14], M. MAYER[1], M. N. MAZZIOTTA[13], J. E. MCENERY[10,11], P. F. MICHELSON[14], T. MIZUNO[53],
A. A. MOISEEV[11,42], M. E. MONZANI[14], A. MORSELLI[54], I. V. MOSKALENKO[14], S. MURGIA[55], E. NUSS[17], M. OHNO[40], T. OHSUGI[53],
R. OJHA[10], N. OMODEI[14], M. ORIENTI[34], E. ORLANDO[14], A. PAGGI[33], D. PANEQUE[14,56], J. S. PERKINS[10], M. PESCE-ROLLINS[12],
F. PIRON[17], G. PIVATO[12], T. A. PORTER[14], S. RAINÒ[13,38], R. RANDO[8,9], M. RAZZANO[12,69], S. RAZZAQUE[18], A. REIMER[14,47],
O. REIMER[14,47], R. W. ROMANI[14], D. SALVETTI[21], M. SCHAAL[57], F. K. SCHINZEL[58], A. SCHULZ[1], C. SGRÒ[12], E. J. SISKIND[59],
K. V. SOKOLOVSKY[39,60], F. SPADA[12], G. SPANDRE[12], P. SPINELLI[13,38], L. STAWARZ[61,62], D. J. SUSON[63], H. TAKAHASHI[40],
T. TAKAHASHI[61], Y. TANAKA[53], J. G. THAYER[14], J. B. THAYER[14], L. TIBALDO[14], D. F. TORRES[50,64], E. TORRESI[65], G. TOSTI[24,25],
E. TROJA[10,11], Y. UCHIYAMA[66], G. VIANELLO[14], B. L. WINER[67], K. S. WOOD[27], AND S. ZIMMER[30,31]

[1] Deutsches Elektronen Synchrotron DESY, D-15738 Zeuthen, Germany
[2] Department of Physics and Astronomy, Clemson University, Kinard Lab of Physics, Clemson, SC 29634-0978, USA
[3] Santa Cruz Institute for Particle Physics, Department of Physics and Department of Astronomy and Astrophysics, University of California at Santa Cruz, Santa Cruz, CA 95064, USA
[4] Università di Pisa and Istituto Nazionale di Fisica Nucleare, Sezione di Pisa I-56127 Pisa, Italy
[5] Laboratoire AIM, CEA-IRFU/CNRS/Université Paris Diderot, Service d'Astrophysique, CEA Saclay, F-91191 Gif sur Yvette, France
[6] Istituto Nazionale di Fisica Nucleare, Sezione di Trieste, I-34127 Trieste, Italy
[7] Dipartimento di Fisica, Università di Trieste, I-34127 Trieste, Italy
[8] Istituto Nazionale di Fisica Nucleare, Sezione di Padova, I-35131 Padova, Italy
[9] Dipartimento di Fisica e Astronomia "G. Galilei," Università di Padova, I-35131 Padova, Italy
[10] NASA Goddard Space Flight Center, Greenbelt, MD 20771, USA
[11] Department of Physics and Department of Astronomy, University of Maryland, College Park, MD 20742, USA
[12] Istituto Nazionale di Fisica Nucleare, Sezione di Pisa, I-56127 Pisa, Italy
[13] Istituto Nazionale di Fisica Nucleare, Sezione di Bari, I-70126 Bari, Italy
[14] W. W. Hansen Experimental Physics Laboratory, Kavli Institute for Particle Astrophysics and Cosmology, Department of Physics and SLAC National Accelerator Laboratory, Stanford University, Stanford, CA 94305, USA
[15] Istituto Nazionale di Fisica Nucleare, Sezione di Torino, I-10125 Torino, Italy
[16] Dipartimento di Fisica Generale "Amadeo Avogadro," Università degli Studi di Torino, I-10125 Torino, Italy
[17] Laboratoire Univers et Particules de Montpellier, Université Montpellier, CNRS/IN2P3, Montpellier, France
[18] Department of Physics, University of Johannesburg, P. O. Box 524, Auckland Park 2006, South Africa
[19] Laboratoire Leprince-Ringuet, École polytechnique, CNRS/IN2P3, Palaiseau, France
[20] Consorzio Interuniversitario per la Fisica Spaziale (CIFS), I-10133 Torino, Italy
[21] INAF-Istituto di Astrofisica Spaziale e Fisica Cosmica, I-20133 Milano, Italy
[22] Catholic University of America, Washington, DC 20064, USA
[23] Agenzia Spaziale Italiana (ASI) Science Data Center, I-00133 Roma, Italy; elisabetta.cavazzuti@asdc.asi.it, stefano.ciprini@asdc.asi.it, sara.cutini@asdc.asi.it, gasparrini@asdc.asi.it
[24] Istituto Nazionale di Fisica Nucleare, Sezione di Perugia, I-06123 Perugia, Italy
[25] Dipartimento di Fisica, Università degli Studi di Perugia, I-06123 Perugia, Italy
[26] College of Science, George Mason University, Fairfax, VA 22030, Resident at Naval Research Laboratory, Washington, DC 20375, USA
[27] Space Science Division, Naval Research Laboratory, Washington, DC 20375-5352, USA
[28] INAF Osservatorio Astronomico di Roma, I-00040 Monte Porzio Catone (Roma), Italy
[29] Department of Physics and Astronomy, Sonoma State University, Rohnert Park, CA 94928-3609, USA
[30] Department of Physics, Stockholm University, AlbaNova, SE-106 91 Stockholm, Sweden
[31] The Oskar Klein Centre for Cosmoparticle Physics, AlbaNova, SE-106 91 Stockholm, Sweden
[32] The Royal Swedish Academy of Sciences, Box 50005, SE-104 05 Stockholm, Sweden
[33] Harvard-Smithsonian Center for Astrophysics, Cambridge, MA 02138, USA
[34] INAF Istituto di Radioastronomia, I-40129 Bologna, Italy
[35] Dipartimento di Astronomia, Università di Bologna, I-40127 Bologna, Italy
[36] Dipartimento di Fisica, Università di Udine and Istituto Nazionale di Fisica Nucleare, Sezione di Trieste, Gruppo Collegato di Udine, I-33100 Udine, Italy
[37] Università di Udine, I-33100 Udine, Italy
[38] Dipartimento di Fisica "M. Merlin" dell'Università e del Politecnico di Bari, I-70126 Bari, Italy
[39] Max-Planck-Institut für Radioastronomie, Auf dem Hügel 69, D-53121 Bonn, Germany
[40] Department of Physical Sciences, Hiroshima University, Higashi-Hiroshima, Hiroshima 739-8526, Japan
[41] Department of Physics and Center for Space Sciences and Technology, University of Maryland Baltimore County, Baltimore, MD 21250, USA

1

[42] Center for Research and Exploration in Space Science and Technology (CRESST) and NASA Goddard Space Flight Center, Greenbelt, MD 20771, USA
[43] School of Physics and Astronomy, University of Southampton, Highfield, Southampton, SO17 1BJ, UK
[44] Science Institute, University of Iceland, IS-107 Reykjavik, Iceland
[45] Research Institute for Science and Engineering, Waseda University, 3-4-1, Okubo, Shinjuku, Tokyo 169-8555, Japan
[46] Dr. Remeis-Sternwarte Bamberg, Sternwartstrasse 7, D-96049 Bamberg, Germany
[47] Institut für Astro- und Teilchenphysik and Institut für Theoretische Physik, Leopold-Franzens-Universität Innsbruck, A-6020 Innsbruck, Austria
[48] Department of Astronomy, Stockholm University, SE-106 91 Stockholm, Sweden
[49] ASI Science Data Center, I-00044 Frascati (Roma), Italy
[50] Institute of Space Sciences (IEEC-CSIC), Campus UAB, E-08193 Barcelona, Spain
[51] Department of Physics, KTH Royal Institute of Technology, AlbaNova, SE-106 91 Stockholm, Sweden
[52] Univ. Bordeaux, Centre d'Études Nucléaires de Bordeaux Gradignan, IN2P3/CNRS, BP120, F-33175 Gradignan Cedex, France; lott@cenbg.in2p3.fr
[53] Hiroshima Astrophysical Science Center, Hiroshima University, Higashi-Hiroshima, Hiroshima 739-8526, Japan
[54] Istituto Nazionale di Fisica Nucleare, Sezione di Roma "Tor Vergata," I-00133 Roma, Italy
[55] Center for Cosmology, Physics and Astronomy Department, University of California, Irvine, CA 92697-2575, USA
[56] Max-Planck-Institut für Physik, D-80805 München, Germany
[57] National Research Council Research Associate, National Academy of Sciences, Washington, DC 20001, resident at Naval Research Laboratory, Washington, DC 20375, USA
[58] University of New Mexico, MSC07 4220, Albuquerque, NM 87131, USA
[59] NYCB Real-Time Computing Inc., Lattingtown, NY 11560-1025, USA
[60] Astro Space Center of the Lebedev Physical Institute, 117810 Moscow, Russia
[61] Institute of Space and Astronautical Science, Japan Aerospace Exploration Agency, 3-1-1 Yoshinodai, Chuo-ku, Sagamihara, Kanagawa 252-5210, Japan
[62] Astronomical Observatory, Jagiellonian University, 30-244 Kraków, Poland
[63] Department of Chemistry and Physics, Purdue University Calumet, Hammond, IN 46323-2094, USA
[64] Institució Catalana de Recerca i Estudis Avançats (ICREA), Barcelona, Spain
[65] INAF-IASF Bologna, I-40129 Bologna, Italy
[66] 3-34-1 Nishi-Ikebukuro, Toshima-ku, Tokyo 171-8501, Japan
[67] Department of Physics, Center for Cosmology and Astro-Particle Physics, The Ohio State University, Columbus, OH 43210, USA

ABSTRACT

The third catalog of active galactic nuclei (AGNs) detected by the *Fermi*-LAT (3LAC) is presented. It is based on the third *Fermi*-LAT catalog (3FGL) of sources detected between 100 MeV and 300 GeV with a Test Statistic greater than 25, between 2008 August 4 and 2012 July 31. The 3LAC includes 1591 AGNs located at high Galactic latitudes ($|b| > 10°$), a 71% increase over the second catalog based on 2 years of data. There are 28 duplicate associations, thus 1563 of the 2192 high-latitude gamma-ray sources of the 3FGL catalog are AGNs. Most of them (98%) are blazars. About half of the newly detected blazars are of unknown type, i.e., they lack spectroscopic information of sufficient quality to determine the strength of their emission lines. Based on their gamma-ray spectral properties, these sources are evenly split between flat-spectrum radio quasars (FSRQs) and BL Lacs. The most abundant detected BL Lacs are of the high-synchrotron-peaked (HSP) type. About 50% of the BL Lacs have no measured redshifts. A few new rare outliers (HSP-FSRQs and high-luminosity HSP BL Lacs) are reported. The general properties of the 3LAC sample confirm previous findings from earlier catalogs. The fraction of 3LAC blazars in the total population of blazars listed in BZCAT remains non-negligible even at the faint ends of the BZCAT-blazar radio, optical, and X-ray flux distributions, which hints that even the faintest known blazars could eventually shine in gamma-rays at LAT-detection levels. The energy-flux distributions of the different blazar populations are in good agreement with extrapolation from earlier catalogs.

Key words: BL Lacertae objects: general – galaxies: active – galaxies: jets – gamma rays: galaxies

Supporting material: machine-readable tables

1. INTRODUCTION

Since its launch in 2008, the *Fermi*-LAT has revolutionized our knowledge of the gamma-ray sky above 100 MeV. Its unique combination of high sensitivity, wide field of view, large energy range, and a nominal sky-survey operating mode has enabled a complete mapping and continuous monitoring of the gamma-ray sky to an unprecedented level. Several catalogs or source lists, both general and specialized (active galactic nuclei; AGNs, pulsars, supernova remnants, pulsar wind nebulae, gamma-ray bursts, very-high-energy (VHE) candidates) have already been produced. These constitute important resources to the astronomical community. The successive AGN lists and catalogs, LAT Bright AGN Sample (LBAS; Abdo et al. 2009a), 1LAC (Abdo et al. 2010g) and 2LAC (Ackermann et al. 2011c, 2015), first and second LAT AGN catalogs, respectively, have triggered numerous population studies (e.g., Ghisellini et al. 2009, 2012, 2013; Ajello et al. 2012; D'Abrusco et al. 2012; Massaro et al. 2012; Meyer et al. 2012; Padovani et al. 2012; Finke 2013; Giommi et al. 2013), provided suitable samples, e.g., to probe the Extragalactic Background Light (EBL, Abdo et al. 2010c; Ackermann et al. 2012c), offered suitable target lists to investigate the dichotomy between gamma-ray loud and gamma-ray quiet blazars at other wavelengths (Kovalev et al. 2009; Lister et al. 2009, 2011; Ojha et al. 2010; Giommi et al. 2012; Piner et al. 2012), and served as references for works on individual sources (e.g., Abramowski et al. 2013; Tavecchio et al. 2013).

This paper presents the third catalog of AGNs detected by the *Fermi*-LAT after four years of operation (3LAC). It is a follow-up of the 2LAC (Ackermann et al. 2011c) and makes use of the results of the 3FGL catalog (Fermi-LAT Collaboration 2015), a sequel to the 2FGL catalog (Nolan et al. 2012). The latter contained 1873 sources. In addition to dealing with more data, the 3FGL benefits from improved data selection, instrument response functions and analysis techniques. The 3FGL catalog includes 3033 sources with a Test Statistic[72] (TS) greater than 25. Among them, 2192 sources are detected at $|b| > 10°$, where b is the Galactic latitude. Among these 2192, 1563 (71%) are associated with high confidence with 1591 AGNs, which constitute the 3LAC. The 3LAC represents a sizeable improvement over the 2LAC as it includes 71% more sources[73] (1591 versus 929) with an updated data analysis.

The paper is organized as follows. In Section 2, the observations by the LAT and the analysis employed to produce the four-year catalog are described. In Section 3, we explain the methods for associating gamma-ray sources with AGN counterparts and the different schemes for classifying 3LAC AGNs. Section 4 provides a brief census of the 3LAC sample and discusses sources of particular interest. Section 5 summarizes some of the properties of the 3LAC, including the gamma-ray flux distribution, the gamma-ray spectral properties, the redshift distribution, the gamma-ray luminosity distribution, and the gamma-ray variability properties. In Section 6, we address the connection with populations of blazars detected in the two neighboring energy bands, namely the hard X-ray and VHE bands. We discuss the implications of the 3LAC results in Section 7 and present our conclusions in Section 8.

In the following, we use a ΛCDM cosmology with values from the *Planck* results (Planck Collaboration et al. 2014); in particular, we use $h = 0.67$, $\Omega_m = 0.32$, and $\Omega_\Lambda = 0.68$, where the Hubble constant $H_0 = 100\, h$ km s^{-1} Mpc^{-1}.

2. OBSERVATIONS WITH THE LARGE AREA TELESCOPE—ANALYSIS PROCEDURES

The gamma-ray results used in this paper were derived in the context of the 3FGL catalog, so we only briefly summarize the analysis here and we refer the reader to the paper describing the 3FGL catalog (Fermi-LAT Collaboration 2015) for details. No additional analysis of the gamma-ray data was performed in the context of the present paper except for the fitting of the monthly light curves described in Section 5.5. The broadband spectral energy distribution (SED) fitting described in Section 3.1.2 was also carried out in this work.

The data were collected over the first 48 months of the mission, from 2008 August 4 to 2012 July 31 (MJD 54682 to 56139). Time intervals during which the rocking angle of the LAT was greater than 52° were excluded and a cut on the zenith angle of gamma-rays of 100° was applied to limit the contribution of Earth-limb gamma-rays. Time intervals with bright gamma-ray bursts and solar flares were excised. The reprocessed Pass7REP_V15_Source event class was used, with photon energies between 100 MeV and 300 GeV. This event class shows a narrower point-spread function above 3 GeV than the Pass7_V6_Source class used in 2FGL. The source detection procedure started with an initial set of sources from the 2FGL analysis: not just those reported in that catalog, but also including all candidates failing the significance threshold. With these seeds, an all-sky likelihood analysis produced an "optimized" model, where parameters characterizing the diffuse components,[74] in addition to sources were fitted. The analysis of the residual TS map provided new seeds that were included in the model for a new all-sky likelihood analysis. This iterative procedure yielded over 4000 seeds that were then passed on to the maximum likelihood analysis for source characterization.

Events from the front and back sections of the LAT tracker (see Atwood et al. 2009, for details) were treated separately in the analysis. The analysis was performed with the binned likelihood method below 3 GeV and the unbinned method above 3 GeV. These methods are implemented in the *pyLikelihood* library of the Science Tools[75](v9r23p0). Different spectral fits were carried out with a single power-law function ($dN/dE = N_0(E/E_0)^{-\Gamma}$) and a log-parabola function ($dN/dE = N_0(E/E_0)^{-\alpha-\beta\,\log(E/E_0)}$, Massaro et al. 2004), where N_0 is a normalization factor, Γ, α and β are spectral parameters, and E_0 is an arbitrary reference energy adjusted on a source-by-source basis to minimize the correlation between N_0 and the other fitted parameters over the whole energy range (0.1–300 GeV). Whenever the difference in log(likelihood) between these two fits was greater than 8 (i.e., TS$_{\rm curve}$, which is defined as twice this difference, was greater than 16), the log-parabola results were retained. For 3C 454.3, an exponentially cutoff power law ($dN/dE = N_0(E/E_0)^{-\Gamma}\,\exp[(E_0/E_c)^b - (E/E_c)^b]$, where E_c is the cutoff energy and b the exponential index) was needed to provide a reasonable fit to the data. The photon spectral index (Γ) was obtained from the single power-law fit for all sources. A threshold of TS = 25, as calculated with the power-law model, was applied to all sources, corresponding to a significance of approximately 4σ. At the end of this procedure, 3033 sources survived the TS cut and constitute the 3FGL catalog.

Power-law fits were also performed in five different energy bands (100–300 MeV; 300 MeV–1 GeV; 1–3 GeV; 3–10 GeV; 10–300 GeV), from which the energy flux was derived. A variability index (TS$_{\rm VAR}$) was constructed from a likelihood test based on the monthly averaged light curves, with the null (alternative) hypothesis corresponding to the source being steady (variable). A source is identified as being variable at the 99% confidence level if the variability index is equal or greater than 72.44, TS$_{\rm VAR}$ being distributed as a χ^2 function with 47 degrees of freedom.

Some of the 3FGL sources were flagged as doubtful when certain issues arose during their analyses (see 3FGL for a full list of these flags). The issues that most strongly affected the 3LAC list are: (i) sources with TS > 35 going down to TS < 25 when changing the diffuse model, (ii) photon flux (>1 GeV) or energy flux (>100 MeV) changed by more than

---

[72] We use the TS = $2\Delta \log L$ for quantifying how significantly a source emerges from the background, comparing the likelihood function L with and without that source.

[73] See Ackermann et al. (2015) for a 2LAC erratum. The corrected 2LAC full and clean samples include 929 and 827 sources, respectively. A total of 63 of the 88 sources mistakenly included in the initial 2LAC full sample are now in the 3LAC catalog.

[74] The Galactic diffuse model and isotropic background model (including the gamma-ray diffuse and residual charged-particle backgrounds) are described in the 3FGL paper. Alternative Galactic diffuse models were tested as well.
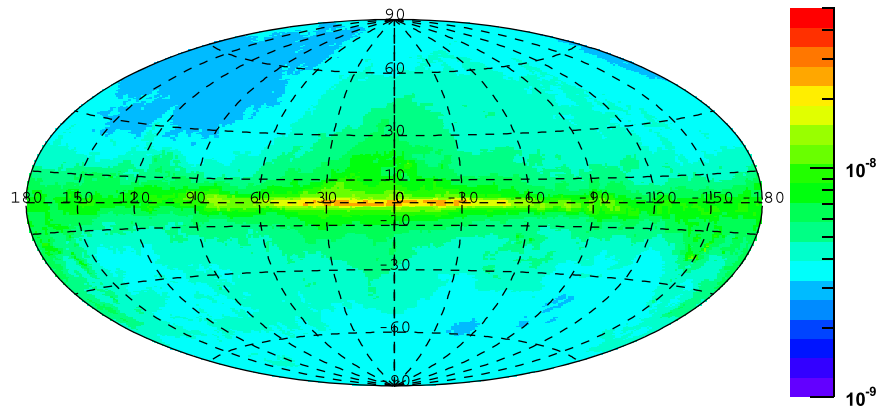
[75] http://fermi.gsfc.nasa.gov/ssc/data/analysis/documentation/Cicerone/

Figure 1. Point-source flux limit in units of ph cm^{-2} s^{-1} for $E > 100$ MeV and photon spectral index $\Gamma = 2.2$ as a function of sky location (in Galactic coordinates) for the 3LAC time interval.
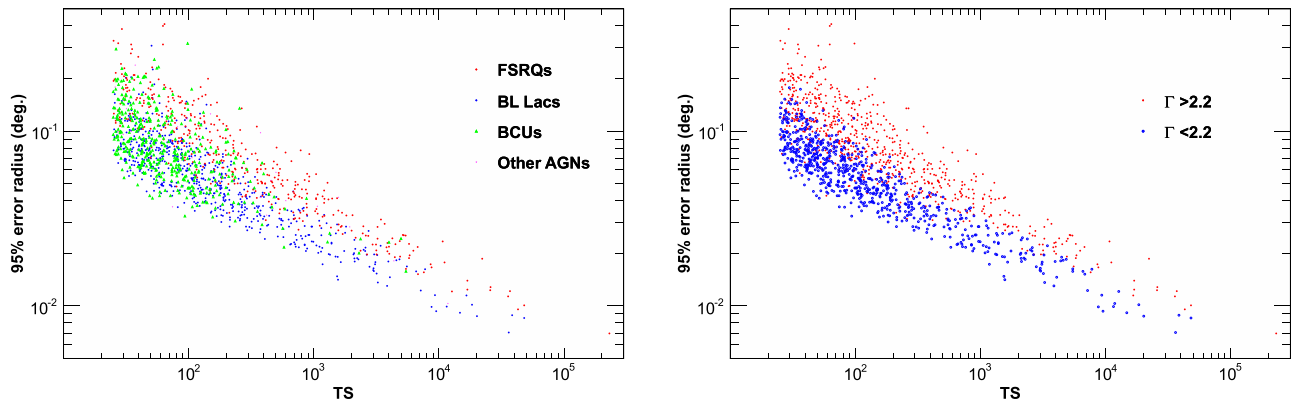

Figure 2. 95% error radius vs. TS. Left: red circles: FSRQs, blue circles: BL Lacs, green triangles: unknown type (BCUs). Right: sources with $\Gamma > 2.2$ (red) and $\Gamma < 2.2$ (blue).

3σ and 35% when changing the diffuse model, (iii) sources located close to a brighter neighbor (the conditions are defined in Table 3 of 3FGL), and (iv) source Spectral_Fit_Quality >16.3 (Spectral_Fit_Quality is the χ^2 between the fluxes in five energy bands and the spectral model). We developed a clean selection of sources by excluding sources that have any of the 3FGL analysis flags set. About 91% (1444/1591) of the 3LAC sources survived this cut. Although the Spectral_Fit_Quality condition may reject sources with unusual spectra, this condition ensures that the spectral properties discussed in the following are not affected by analysis issues.

A map of the LAT flux limit, calculated for the four-year period covered by this catalog, a TS = 25, and a photon index of 2.2, is shown in Galactic coordinates in Figure 1. A map computed for a photon index of 1.8 would look very similar, with flux limits about four times lower. The 95% error radius, θ_{95}, defined as the geometric mean of the semimajor and semi-minor axes of the source location ellipse (see 3FGL), is plotted as a function of TS in Figure 2. It ranges from about 0°.007 for 3C 454.3, the brightest LAT blazar, to 0°.08–0°.3 for sources just above the detection threshold depending on the gamma-ray spectral slope.

3. SOURCE ASSOCIATION AND CLASSIFICATION

In this work we look for candidate counterparts to 3FGL gamma-ray sources based on positional association with known cataloged objects that display AGN-type spectral characteristics. These characteristics are a flat radio spectrum between 1.4 and 5 GHz, an AGN-like broadband emission, core compactness or radio extended emission.

We recall here that in the context of AGNs, *identification* is only firmly established when correlated variability with a counterpart detected at other energies has been reported. So far, only 26 AGNs have met this condition (see 3FGL). For the rest, we use statistical approaches to find associations between LAT sources and AGNs. We will refer to the so-associated AGNs as the counterparts, although identification is not strictly established.

We apply the Bayesian Association Method (Abdo et al. 2010d) to catalogs of sources that were already classified and/or characterized. These catalogs come from specific instruments providing information on the spectrum and/or broadband emission. If a catalog reports an AGN classification, that is used. Otherwise the classification is made according to the criteria described below.

To broaden the possibility of associating a candidate AGN while knowing its broadband emission characteristics, we added the Likelihood Ratio (LR) Method (Ackermann et al. 2011c). This method can handle large uniform all-sky surveys and take the source space-density distribution into account. In the case of general radio or X-ray surveys, including AGN and non-AGN sources, the classification procedure is the same as for the Bayesian Association Method.

These two association approaches have been extensively described in previous catalog papers, so only updates will be given here (see Section 3.2).

4

3.1. Source Classification

To define the criteria that a source must fulfill to be considered an AGN, the ingredients are primarily the optical spectrum and to a lesser extent other characteristics such as radio loudness, flat/steep radio spectrum between 1.4 and 5 GHz, broadband emission, flux variability, and polarization.

We stress that we are classifying the candidate counterpart to a 3FGL source. If available, the earlier classification in the literature of each reported candidate counterpart was checked.

3.1.1. Optical Classification

To optically classify a source we made use of different resources, in decreasing order of precedence: optical spectra from our intensive follow-up program (Shaw et al. 2013), the BZCAT list (i.e., classification from this list, which is a compilation of sources ever classified as blazars, Massaro et al. 2009), and spectra available in the literature, e.g., SDSS (Ahn et al. 2012), 6dF (Jones et al. 2009), when more recent than the version 4.1.1 of BZCAT (2012 August). The latter information was used only if we found a published spectrum.

The resulting classes are as follows.

1. Confirmed classifications: flat-spectrum radio quasar (FSRQ), BL Lac, radio galaxy, steep-spectrum radio quasar (SSRQ), Seyfert, and Narrow-Line Seyfert 1 (NLSy1)—these are sources with a well-established classification in the literature and/or through a well evaluated optical spectrum (with clear evidence for or lack of emission lines).

2. Tentative classifications: BCU—blazar candidates of uncertain type: these are considered candidate blazars because the association methods (see Sections 3.2.1 and 3.2.2) select a candidate counterpart that satisfies at least one of the following conditions:

(a) a BZU object (blazar of uncertain/transitional type) in the BZCAT list;
(b) a source with multiwavelength data in one or more of the *WISE* (D'Abrusco et al. 2013), AT20G (Murphy et al. 2010), VCS (Kovalev et al. 2007), CRATES (Healey et al. 2007), PMN-CA (Wright et al. 1996), CRATES-Gaps (Healey et al. 2007), or CLASS (Myers et al. 2003) source lists, that indicates a flat radio spectrum, and shows a typical two-humped, blazar-like SED; and
(c) a source included in radio and X-ray catalogs not listed above and for which we found a typical two-humped, blazar-like SED (see Böttcher 2007).

The *BCU* sources are divided into three sub-types:
BCU I: the counterpart has a published optical spectrum but is not sensitive enough for a classification as an FSRQ or a BL Lac;
BCU II: the counterpart is lacking an optical spectrum but a reliable evaluation of the SED synchrotron-peak position is possible;
BCU III: the counterpart is lacking both an optical spectrum and an estimated synchrotron-peak position but shows blazar-like broadband emission and a flat radio spectrum;
AGN—the counterparts show SEDs typical of radio-loud compact-core objects, but data are lacking in the literature to be more specific about their classes.

3.1.2. SED Classification

To better characterize the candidate counterparts of the 3FGL sources that we consider to be candidate blazars or more generally radio-loud AGNs, we studied their broadband SEDs by collecting all data available in the literature.[76]

We use the estimated value of the (rest-frame) broadband-SED synchrotron peak frequency $\nu_{\mathrm{peak}}^{\mathrm{S}}$ to classify the source as either a low-synchrotron-peaked blazar (LSP, for sources with $\nu_{\mathrm{peak}}^{\mathrm{S}} < 10^{14}$ Hz), an intermediate-synchrotron-peaked blazar (ISP, for 10^{14} Hz $< \nu_{\mathrm{peak}}^{\mathrm{S}} < 10^{15}$ Hz), or a high-synchrotron-peaked blazar (HSP, if $\nu_{\mathrm{peak}}^{\mathrm{S}} > 10^{15}$ Hz). We refer the reader to the 2LAC paper for the list of broadband data used in this procedure.

The estimation of $\nu_{\mathrm{peak}}^{\mathrm{S}}$ relies on a 3rd-degree polynomial fit of the low-energy hump of the SED performed on a source-by-source basis, while in previous catalogs (1LAC, 2LAC) an empirical parameterization of the SED based on the broadband indices α_{ro} (radio-optical) and α_{ox} (optical-X-rays) was used (see Abdo et al. 2010a). In this new method, some sources changed SED classification with respect to the 2LAC (see below).

This new procedure allows more objects to be assigned peak parameters than the empirical method since there is no need for a measured X-ray flux if the curvature is sufficiently pronounced in the IR-optical band. Even though a scrupulous check was performed for each individual source, caution is advised in using these $\nu_{\mathrm{peak}}^{\mathrm{S}}$ values that were determined using non-simultaneous broadband data. Significant contamination from thermal/disk radiation may result in overestimation of the $\nu_{\mathrm{peak}}^{\mathrm{S}}$ values of FSRQs, while the contribution of the host galaxy may bias the peak estimate toward lower frequencies in BL Lacs. Comparing the two procedures indicates that the new procedure leads to an average shift of +0.26 (rms: 0.49) and −0.05 (rms: 0.64) in log $\nu_{\mathrm{peak}}^{\mathrm{S}}$ relative to the previous one for FSRQs and BL Lacs, respectively, which we take as typical systematic uncertainties.

In the electronic tables, we report the so-obtained observer-frame values of $\nu_{\mathrm{peak}}^{\mathrm{S}}$, as well as the rest-frame values (i.e., corrected by a $(1 + z)$ factor). For BL Lac and BCU sources without measured redshifts, a redshift $z = 0$ was assumed for the SED classification, but we omit these sources in figures showing $\nu_{\mathrm{peak}}^{\mathrm{S}}$. Assuming a redshift of 1 for these sources as suggested by Giommi et al. (2013) would lead to a shift in the rest-frame log $\nu_{\mathrm{peak}}^{\mathrm{S}}$ of +0.3, taken as an additional systematic uncertainty.

The $\nu_{\mathrm{peak}}^{\mathrm{S}}$ distributions for FSRQs and BL Lacs are displayed in Figure 3. The FSRQ distribution is sharply peaked around log $\nu_{\mathrm{peak}}^{\mathrm{S}} = 13$ while BL Lacs span the whole parameter space from low (LSP) to the highest frequencies (HSP). The BCU distribution resembles that of BL Lacs with an additional fairly weak component akin to FSRQs at this low ν_{peak} end.

3.2. Source Association

3.2.1. The Bayesian Association Method

This method (see Abdo et al. 2010d) uses Bayes' theorem to calculate the posterior probability that a catalog source is the

---

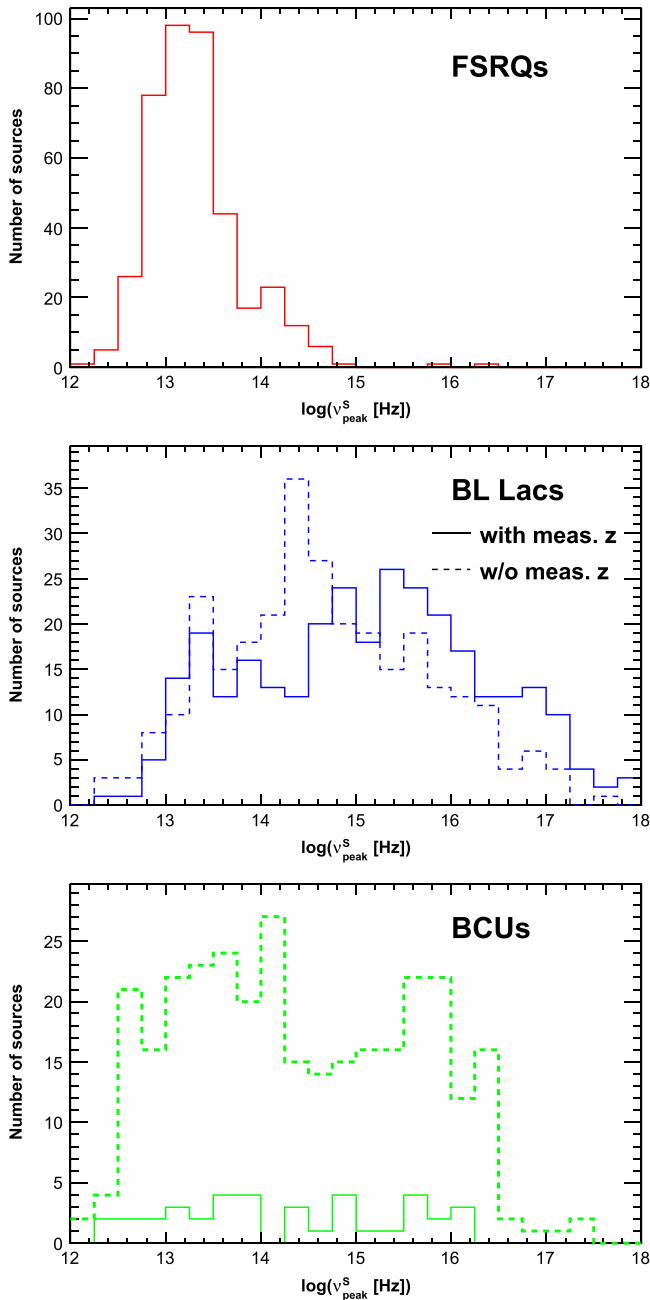[76] We made extensive use of the SED Builder online tool available at the ASI Science Data Center, http://tools.asdc.asi.it/SED/.

Figure 3. Distributions of the synchrotron peak frequency ν_{peak}^{S} for FSRQs (top), BL Lacs (middle), and BCUs (bottom) in the Clean Sample (defined in Section 3.3). The solid and dashed histograms correspond to sources with and without measured redshifts, respectively. The $(1 + z)$ correction factor (to convert to rest-frame values) has thus been applied to ν_{peak}^{S} only for the former.

true counterpart of an LAT source. The significance of a spatial coincidence between a candidate counterpart from a catalog C and an LAT-detected gamma-ray source is evaluated by examining the local density of counterparts from C in the vicinity of the LAT source. If the candidate counterpart has not been established as an AGN in a catalog C, all we have is a positional association. The nature of the candidate counterpart is subsequently studied through the literature and SED study (See Section 3.1). The catalogs used in 3LAC are the 13th edition of the Veron catalog (Véron-Cetty & Véron 2010), version 4.1.1 of BZCAT (Massaro et al. 2009), the CRATES

and CGRaBs catalogs (Healey et al. 2007), the 2010 December 5 version of the VLBA Calibrator Source List,[77] the most recent version of the TeVCat catalog,[78] and the Australia Telescope 20 GHz Survey (AT20G; Murphy et al. 2010), which contains entries for 5890 sources observed at declination $\delta < 0°$. Associations with the *Planck* Early Release Catalogs (Planck Collaboration et al. 2011) were performed as well, but an association solely with a *Planck* counterpart was not considered sufficient to call the source an AGN candidate, as *Planck* detects sources of various types. Additions relative to 2LAC are the list of *WISE* gamma-ray blazar candidates from D'Abrusco et al. (2013) and Arsioli et al. (2015). The whole list of catalogs used in this method is given in Table 12 of the 3FGL paper (Fermi-LAT Collaboration 2015).

3.2.2. The Likelihood-ratio Association Method

The LR method has frequently been used to assess identification probabilities for radio, infrared, and optical sources (e.g., de Ruiter et al. 1977; Prestage & Peacock 1983; Sutherland & Saunders 1992; Lonsdale et al. 1998; Masci et al. 2001; Ackermann et al. 2011c). It is based on uniform surveys in the radio and in X-ray bands, enabling us to search for possible counterparts among the faint radio and X-ray sources. The LR makes use of counterpart densities (assumed spatially constant over the survey region) through the $\log N$–$\log S$ relation and therefore the source flux. As for the Bayesian method applied to catalogs without classification information, we can only claim a positional association for these counterparts. The nature of the candidate counterpart is subsequently studied through the literature and SED properties (see Section 3.1).

We made use of a number of relatively uniform radio surveys. Almost all radio AGN candidates of possible interest are in the NRAO VLA Sky Survey (NVSS; Condon et al. 1998), and the Sydney University Molonglo Sky Survey (SUMSS; Mauch et al. 2003). We also added AT20G. In this way we are able to look for radio counterparts with detections at higher frequencies. To look for additional possible counterparts we cross-correlated the LAT sources with the most sensitive all-sky X-ray survey, the *ROSAT* All Sky Survey (RASS) Bright and Faint Source Catalogs (Voges et al. 1999, 2000). The method, which computes the probability that a suggested association is the "true" counterpart, is described in detail in Section 3.2 of the 2LAC paper. A source is considered a likely counterpart of the gamma-ray source if its reliability, log LR, (see Equation (4) in the 2LAC paper) is greater than 0.8 in at least one survey. The critical values of log LR_c above which the reliability is greater than 0.8 are 1.69, 0.52, 2.42, and 5.80 for the NVSS, SUMSS, RASS, and AT20G surveys, respectively.

3.3. Association Results

The adopted threshold for the association probability is 0.80 in either method. This value represents a compromise between association efficiency and purity. As in previous LAC catalog versions, we define a Clean Sample as 3LAC single-association sources free of the analysis issues mentioned in Section 2. Table 1 compares the performance of the two methods in terms

---

[77] The VLBA Calibrator Source List can be downloaded from http://www.vlba.nrao.edu/astro/calib/vlbaCalib.txt.
[78] http://tevcat.uchicago.edu

Table 1
Comparison of Association Methods in Terms of the Total Number of Associations, the Estimated Number of False Associations (N_{false}), and the Number of Sources Associated only via a Given Method, N_{S}

Sample	All Methods		Bayesian Method			LR Method		
	Total	N_{false}	Total	N_{false}	N_{S}	Total	N_{false}	N_{S}
All	1591	29.7	1529	34.5	379	1212	120.5	62
Clean Sample	1444	23.4	1391	17.5	337	1107	107.3	53

of the total number of associations, the estimated number of false associations N_{false}, calculated as $N_{\text{false}} = \sum_i (1 - P_i)$, where P_i is the association probability for the ith source, and the number of sources associated solely via a given method, N_{S}, for the full and Clean samples.

The fraction of sources associated by both methods is 71% (1150/1591), 379, and 62 sources being solely associated with the Bayesian and LR methods, respectively. Among the former, 177 sources are associated due to the list of *WISE* gamma-ray blazar candidates only (over 1000 3FGL sources have counterparts in that catalog). The overall false-positive rate is 1.9%. The estimated number of false positives among the 571 sources not previously detected in 2FGL and previous LAT catalogs is 12.0 (2.1%).

Figure 4 displays the distributions of separation distance between the gamma-ray sources and their assigned counterparts, normalized to $\sigma = \theta_{95}/\sqrt{-2\log(0.05)}$, for the whole sample and for the newly detected sources. Both agree well with the distributions expected for real associations, as expected from the overall low false-positive rate.

Figure 4. Distributions of normalized angular separation between 3LAC sources and their assigned counterparts. The normalization factor σ is defined in the text. Red: total. Blue: new sources. The curves correspond to the expected distribution for real associations and the dashed line illustrates that expected for spurious associations.

3.4. Blazar Candidates by the Australia Telescope Compact Array

In this section, we point out blazar candidates derived from the recent work of Petrov et al. (2013) but not all included in 3LAC. Using the Australia Telescope Compact Array (ATCA) at 5 GHz and 9 GHz, Petrov et al. (2013) detected 424 sources in the LAT error ellipses of southern unassociated 2FGL sources. They found that 84 of them have radio-source counterparts with a spectral index flatter (i.e., greater) than −0.5.

The 424 sources are characterized by weak radio fluxes (<100 mJy), and were thus missing from the previous AT20G. Flat spectrum radio sources cannot be directly associated with extragalactic sources like blazars, as peculiar Galactic objects (like, for example, η Carinae, microquasars, compact H II regions, planetary nebulae) can also exhibit a flat radio spectrum. On the other hand a steep radio spectrum does not rule out an extragalactic nature. A total of 24 sources among the 84 flat-spectrum ones are included in 3LAC, as they now fulfill the required criterion (association probability greater than 0.8). An additional 21 sources listed in Table 2 show double-humped radio-to-gamma-ray SEDs resembling those of BCU, but they have association probabilities below threshold. More data may help secure these associations in the future.

4. THE THIRD LAT AGN CATALOG (3LAC)

4.1. Census

Table 3 summarizes the 3LAC source statistics. The 3LAC includes 1591 objects, with 467 FSRQs, 632 BL Lacs, 460
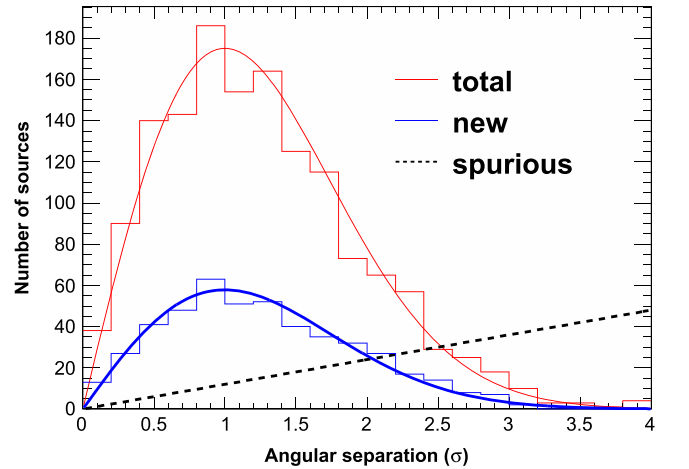
BCUs, and 32 non-blazar AGNs. Their properties are given in Table 4.

A total of 1563 gamma-ray sources have been associated with radio-loud AGNs among 2192 $|b| > 10°$ 3FGL sources, corresponding to an overall association fraction of 72%. The fraction changes substantially between the northern and southern celestial hemispheres (843/1136 = 74% and 731/1056 = 69% respectively), an effect essentially entirely driven by unassociated southern-hemisphere BL Lacs as discussed below.

Only sources in the Clean Sample will be used in the following tallies and figures unless stated otherwise. It includes 1444 objects with 414 FSRQs, 604 BL Lacs, 402 BCUs, and 24 non-blazar AGNs.

A comparison of the results inferred from the 3LAC and 2LAC enables the following observations:

1. The 3LAC Clean Sample includes 619 more sources than the 2LAC Clean Sample, i.e., a 75% increase. Of these, 477 sources are new (81 FSRQs, 146 BL Lacs, 240 blazars of unknown type, 10 non-blazar objects); the other sources were present in previous *Fermi* catalogs but not included in Clean Samples for various reasons (e.g., the corresponding gamma-ray sources were not associated with AGNs, had more than one counterpart or were flagged in the analysis). The fraction of new sources (not present in 1FGL or 2FGL) is slightly higher for hard-spectrum (i.e., $\Gamma < 2.2$) sources than for soft-spectrum ones (i.e., $\Gamma > 2.2$), 51% versus 47%, respectively, but the relative increase reaches 72% for very hard-spectrum (i.e., $\Gamma < 1.8$) sources.

Table 2
List of ATCA Blazar Candidates

3FGL Name	Counterpart name	R.A. radio (°)	Decl. radio (°)	Class count	Log(ν_{peak}^{S}[Hz])	2FGL Name
J0102.1+0943	NVSS J010217+094407	15.57133	9.73622	BCU II	14.419	J0102.2+0943
J0437.7−7330	SUMSS J043836−732921	69.65392	−73.48994	BCU III	⋯	J0438.0−7331
J0725.7−0550	NVSS J072547−054832	111.44867	−5.80753	BCU III	⋯	J0725.8−0549
J0737.8−8245	SUMSS J073706−824836	114.47621	−82.73703	BCU III	⋯	J0737.5−8246
J0937.9−1435	NVSS J093754−143350	144.47783	−14.56414	BCU II	17.150	J0937.9−1434
J1016.6−4244	1RXS J101620.6−424733	154.08650	−42.78975	BCU II	15.600	J1016.4−4244
J1038.0−2425	NVSS J103824−242355	159.59987	−24.39869	BCU II	12.550	J1038.2−2423
J1117.2−5338	MGPS J111715−533816	169.31279	−53.63783	BCU II	14.755	J1117.2−5341
J1115.0−0701	NVSS J111511−070238	168.79832	−7.04417	BCU III	⋯	J1115.0−0701
J1207.2−5052	SUMSS J120719−505350	181.79211	−50.86061	BCU III	⋯	J1207.3−5055
J1240.3−7149	MGPS J124021−714901	190.08821	−71.81653	BCU III	⋯	J1240.6−7151
J1249.1−2808	NVSS J124919−280833	192.33118	−28.14239	BCU II	15.080	J1249.5−2811
J1424.3−1753	NVSS J142412−175010	216.05145	−17.83611	BCU II	15.750	J1424.2−1752
J1539.2−3324	NVSS J153911−332209	234.79825	−33.36822	BCU III	⋯	J1539.2−3325
J1704.4−0528	NVSS J170433−052839	256.14075	−5.47753	BCU II	15.200	J1704.6−0529
J1747.3+0324	NVSS J174733+032703	266.88860	3.45119	BCU III	⋯	J1747.6+0324
J1757.7−6030	SUMSS J175734−603032	269.39413	−60.50794	BCU III	⋯	J1757.5−6028
J2034.6−4202	SUMSS J203451−420024	308.71274	−42.01044	BCU II	15.640	J2034.7−4201
J2046.7−4259	SUMSS J204643−425711	311.68353	−42.95358	BCU III	⋯	J2046.2−4259
J2134.5−2131	NVSS J213430−213032	323.62580	−21.50858	BCU II	15.410	J2134.6−2130
J2258.2−3645	NVSS J225815−364433	344.56195	−36.74264	BCU II	15.150	J2257.9−3646

2. The fraction of BCU has increased notably between the two catalogs (from 20% to 28%). The number of these sources in the 3LAC Clean Sample has increased by more than a factor of 2.5 relative to that in the 2LAC Clean Sample, being almost equal to the number of FSRQs. This increase is mainly due to the lower probability of having a published high-quality spectrum available for these fainter sources because of the lack of optical/near-infrared observing programs. The census of the BCU sources in the Clean Sample is: 49 BCU I, 308 BCU II, 45 BCU III.

3. The relative increase in BCUs drives a drop in the proportions of FSRQs and BL Lacs, which only represent 29% and 41% of the 3LAC Clean Sample, respectively (38% and 48% for 2LAC). The relative increase in the number of sources with respect to 2LAC is 34% and 42% for FSRQs and BL Lacs respectively.

4. Out of 827 sources in the 2LAC Clean Sample, a total of 69 are missing in the 3LAC Clean Sample (42 in the full sample), some of them probably due to variability effects. A few others are present in 3FGL but with shifted positions, ruling out their association with their former counterparts.

The loci of sources in the Clean Sample are shown in Figure 5, both in Galactic and celestial coordinates. The deficit in classified AGNs in the region of the celestial south pole already reported in 2LAC is clearly visible, while a relative excess is seen in the region of the celestial north pole. This anisotropy is mainly driven by BL Lacs, with 51% more sources in the northern Galactic hemisphere (362) than in the southern one (242). This effect is ascribed to the relative incompleteness of the counterpart catalogs in the southern hemisphere (for instance, NVSS only covers the $\delta > -40°$ sky, where δ is the declination). It is very partially offset by an observed relative excess (54 sources) of associations with BCU in the south relative to the north.

4.2. Non-blazar Objects and Misaligned AGNs

Blazars represent the overwhelming majority of 3LAC AGNs, with non-blazar AGNs only constituting 2% of the sample. In 2LAC, eleven sources were classified as AGNs, i.e., were neither confirmed blazars nor blazar candidates (such as BCUs). Although there may have been evidence for their flatness in radio emission or broadband emission, our intensive optical follow-up program did not provide clear evidence for optical blazar characteristics. Nine of them remain in 3LAC, and are now all classified as BCUs, except for one now classified as a BL Lac.

Misaligned AGNs (MAGNs), with jets pointing away from the observer, are not favored GeV sources. By MAGNs we mean radio-loud AGNs with jets directed at large angles relative to the line-of-sight that display steep radio spectra ($\alpha_r \geqslant 0.5$, with the usual convention that $F_\nu \propto \nu^{-\alpha}$) and bipolar or quasi-symmetrical structures in radio maps. The larger jet inclination angle relative to blazars means the observed radio emission from the relativistic jet is not significantly Doppler boosted, making it less prevalent over other radio components such as synchrotron radiation from mildly relativistic outflows or extended radio lobe emission (Abdo et al. 2010e).

Table 5 summarizes the non-blazar objects and MAGNs in the 3FGL/3LAC, also noting their previous appearances in the 2FGL/2LAC and 1FGL/1LAC. All the 1FGL sources, detected in 11 months of exposure, were subsequently studied with 15 months of data (Abdo et al. 2010e).

M 87 was one of the first new *Fermi*-LAT detections (Abdo et al. 2009d) of a source classified as a non-blazar object, being a low-power Fanaroff & Riley (1974) type-I (FRI) radio galaxy. Many of the newly associated non-blazar objects are nearby FRIs—J0758.7+3747 (3C 189, a.k.a., B2 0755+37) and 3C 264. The gamma-ray detection of the latter case was recently reported in a study of its parent cluster Abell 1367 (Ackermann et al. 2011a), although the gamma-rays likely originate from the AGN. We remark that 0′.8 away from 3C

Table 3
Census of Sources

AGN Type	Entire 3LAC	3LAC Clean Sample[a]	Low-latitude Sample
All[b]	**1591**	**1444**	**182**
FSRQ	**467**	**414**	**24**
…LSP	412	366	24
…ISP	47	42	0
…HSP	3	2	0
…no SED classification	5	4	0
BL Lac	**632**	**604**	**30**
…LSP	162	150	8
…ISP	178	173	6
…HSP	272	265	12
…no SED classification	20	16	4
Blazar of Unknown type	**460**	**402**	**125**
…BCU I	57	49	11
…LSP BCU I	26	24	8
…ISP BCU I	11	9	1
…HSP BCU I	13	13	2
…BCU I w/o SED classification	7	3	0
…BCU II	346	308	85
…LSP BCU II	156	129	39
…ISP BCU II	78	70	13
…HSP BCU II	107	105	31
…BCU II w/o SED classification	5	4	2
…BCU III	57	45	29
…LSP BCU III	16	11	9
…ISP BCU III	0	0	0
…HSP BCU III	0	0	0
…BCU III w/o SED classification	41	34	20
Non-blazar AGN	**32**	**24**	**3**
…CSS	2	1	0
…NLSy1	5	5	0
…RG	14	13	2
…SSRQ	5	3	0
…Other AGN	6	2	1

Notes.
[a] Sources with single counterparts and without analysis flags. See Section 3.1 for the definitions of this sample.
[b] Bold values are the total numbers for each subclass.

189 lies the quasar SDSS J075825.87+374628.7 with redshift 1.50. With the resolution of the NVSS, this source cannot be disentangled from the radio emission of 3C 189. This may be the reason why this source is not present in the NVSS catalog, precluding the estimation of the association probability with the gamma-ray source.

NGC 1275 (3C 84, Perseus A) was first detected in the initial LAT bright source list based on 3 months of data (Abdo et al. 2009e). It was probably detected previously with COS-B (Strong & Bignami 1983), but not with EGRET. In the *Fermi* era, it is a strong source, exhibiting GeV variability (Abdo et al. 2009c; Kataoka et al. 2010). 3C 120 is not listed in any of the FGL catalogs but its detection was reported in a 15 month

study (Abdo et al. 2010e). There are indications that 3C 120 undergoes a series of flares with a low long-term average flux. For instance, in 2014 September a flaring source positionally consistent with 3C 120 was detected with a high significance (TS > 50; Tanaka et al. 2014). The closest 3FGL source, 3FGL J0432.5+0539, lies 0°.35 away, with an 95% error radius of 0°.15, hampering association with 3C 120 by our methods. This gamma-ray source has a soft spectrum ($\Gamma = 2.7 \pm 0.1$), comparable with that ascribed to 3C 120 (Abdo et al. 2010e; Kataoka et al. 2011). The possibility of two separate, soft-spectrum sources cannot be excluded. Another known example from previous lists is 3C 78 (NGC 1218; Abdo et al. 2010g).

Cen A was also reported in the initial LAT bright source list (Abdo et al. 2009e), confirming the EGRET source (Hartman et al. 1999; Sreekumar et al. 1999). It remains as the only AGN with a significant detection of extended gamma-ray emission (Abdo et al. 2010b). There is no convincing case of extended emission in other radio galaxies with relatively large radio extensions, such as Cen B (Katsuta et al. 2013), NGC 6251 (Takeuchi et al. 2012), and Fornax A. Fornax A may be a good case to investigate this emission (Cheung et al. 2007; Georganopoulos et al. 2008). The closest 3FGL source is offset from the Fornax A core by 0°.15, while the 95%-contour distance is 0°.092 (see Figure 6 for a VLA 1.5 GHz image). NGC 6251 (one square degree in solid angle) was also detected by EGRET (Mukherjee et al. 2002). Its location shifted between 1LAC and 2LAC toward the western radio lobe.

3C 111 was also a previous EGRET source (Hartman et al. 2008) and also shows apparent variability (e.g., Abdo et al. 2010e; Kataoka et al. 2011; Grandi et al. 2012). It joins the other two FR type-II sources listed in Table 5: 3FGL J1442.6+5156 (3C 303) and 3FGL J0519.2−4542 (Pictor A). The latter are also broad-lined radio galaxies (BLRGs), and are new detections. The LAT detection of Pictor A was reported by Brown & Adams (2012) following[79] a previous tentative detection (Kataoka et al. 2011).

The previous LAT detections of PKS 0625−35 and IC 310, two radio galaxies with BL Lac characteristics, were reported in 2LAC, and are confirmed. IC 310 has been classified as a head-tail galaxy (Neronov et al. 2010), but recent works have found increasing evidence for blazar-like properties, e.g., blazar-like VLBI jet structure (Kadler et al. 2012a) and extremely fast TeV variability (Aleksić et al. 2014). The source 4C +39.12 (3FGL J0334.2+3915) was classified as a low-power compact source by Giovannini et al. (2001), separate from its Fanaroff–Riley classification. Two new compact steep-spectrum (CSS) sources are detected: 3FGL J1330.5+3023 (3C 286) and 3FGL J0824.9+3916 (4C +39.23B). While both are CSS, the latter is a duplicate association (the other association being the FSRQ blazar 4C+39.23) so it is not in the Clean Sample. The former has the morphology of a medium symmetric object (MSO), like that of the LAT-detected FSRQ 4C +55.17 (McConville et al. 2011).

The gamma-ray detections of 3C 207 and 3C 380 were first reported in 1LAC. They appear in the 3CRR catalog (Laing et al. 1983) by virtue of their bright low-frequency emission due to the presence of kpc-scale extended steep-spectrum radio lobes, and thus are formally classified as SSRQs. However, they contain pronounced flat-spectrum radio cores with

---

[79] The results of Brown & Adams (2012) are in tension with those presented here, with their reported statistical uncertainties being very small given the low source flux.

Table 4
High Latitude ($|b| > 10°$) 3LAC Full Sample

3FGL Source Name (1)	Counterpart Name (2)	R.A. (°) (3)	Decl. (°) (4)	AngSep (°) (5)	θ_{95} (°) (6)	Optical Class (7)	SED Class (8)	$\log(\nu_{peak}^{S,meas})$ (9)	$\log(\nu_{peak}^{S})$ (10)	z (11)	Prob. Bay. (12)	Rel. LR_{RG} (13)	Rel. LR_{XG} (14)	Compton Dominance (15)
J0001.2−0748[a]	PMN J0001−0746	0.32510	−7.77411	0.042	0.075	BLL	ISP	14.486	14.486	⋯	0.9978	0.859	0.00	⋯
J0001.4+2120[a]	TXS 2358+209	0.38502	21.22679	0.113	0.199	FSRQ	ISP	14.163	14.486	1.10600	0.924	0.00	0.000	2.40
J0002.2−4152[a]	1RXS J000135.5−415519	0.38642	−41.92367	0.137	0.174	BCU II	HSP	15.800	15.800	⋯	0.972	0.000	0.000	−0.59
J0003.2−5246[a]	RBS 0006	0.83121	−52.79103	0.017	0.065	BCU II	HSP	16.850	16.850	⋯	0.998	0.000	0.900	−0.52
J0003.8−1151	PMN J0004−1148	1.02048	−11.81622	0.076	0.114	BCU II	LSP	12.515	12.515	⋯	0.995	0.869	0.000	⋯
J0003.8−1151	PKS 0001−121	0.92848	−11.86372	0.030	0.114	BCU I	⋯	⋯	⋯	1.30999	0.988	0.871	0.000	⋯

Note. Columns 1 and 2 are the 3FGL and counterpart names, columns 3 and 4 are the counterpart J2000 coordinates, column 5 gives the angular separation between the gamma-ray and counterpart positions, column 6 is the 95% error radius on the gamma-ray position, column 7 lists the optical class, column 8 is the spectral energy distribution (SED) class (depending on the synchrotron peak frequency given in column 9), column 10 is the synchrotron peak frequency corrected for the redshift shown in column 11, and columns 12–14 report the probability for the Bayesian method and the two reliability values, LR_{RG} and LR_{XG}, for the radio–gamma-ray match and the X-ray–gamma-ray match respectively. Column 15 reports $\log(CD)$.
[a] Refers to sources in the Clean Sample.

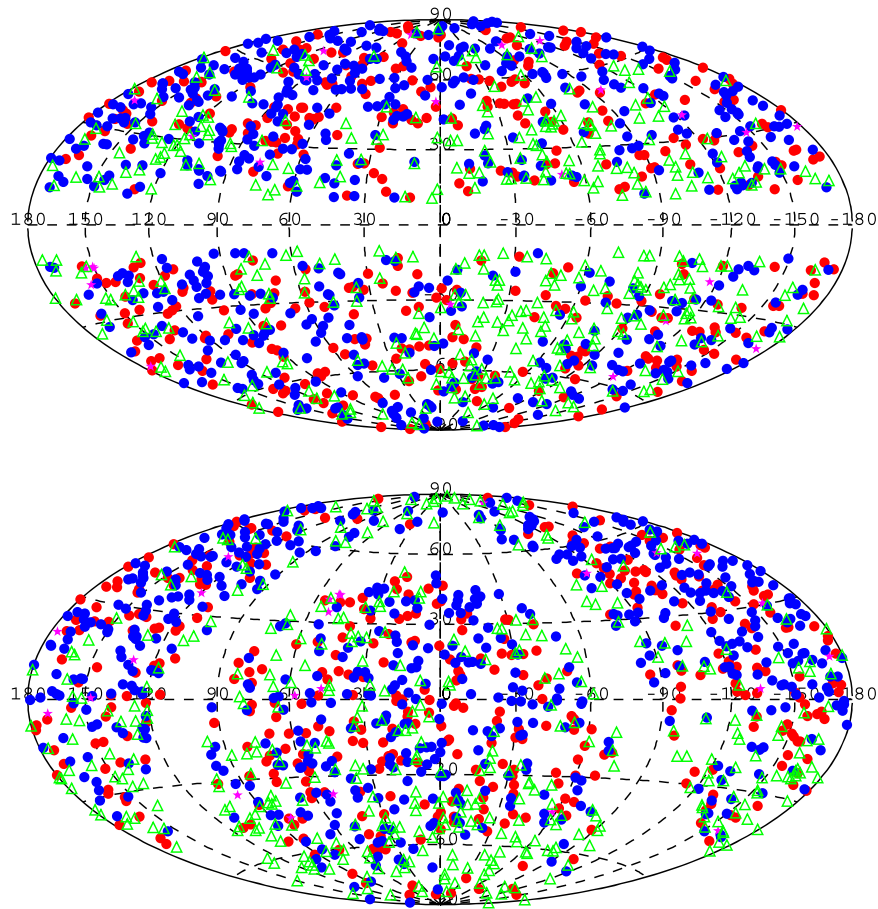(This table is available in its entirety in machine-readable form.)

Figure 5. Locations of the sources in the Clean Sample in Galactic (top) and J2000 equatorial (bottom) coordinates. Red circles: FSRQs; blue circles: BL Lacs; green triangles: blazars of unknown type; magenta stars: other AGNs.

superluminal motions measured in their parsec-scale jets, indicating that they are the most well-aligned sources to our line of sight among the SSRQs in the 3CRR (e.g., Wilkinson et al. 1991; Hough 2013; Lister et al. 2013). New ones to highlight are 3C 275.1 (3FGL J1244.1+1615), TXS 0348+013 (3FGL J0351.1+0128), and 4C +39.26 (3FGL J0934.1+3933). The SSRQ 4C+04.40 is part of a double association (with the FSRQ MG1 J120448+0408) of 3FGL J1205.4+0412.

GB 1310+487 is a gamma-ray/radio-loud narrow-line AGN at $z = 0.638$, showing a gamma-ray flare in November 2009 and located behind the disk of an unrelated emission-line galaxy at $z = 0.500$ (Sokolovsky et al. 2014).

Circinus, a type-2 Seyfert galaxy located at $b = -3°.8$ and thus not in 3LAC, was recently detected (Hayashida et al. 2013). Other Seyfert detections were investigated (Teng et al. 2011; Ackermann et al. 2012b; Lenain et al. 2010), but were found to be starburst galaxies (Ackermann et al. 2012a).

The detections of NGC 6951 (classified as a Seyfert 2 galaxy and a LINER, reported in 1LAC but missing in 2LAC), 3C 407 (a source with broad emission lines but with a fairly steep radio spectrum and reported in 2LAC), and NGC 6814 (type 1.5 Seyfert galaxy, also reported in 2LAC) are not confirmed. The same conclusion applies to PKS 0943−76 (studied in Abdo et al. 2010e). The previous claim that it has a FRII morphology was based on a low-resolution radio map from Burgess & Hunstead (2006). The offset between the 4 year source and PKS 0943−76 is 0°.22, while the radius of the source location region at the 95% confidence level is 0°.12. ESO 323−G77

(type 2 Seyfert galaxy), and PKS0943−76 (radio galaxy), both reported in 2LAC, were actually both mis-associated because of an error in the LR association method (Ackermann et al. 2015).

Five sources are associated with NLSy1. Four of them were included in 2LAC: 3FGL J0325.2+3410 (BZU J0324+3410), 3FGL J0948.8+0021 (PMN J0948+0022), 3FGL J1505.1 +0326 (BZQ J1505+0326), and 3FGL J2007.8−4429 (BZQ J2007−4434), while 3FGL 0849.9+5108 (SBS 0846+513) was first reported by Donato & Perkins (2011) and further studied by D'Ammando et al. (2012, 2013).

4.3. Noteworthy Sources

The highest redshift reported in 2LAC for an HSP-BL Lac was 0.7. The 3LAC lists seven (six in the Clean Sample) HSP-BL Lacs with redshifts greater than 1, six (five in the Clean Sample) of which were included in 2LAC but with other classifications or redshifts. They are briefly discussed below.

3FGL J0008.0+4713 is associated with MG4 J000800+4712. The redshift reported in 2LAC was 0.28 and its SED classification was LSP. Shaw et al. (2013) derived a redshift of 2.1 from the clear onset of the Lyα forest and their new procedure for estimating SED class together with *WISE* data classified this source as an HSP.

3FGL J0630.9−2406 is associated with TXS 0628−240, an HSP-BL Lac for which $z \gtrsim 1.238$ was determined from certain absorption features by Landt (2012).

Table 5
Non-blazar Objects and Misaligned AGNs

Name	3FGL	2FGL	1FGL	Type	Photon Index	Notes
NGC 1218	J0308.6+0408[a]	⋯	J0308.3+0403[a]	FRI	2.07 ± 0.11	⋯
IC 310	J0316.6+4119[a]	J0316.6+4119	⋯	FRI/BLL	1.90 ± 0.14	Neronov et al. (2010)
NGC 1275	J0319.8+4130[a]	J0319.8+4130[a]	J0319.7+4130[a]	FRI	2.07 ± 0.01	Abdo et al. (2009c); Kataoka et al. (2010)
1 H 0323+342	J0325.2+3410[a]	J0324.8+3408[a]	J0325.0+3403[a]	NLSy1	2.44 ± 0.12	⋯
4C+39.12	J0334.2+3915[a]	⋯	⋯	FRI/BLL?	2.11 ± 0.17	Giovannini et al. (2001)
TXS 0348+013	J0351.1+0128[a]	⋯	⋯	SSRQ	2.43 ± 0.18	⋯
3C 111	J0418.5+3813[a]	⋯	J0419.0+3811	FRII	2.79 ± 0.08	Abdo et al. (2010e); Kataoka et al. (2011); Grandi et al. (2012)
Pictor A	J0519.2−4542[a]	⋯	⋯	FRII	2.49 ± 0.18	Brown & Adams (2012); Kataoka et al. (2011)
PKS 0625−35	J0627.0−3529[a]	J0627.1−3528[a]	J0627.3−3530[a]	FRI/BLL	1.87 ± 0.06	⋯
4C+52.17	J0733.5+5153	⋯	⋯	AGN	1.74 ± 0.16	Part of a duplicate association. Most probable counterpart is a BCU III.
NGC 2484	J0758.7+3747[a]	⋯	⋯	FRI	2.16 ± 0.16	quasar SDSS J075825.87+374628.7 is 0.′8 away
4C+39.23B	J0824.9+3916	⋯	⋯	CSS	2.44 ± 0.10	⋯
3C 207	J0840.8+1315[a]	J0840.7+1310	J0840.8+1310	SSRQ	2.47 ± 0.09	⋯
SBS 0846+513	J0849.9+5108[a]	⋯	⋯	NLSy1	2.28 ± 0.04	⋯
3C 221	J0934.1+3933	⋯	⋯	SSRQ	2.28 ± 0.12	⋯
PMN J0948+0022	J0948.8+0021[a]	J0948.8+0020[a]	J0949.0+0021[a]	NLSy1	2.32 ± 0.05	⋯
PMN J1118−0413	J1118.2−0411[a]	⋯	⋯	AGN	2.56 ± 0.08	⋯
B2 1126+37	J1129.0+3705	⋯	⋯	AGN	2.08 ± 0.13	Part of a duplicate association. Most probable counterpart is a BLL.
3C 264	J1145.1+1935[a]	⋯	⋯	FRI	1.98 ± 0.20	⋯
PKS 1203+04	J1205.4+0412	⋯	⋯	SSRQ	2.64 ± 0.16	Part of a duplicate association. The other counterpart is an FSRQ.
M 87	J1230.9+1224[a]	J1230.8+1224[a]	J1230.8+1223[a]	FRI	2.04 ± 0.07	Abdo et al. (2009d)
3C 275.1	J1244.1+1615	⋯	⋯	SSRQ	2.43 ± 0.17	⋯
GB 1310+487	J1312.7+4828[a]	J1312.8+4828[a]	J1312.4+4827[a]	AGN	2.04 ± 0.03	⋯
Cen A Core	J1325.4−4301[a]	J1325.6−4300	J1325.6−4300	FRI	2.70 ± 0.03	radio core
Cen A Lobes	J1324.0−4330e	J1324.0−4330e	J1322.0−4515	FRI	2.53 ± 0.05	giant lobes detected (Abdo et al. 2010b)
3C 286	J1330.5+3023[a]	⋯	⋯	SSRQ/CSS	2.60 ± 0.16	⋯
Cen B	J1346.6−6027	J1346.6−6027	⋯	FRI	2.32 ± 0.01	Katsuta et al. (2013)
Circinus	J1413.2−6518	⋯	⋯	Seyfert	2.43 ± 0.10	Hayashida et al. (2013)
3C 303	J1442.6+5156[a]	⋯	⋯	FRII	1.92 ± 0.18	⋯
PKS 1502+036	J1505.1+0326[a]	J1505.1+0324[a]	J1505.0+0328[a]	NLSy1	2.61 ± 0.05	⋯
TXS 1613−251	J1617.3−2519	J1617.6−2526c	⋯	AGN	2.59 ± 0.10	Part of a duplicate association. Most probable counterpart is a BCU II.
PKS 1617−235	J1621.1−2331[a]	J1620.5−2320c	⋯	AGN	2.50 ± 0.23	⋯
NGC 6251	J1630.6+8232[a]	J1629.4+8236	J1635.4+8228[a]	FRI	2.22 ± 0.08	⋯
3C 380	J1829.6+4844[a]	J1829.7+4846[a]	J1829.8+4845[a]	SSRQ/CSS	2.37 ± 0.04	⋯
PKS 2004−447	J2007.8−4429[a]	J2007.9−4430[a]	J2007.9−4430[a]	NLSy1	2.47 ± 0.09	⋯

Notes. SSRQ implies FRII. The table includes the 34 non-blazar objects and MAGNs at all latitudes associated with 3FGL sources (Cen A Core and Cen A Lobes constitute a single object).
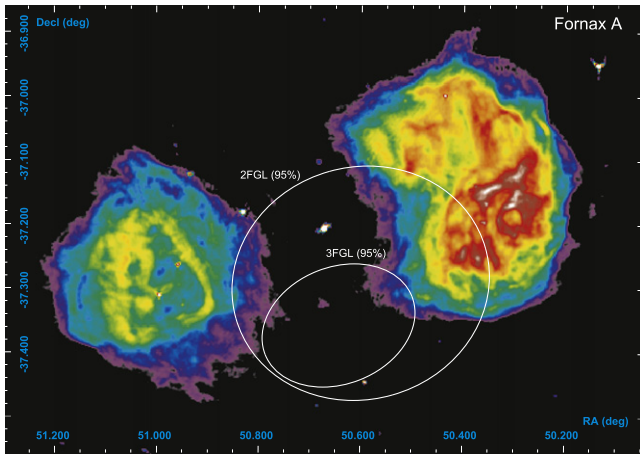[a] Refers to sources included in the Clean Sample of a given catalog.

Figure 6. VLA image of Fornax A at 1.5 GHz (Fomalont et al. 1989). The 95% error ellipses of the closest 3FGL and 2FGL sources are overlaid.

3FGL J1109.4+2411 is associated with 1ES 1106+244 and new spectroscopy from SDSS changed the redshift to 1.220.

3FGL J1312.5−2155 is associated with PKS 1309−216. In Shaw et al. (2013) a plausible Mg II feature is found; this single-line identification is in a small allowed redshift range ($z \simeq 1.6$). However, previous data (Massaro et al. 2009) show a questionable redshift of 1.491.

3FGL J2116.1+3339 is associated with B2 2114+33. The redshift quoted in 2LAC was 0.35, but a recent measurement by Shaw et al. (2013) gives $z = 1.596$, identifying a significant broad emission feature with C IV, consistent with a weak bump in the far blue at Lyα. A lower redshift is possible if the purported Lyα line is not real.

The newly detected source is *3FGL J0814.5+2943*, associated with FBQS J081421.2+294021 at $z = 1.084$ (from SDSS DR3, Ahn et al. 2012).

The highest redshift BL Lac object is *3FGL J1450.9+5200*, associated with BZB J1450+5201 with redshift $z = 2.41$ coming from new observations in Shaw et al. (2013). The presence of the Lyα forest can suppress a part of the optical spectrum, resulting in ISP classification, so the intrinsic synchrotron peak position is probably greater than our estimate.

A low-redshift source, reported as a BCU in BZCAT, has recently been classified as an FSRQ by G. Chiaro & D. Bastieri (2014, private communication): SBS 1646+499 (3FGL J1647.4+4950) with $z = 0.0467$.

Two HSP-FSRQs have been detected: BZB J0202+0849 (3FGL J0202.3+0851) and NVSS J025037+171209 (3FGL J0250.6+1713) with LAT spectral photon indices of 2.05 ± 0.16 and 1.98 ± 0.19, respectively. 3FGL J0202.3+0851 was classified as a BL Lac in 1LAC but new observations from Shaw et al. (2013) led to a reclassification as an FSRQ. These objects are probably transitional objects that show broad lines in the optical band when the continuum is low (see, e.g., Ruan et al. 2014).

4.4. Low Galactic Latitude AGNs

Because of the intrinsic incompleteness of the counterpart catalogs in this sky area ($|b| < 10°$), these sources are treated separately and are not included in the 3LAC or in the analyses presented in the rest of the paper. We report associations for 182 blazars (75% more than in 2LAC) located at $|b| < 10°$: 24

FSRQs, 30 BL Lacs, 125 BCUs, and 3 non-blazar AGNs. They are listed in Table 6. Extrapolating from the number of high-latitude sources and assuming the same sensitivity, about 340 sources would be expected in this area. The discrepancy between expected and actual source numbers stems from the dual effect of a higher detection threshold due to a higher Galactic diffuse emission background (see Figure 1) and a higher incompleteness of the counterpart catalogs for this area.

4.5. Comparison with 1LAC and 2LAC

The revised 2LAC sample (Ackermann et al. 2015) includes 929 sources, 65 of which are missing in 3LAC (Table 7). Most do not make the TS cut over the 4 year-long period, probably mainly due to variability. On the other hand, 56 unassociated sources in the 2FGL are now associated with blazars, thanks to a more complete set of counterpart catalogs and more precise localizations for the gamma-ray sources (arising from greater statistics and an improved instrument point-spread function). A total of 27 1FGL sources (not necessarily all in 1LAC) that were not listed in 2LAC are now included in 3LAC. Some 51 2LAC sources have changed classifications in 3LAC, mostly due to improved data: 8 AGNs into BCUs, 1 AGN into a BL Lac, 39 BCUs into 34 BL Lacs and 5 FSRQs, one FSRQ into a BL Lac (TXS 0404+075) and two BL Lacs into FSRQs (B2 1040+24A and 4C +15.54).

4.6. Flaring Sources Detected in the Flare Advocate Service

The 3LAC catalog lists sources detected with high significance during 48 months of observation. Some blazars flare during a limited time only and may be missing in 3LAC. If bright enough, some of them are caught in near-real time by the *Fermi* Flare Advocate service, also known as Gamma-ray Sky Watcher (FA-GSW), which we briefly describe here.

A day-by-day review of the whole gamma-ray sky, both by a human-in-the-loop and by automated science processing analysis (see, e.g., Chiang et al. 2012), results in the calculation of preliminary source fluxes, tentative localizations, and counterpart associations for any significant source detection. This service serves as an important resource for the scientific community by providing alerts on flaring or transient sources and by producing seeds for follow-up variability and multi-wavelength[80] studies (see, e.g., Ciprini & Thompson 2013).

Since the beginning of the mission, daily reports are compiled internally to the Collaboration, while information and news are communicated via the LAT-MW mailing-list,[81] published in The Astronomer's Telegrams (ATels,)[82] special GCN notices,[83] and weekly summaries in the *Fermi* Sky Blog.[84] A total of 201 ATels were posted on behalf of the LAT Collaboration in the 48 month period considered in the 3FGL/3LAC, specifically from 2008 July 24 (the first ATel#1628) to 2012 July 29 (ATel#4285), primarily derived from the FA-GSW service. Some 143 ATels contained alerts and preliminary results about blazars and other AGN targets[85] referring to 71 different FSRQs, 18 different BL Lac objects,

---

[80] For example the LAT MW Coordinating Group page: confluence.slac.stanford.edu/x/YQw
[81] Address: lists.nasa.gov/mailman/listinfo/gammamw/
[82] www-glast.stanford.edu/cgi-bin/pub_rapid
[83] gcn.gsfc.nasa.gov/gcn/fermi_lat_mon_trans.html
[84] The *Fermi* Gamma-ray Sky Blog: fermisky.blogspot.com
[85] An interactive incremental list is available at: www.asdc.asi.it/feratel/.

14

Table 6
Low-latitude ($|b| < 10°$) Sample

3FGL Source Name	Counterpart Name	R.A. (°)	Decl. (°)	AngSep (°)	θ_{95} (°)	Optical Class	SED Class	$\log(\nu_{\rm peak}^{\rm S,meas})$	$\log(\nu_{\rm peak}^{\rm S})$	z	Prob. Bay.	Rel. $LR_{\rm RG}$	Rel. $LR_{\rm XG}$
(1)	(2)	(3)	(4)	(5)	(6)	(7)	(8)	(9)	(10)	(11)	(12)	(13)	(14)
J0012.4+7040	TXS 0008+704	2.88293	70.75878	0.115	0.105	BCU II	LSP	13.075	13.075	...	0.912	0.856	...
J0014.6+6119	4C +60.01	3.70330	61.29543	0.031	0.061	BCU II	LSP	13.113	13.113	...	0.997	0.976	...
J0014.7+5802	1RXS J001442.2+580201	3.67471	58.03404	0.009	0.055	BLL	HSP	16.640	16.640	...	...	...	0.936
J0015.7+5552	GB6 J0015+5551	3.91737	55.86226	0.018	0.043	BCU II	HSP	15.791	15.791	...	0.998	0.868	0.952
J0035.9+5949	1ES 0033+595	8.96935	59.83459	0.010	0.018	BLL	HSP	17.120	17.120	...	1.000	0.935	0.979
J0047.0+5658	GB6 J0047+5657	11.75179	56.96178	0.013	0.040	BLL	...	...	...	0.74700	1.000	0.910	...
J0047.9+5447	1RXS J004754.5+544758	11.96611	54.79579	0.010	0.060	BCU II	HSP	15.896	15.896	...	...	...	0.890
J0102.8+5825	TXS 0059+581	15.69068	58.40309	0.023	0.020	FSRQ	LSP	12.725	12.941	0.64400	0.999	0.956	...
J0103.4+5336	1RXS J010325.9+533721	15.85816	53.62036	0.006	0.042	BLL	...	...	...	...	...	0.824	0.934
J0109.8+6132	TXS 0106+612	17.44310	61.55846	0.015	0.033	FSRQ	LSP	13.290	13.541	0.78300	0.999	0.934	...
J0110.2+6806	4C +67.04	17.55364	68.09478	0.022	0.023	BLL	ISP	14.864	14.864	...	1.000	0.972	0.895
J0131.2+6120	1RXS J013106.4+612035	22.78011	61.34260	0.013	0.022	BLL	HSP	16.300	16.300	...	0.999	0.850	0.979
J0131.3+5548	TXS 0128+554	22.80760	55.75361	0.056	0.082	BCU I	...	...	...	0.03649	0.986	0.828	0.806
J0135.0+6927	TXS 0130+691	23.66984	69.41969	0.055	0.095	BCU III	...	...	...	...	0.984	0.830	...
J0137.8+5813	1RXS J013748.0+581422	24.46032	58.23648	0.005	0.032	BCU I	HSP	16.580	16.580	...	0.999	0.921	0.969
J0148.3+5200	GB6 J0148+5202	27.08473	52.03470	0.025	0.039	BCU III	...	...	...	...	0.996	...	...
J0153.4+7114	TXS 0149+710	28.35771	71.25180	0.010	0.037	BCU I	HSP	15.690	15.699	0.02200	1.000	0.953	0.930
J0211.7+5402	TXS 0207+538	32.73495	54.08692	0.120	0.128	BCU III	...	...	...	...	...	0.827	...
J0214.4+5143	TXS 0210+515	33.57473	51.74776	0.034	0.044	BLL	HSP	15.020	15.041	0.04900	0.999	0.905	0.944
J0217.3+6209	TXS 0213+619	34.26049	62.19274	0.056	0.102	BCU III	...	...	...	...	...	0.800	...
J0223.3+6820	NVSS J022304+682154	35.76891	68.36528	0.031	0.037	BCU II	HSP	15.800	15.800	...	0.991	...	...
J0223.5+6313	TXS 0219+628	35.87363	63.12177	0.104	0.152	BCU III	...	...	...	...	0.945	...	...
J0228.5+6703	GB6 J0229+6706	37.34410	67.11042	0.099	0.166	BCU III	...	...	...	...	0.953	...	...
J0241.3+6542	TXS 0237+655	40.34061	65.71988	0.018	0.043	BCU II	HSP	15.500	15.500	...	...	0.903	0.910
J0250.6+5630	NVSS J025047+562935	42.69830	56.49317	0.030	0.052	BCU II	HSP	16.138	16.138	...	...	...	0.890
J0253.8+5104	NVSS J025357+510256	43.49003	51.04902	0.022	0.075	FSRQ	LSP	12.500	12.936	1.73200	1.000	0.912	...
J0302.0+5335	GB6 J0302+5331	45.59473	53.52958	0.081	0.076	BCU II	HSP	15.988	15.988	...	0.965	...	...
J0303.6+4716	4C +47.08	45.89684	47.27119	0.017	0.031	BLL	ISP	14.000	14.000	...	1.000	0.965	...
J0304.9+6817	TXS 0259+681	46.09168	68.36041	0.082	0.076	BCU II	LSP	12.725	12.725	...	0.911	0.920	...
J0332.0+6308	GB6 J0331+6307	52.97465	63.13727	0.016	0.051	BCU II	ISP	14.150	14.150	...	0.998	0.816	...
J0333.9+6538	TXS 0329+654	53.48641	65.61561	0.022	0.034	BLL	HSP	15.200	15.200	...	0.998	0.924	0.885
J0352.9+5655	GB6 J0353+5654	58.28989	56.90859	0.032	0.046	BCU II	HSP	16.315	16.315	...	0.996	0.820	...
J0354.1+4643	B3 0350+465	58.62505	46.72188	0.065	0.118	BCU III	...	...	...	...	0.977	0.904	...
J0358.8+6002	TXS 0354+599	59.76100	60.08946	0.055	0.121	FSRQ	LSP	12.905	13.068	0.45500	0.993	0.919	0.830
J0418.5+3813	3C 111	64.58866	38.02661	0.198	0.168	RDG	...	...	...	0.04850	0.961	0.949	0.807
J0423.8+4150	4C +41.11	65.98337	41.83409	0.012	0.021	BLL	...	13.180	13.180	...	1.000	0.980	...
J0425.2+6319	1RXS J042523.0+632016	66.35324	63.33486	0.019	0.040	BCU II	HSP	16.050	16.050	...	...	0.804	0.920
J0444.5+3425	B2 0441+34	71.15083	34.42877	0.014	0.074	BCU II	LSP	13.005	13.005	...	0.997	0.880	...
J0501.8+3046	1RXS J050140.8+304831	75.42145	30.80727	0.051	0.059	BCU II	HSP	16.100	16.100	...	...	...	0.886
J0502.7+3438	MG2 J050234+3436	75.62478	34.60960	0.064	0.078	BCU III	...	...	...	...	0.983	0.820	...
J0503.4+4522	1RXS J050339.8+451715	75.91491	45.28320	0.098	0.086	BCU II	HSP	15.645	15.645	...	...	...	0.844
J0512.2+2918	B2 0509+29	78.17586	29.45100	0.170	0.527	BCU III	...	...	...	...	0.891	...	...
J0512.9+4038	B3 0509+406	78.21893	40.69545	0.054	0.073	BCU II	LSP	13.635	13.635	...	0.999	0.933	...
J0517.4+4540	4C +45.08	79.37041	45.61802	0.050	0.154	FSRQ	LSP	12.900	13.165	0.83900	0.990	0.907	...
J0519.3+2746	4C +27.15	79.88761	27.73454	0.051	0.110	BCU III	...	...	...	...	0.992	0.944	...
J0521.7+2113	TXS 0518+211	80.44152	21.21429	0.008	0.014	BLL	ISP	14.335	14.380	0.10800	1.000	0.969	0.961
J0526.0+4253	NVSS J052520+425520	81.33690	42.92225	0.140	0.150	BCU II	LSP	13.145	13.145	...	0.942	...	...
J0528.3+1815	1RXS J052829.6+181657	82.12341	18.28188	0.048	0.060	BCU III	...	...	...	...	...	...	0.929
J0533.2+4822	TXS 0529+483	83.31611	48.38134	0.007	0.031	FSRQ	LSP	13.040	13.375	1.16200	1.000	0.950	0.876

Table 6
(Continued)

3FGL Source Name	Counterpart Name	R.A. (°)	Decl. (°)	AngSep (°)	θ_{95} (°)	Optical Class	SED Class	$\log(\nu_{\rm peak}^{\rm S,meas})$	$\log(\nu_{\rm peak}^{\rm S})$	z	Prob. Bay.	Rel. $\mathrm{LR_{RG}}$	Rel. $\mathrm{LR_{XG}}$
(1)	(2)	(3)	(4)	(5)	(6)	(7)	(8)	(9)	(10)	(11)	(12)	(13)	(14)
J0539.8+1434	TXS 0536+145	84.92652	14.56266	0.031	0.071	FSRQ	LSP	12.445	13.012	2.69000	0.999	0.911	⋯
J0601.0+3837	B2 0557+38	90.26196	38.64144	0.017	0.053	BLL	LSP	13.810	13.810	⋯	⋯	0.945	⋯
J0603.8+2155	4C +22.12	90.96482	21.99381	0.066	0.058	BCU II	LSP	13.250	13.250	⋯	0.981	0.955	⋯
J0611.7+2759	GB6 J0611+2803	92.93284	28.06449	0.067	0.107	BCU III	⋯	⋯	⋯	⋯	0.991	⋯	⋯
J0620.4+2644	RX J0620.6+2644	95.16716	26.72524	0.044	0.063	BCU II	HSP	16.085	16.085	⋯	⋯	0.805	0.940
J0622.9+3326	B2 0619+33	95.71759	33.43622	0.014	0.018	BCU II	ISP	14.050	14.050	⋯	0.999	0.938	⋯
J0623.3+3043	GB6 J0623+3045	95.81747	30.74889	0.025	0.065	BCU II	ISP	14.790	14.790	⋯	0.996	0.800	⋯
J0631.2+2019	TXS 0628+203	97.75443	20.34978	0.050	0.106	BCU II	HSP	15.000	15.000	⋯	0.990	0.862	⋯
J0640.0−1252	TXS 0637−128	100.02993	−12.88761	0.015	0.040	BCU II	HSP	16.050	16.050	⋯	0.998	0.915	0.967
J0641.8−0319	TXS 0639−032	100.46305	−3.34683	0.029	0.142	BCU II	LSP	12.760	12.760	⋯	0.987	0.920	⋯
J0643.2+0859	PMN J0643+0857	100.86019	8.96056	0.066	0.063	FSRQ	LSP	13.000	13.275	0.88200	0.975	⋯	⋯
J0648.1+1606	1RXS J064814.1+160708	102.05790	16.11576	0.018	0.045	BCU II	HSP	16.300	16.300	⋯	⋯	⋯	0.904
J0648.8+1516	RX J0648.7+1516	102.19854	15.27355	0.007	0.029	BLL	HSP	15.850	15.922	0.17900	1.000	0.892	0.976
J0648.8−1740	TXS 0646−176	102.11874	−17.73484	0.109	0.155	FSRQ	LSP	12.480	12.829	1.23200	0.995	0.898	⋯
J0650.4−1636	PKS 0648−16	102.60242	−16.62770	0.019	0.094	BCU II	LSP	11.465	11.465	⋯	0.998	0.954	⋯
J0650.5+2055	1RXS J065033.9+205603	102.64681	20.93242	0.003	0.040	BCU II	HSP	15.650	15.650	⋯	⋯	⋯	0.892
J0654.5+0926	RX J0654.3+0925	103.61306	9.42644	0.032	0.231	BCU II	HSP	15.350	15.350	⋯	⋯	⋯	0.840
J0656.2−0323	TXS 0653−033	104.04634	−3.38522	0.009	0.053	FSRQ	LSP	13.495	13.708	0.63400	1.000	0.929	⋯
J0658.6+0636	NVSS J065844+063711	104.68735	6.61943	0.039	0.068	BCU II	HSP	15.000	15.000	⋯	0.999	⋯	⋯
J0700.0+1709	TXS 0657+172	105.00636	17.15603	0.016	0.116	BCU II	LSP	12.725	12.725	⋯	0.999	0.910	⋯
J0700.2+1304	GB6 J0700+1304	105.05963	13.07345	0.013	0.065	BCU II	HSP	15.425	15.425	⋯	0.998	⋯	⋯
J0702.7−1952	TXS 0700−197	105.67875	−19.85612	0.015	0.053	BLL	ISP	14.050	14.050	⋯	0.999	0.937	⋯
J0709.7−0256	PMN J0709−0255	107.43773	−2.92153	0.019	0.039	BLL	LSP	12.830	13.223	1.47200	0.998	0.898	⋯
J0721.4+0404	PMN J0721+0406	110.34963	4.11228	0.041	0.082	FSRQ	LSP	12.700	12.921	0.66500	0.999	0.881	⋯
J0723.2−0728	1RXS J072259.5−073131	110.74895	−7.52649	0.079	0.090	BCU III	⋯	⋯	⋯	⋯	0.976	⋯	0.899
J0725.8−0054	PKS 0723−008	111.46100	−0.91571	0.010	0.044	BCU I	LSP	13.355	13.407	0.12800	1.000	0.967	⋯
J0729.5−3127	NVSS J072922−313128	112.34570	−31.52438	0.078	0.157	BCU II	LSP	13.133	13.133	⋯	0.979	⋯	⋯
J0730.2−1141	PKS 0727−11	112.57964	−11.68683	0.006	0.013	FSRQ	LSP	12.300	12.713	1.58900	1.000	0.989	⋯
J0730.5−0537	TXS 0728−054	112.61849	−5.59636	0.027	0.050	BCU II	HSP	15.200	15.200	⋯	0.997	0.882	⋯
J0744.1−3804	PMN J0743−3804	115.93736	−38.06650	0.080	0.269	BCU III	⋯	⋯	⋯	⋯	0.936	⋯	⋯
J0744.8−4028	PMN J0744−4032	116.15929	−40.53806	0.083	0.078	BCU II	LSP	12.620	12.620	⋯	0.872	⋯	⋯
J0746.6−0706	PMN J0746−0709	116.61456	−7.16379	0.067	0.098	BCU II	ISP	14.230	14.230	⋯	0.983	⋯	⋯
J0747.2−3311	PKS 0745−330	116.83201	−33.17971	0.016	0.033	BCU II	LSP	13.850	13.850	⋯	1.000	0.958	⋯
J0748.0−1639	TXS 0745−165	117.01285	−16.66396	0.009	0.125	BCU II	LSP	11.920	11.920	⋯	0.997	0.915	⋯
J0754.4−1148	TXS 0752−116	118.61024	−11.78804	0.027	0.039	BLL	LSP	13.355	13.355	⋯	1.000	0.953	⋯
J0804.0−3629	NVSS J080405−362919	121.02237	−36.48863	0.008	0.045	BCU II	HSP	15.920	15.920	⋯	0.999	0.852	⋯
J0816.7−2421	PMN J0816−2421	124.16838	−24.35183	0.012	0.073	BCU II	LSP	12.340	12.340	⋯	0.999	0.873	⋯
J0825.8−3217	PKS 0823−321	126.46405	−32.30645	0.023	0.066	BCU II	ISP	14.030	14.030	⋯	0.999	0.914	⋯
J0825.9−2230	PKS 0823−223	126.50655	−22.50756	0.008	0.018	BLL	ISP	14.160	14.441	0.91100	1.000	0.966	0.947
J0828.8−2420	NVSS J082841−241850	127.17383	−24.31403	0.041	0.098	BCU III	⋯	⋯	⋯	⋯	⋯	0.853	⋯
J0841.3−3554	NVSS J084121−355506	130.34017	−35.91823	0.014	0.027	BCU II	HSP	15.956	15.956	⋯	1.000	0.892	⋯
J0845.1−5458	PMN J0845−5458	131.26034	−54.96904	0.021	0.039	BCU II	LSP	13.005	13.005	⋯	1.000	0.981	0.828
J0849.5−2912	NVSS J084922−291149	132.34210	−29.19734	0.043	0.064	BCU II	ISP	14.504	14.504	⋯	0.988	⋯	⋯
J0849.9−3540	PMN J0849−3541	132.44010	−35.68369	0.034	0.052	BCU II	LSP	12.900	12.900	⋯	1.000	0.913	⋯
J0852.6−5756	PMN J0852−5755	133.16136	−57.92495	0.022	0.050	BCU II	LSP	13.076	13.076	⋯	0.999	⋯	0.858
J0853.0−3654	NVSS J085310−365820	133.29384	−36.97236	0.061	0.047	BCU II	HSP	15.660	15.660	⋯	0.883	0.810	⋯
J0858.1−3130	1RXS J085802.6−313043	134.51195	−31.51118	0.029	0.091	BCU II	HSP	16.235	16.235	⋯	⋯	⋯	0.913
J0904.8−3516	NVSS J090442−351423	136.17658	−35.24010	0.053	0.084	BCU II	ISP	14.171	14.171	⋯	0.988	0.864	⋯

Table 6
(Continued)

3FGL Source Name (1)	Counterpart Name (2)	R.A. (°) (3)	Decl. (°) (4)	AngSep (°) (5)	θ_{95} (°) (6)	Optical Class (7)	SED Class (8)	$\log(\nu_{\mathrm{peak}}^{\mathrm{S,meas}})$ (9)	$\log(\nu_{\mathrm{peak}}^{\mathrm{S}})$ (10)	z (11)	Prob. Bay. (12)	Rel. LR$_{\mathrm{RG}}$ (13)	Rel. LR$_{\mathrm{XG}}$ (14)
J0904.8–5734	PKS 0903–57	136.22158	−57.58494	0.015	0.030	BCU I	ISP	14.664	14.893	0.69500	1.000	1.000	⋯
J0922.8–3959	PKS 0920–39	140.69341	−39.99307	0.017	0.165	BCU II	LSP	13.775	13.775	⋯	0.999	0.948	⋯
J0940.7–6102	MRC 0939–608	145.19733	−61.12455	0.078	0.158	BCU II	LSP	13.671	13.671	⋯	0.984	0.897	⋯
J0956.7–6441	AT20G J095612–643928	149.05075	−64.65781	0.067	0.087	BCU II	LSP	13.285	13.285	⋯	0.928	⋯	⋯
J1005.0–4959	PMN J1006–5018	151.55837	−50.30374	0.370	0.197	BCU II	LSP	12.140	12.140	⋯	⋯	1.000	⋯
J1015.2–4512	PMN J1014–4508	153.70981	−45.14477	0.097	0.101	BCU II	LSP	12.025	12.025	⋯	0.986	0.900	⋯
J1038.9–5311	MRC 1036–529	159.66941	−53.19535	0.040	0.057	BCU II	LSP	12.235	12.235	⋯	0.998	1.000	⋯
J1047.8–6216	PMN J1047–6217	161.92897	−62.28740	0.016	0.044	BCU II	LSP	12.200	12.200	⋯	0.999	1.000	⋯
J1051.5–6517	PKS 1049–650	162.84800	−65.30240	0.017	0.063	BCU II	ISP	14.030	14.030	⋯	0.998	⋯	⋯
J1103.9–5357	PKS 1101–536	165.96759	−53.95019	0.007	0.028	BLL	LSP	13.830	13.830	⋯	0.999	0.984	⋯
J1123.2–6415	AT20G J112319–641735	170.83090	−64.29339	0.034	0.078	BCU III	⋯	⋯	⋯	⋯	0.995	0.931	⋯
J1136.6–6826	PKS 1133–681	174.00874	−68.45162	0.062	0.105	BCU III	⋯	⋯	⋯	⋯	0.987	0.932	⋯
J1229.8–5305	AT20G J122939–530332	187.41637	−53.05894	0.046	0.116	BCU III	⋯	⋯	⋯	⋯	0.991	⋯	⋯
J1233.9–5736	AT20G J123407–573552	188.52933	−57.59803	0.019	0.036	BCU II	ISP	14.700	14.700	⋯	0.998	⋯	⋯
J1256.1–5919	PMN J1256–5919	194.02043	−59.32886	0.013	0.054	BCU III	⋯	⋯	⋯	⋯	0.998	⋯	⋯
J1304.3–5535	PMN J1303–5540	195.95507	−55.67545	0.119	0.132	BCU II	LSP	12.725	12.725	⋯	0.974	0.908	⋯
J1308.1–6707	PKS 1304–668	197.07240	−67.11812	0.012	0.053	BCU II	ISP	14.230	14.230	⋯	0.998	0.973	⋯
J1315.1–5329	PMN J1315–5334	198.76742	−53.57663	0.089	0.069	BCU I	LSP	13.775	13.775	⋯	0.959	0.912	⋯
J1326.6–5256	PMN J1326–5256	201.70512	−52.93990	0.025	0.043	BLL	LSP	12.559	12.559	⋯	0.999	1.000	⋯
J1328.9–5607	PMN J1329–5608	202.25477	−56.13407	0.009	0.022	BCU I	LSP	12.930	12.930	⋯	1.000	0.990	⋯
J1330.1–7002	PKS 1326–697	202.54615	−70.05363	0.008	0.031	BCU II	LSP	13.425	13.425	⋯	1.000	0.977	⋯
J1346.6–6027	Cen B	206.70435	−60.40815	0.052	0.051	RDG	ISP	14.762	14.762	0.01292	1.000	1.000	⋯
J1353.5–6640	1RXS J135341.1–664002	208.41726	−66.66602	0.011	0.037	BLL	HSP	15.700	15.700	⋯	1.000	⋯	0.963
J1400.7–5605	PMN J1400–5605	210.17407	−56.08210	0.009	0.121	BCU II	LSP	12.280	12.280	⋯	0.997	⋯	⋯
J1413.2–6518	Circinus galaxy	213.29172	−65.34571	0.043	0.119	sy	HSP	15.440	15.440	⋯	0.988	⋯	0.886
J1419.1–5156	PMN J1419–5155	214.89685	−51.91627	0.079	0.143	BCU II	LSP	12.550	12.550	⋯	0.993	0.921	⋯
J1424.6–6807	PKS 1420–679	216.23149	−68.13280	0.027	0.059	BCU II	LSP	12.480	12.480	⋯	1.000	1.000	⋯
J1503.7–6426	AT20G J150350–642539	225.95892	−64.42764	0.025	0.046	BCU II	LSP	13.285	13.285	⋯	0.997	⋯	⋯
J1508.7–4956	PMN J1508–4953	227.16227	−49.88398	0.051	0.087	BCU II	LSP	11.780	11.780	⋯	0.999	0.956	⋯
J1514.5–4750	PMN J1514–4748	228.66677	−47.80829	0.032	0.063	FSRQ	LSP	12.515	12.922	1.55120	0.999	0.963	⋯
J1525.2–5905	PMN J1524–5903	231.21301	−59.06103	0.060	0.206	BCU II	LSP	12.655	12.655	⋯	0.986	0.848	⋯
J1558.9–6432	PMN J1558–6432	239.70952	−64.54157	0.012	0.030	BLL	HSP	15.300	15.333	0.07958	1.000	0.977	0.937
J1600.3–5810	MRC 1556–580	240.05157	−58.18416	0.020	0.078	BCU III	⋯	⋯	⋯	⋯	0.998	0.952	⋯
J1603.9–4903	PMN J1603–4904	240.96119	−49.06820	0.012	0.014	BLL	ISP	14.615	14.615	⋯	1.000	0.988	⋯
J1604.4–4442	PMN J1604–4441	241.12925	−44.69221	0.027	0.038	BCU I	LSP	12.947	12.947	⋯	0.999	1.000	⋯
J1610.6–3956	PMN J1610–3958	242.59116	−39.98287	0.061	0.183	FSRQ	LSP	13.088	13.269	0.51800	0.999	0.868	⋯
J1617.4–5846	MRC 1613–586	244.32455	−58.80218	0.041	0.073	FSRQ	LSP	12.550	12.550	1.42200	0.996	1.000	0.844
J1637.6–3449	NVSS J163750–344915	249.46249	−34.82098	0.039	0.042	BCU II	LSP	13.000	13.000	⋯	0.983	0.843	0.879
J1645.2–5747	AT20G J164513–575122	251.30595	−57.85622	0.067	0.109	BCU III	⋯	⋯	⋯	⋯	0.979	⋯	⋯
J1648.5–4829	PMN J1648–4826	252.19968	−48.43856	0.064	0.139	BCU III	⋯	⋯	⋯	⋯	0.993	⋯	⋯
J1650.2–5044	PMN J1650–5044	252.56928	−50.74673	0.004	0.023	BCU I	LSP	12.725	12.725	⋯	1.000	1.000	⋯
J1656.2–3303	Swift J1656.3–3302	254.07025	−33.03633	0.016	0.118	FSRQ	LSP	12.648	13.179	2.40000	1.000	0.883	⋯
J1659.7–3132	NVSS J165949–313047	254.95383	−31.51325	0.036	0.090	BCU II	LSP	13.110	13.110	⋯	0.998	0.858	⋯
J1711.5–5029	PMN J1711–5028	257.92080	−50.47150	0.023	0.079	BCU II	LSP	13.390	13.390	⋯	0.997	⋯	⋯
J1717.4–5157	PMN J1717–5155	259.39455	−51.92553	0.044	0.076	FSRQ	LSP	12.836	13.170	1.15800	0.990	⋯	⋯
J1717.8–3342	TXS 1714–336	259.40012	−33.70245	0.042	0.036	BLL	LSP	12.865	12.865	⋯	1.000	0.922	⋯
J1718.1–3056	PMN J1718–3056	259.52173	−30.93753	0.007	0.062	BCU III	⋯	⋯	⋯	⋯	0.998	0.880	⋯
J1731.8–3001	NVSS J173146–300309	262.94538	−30.05255	0.035	0.035	BLL	⋯	⋯	⋯	⋯	0.994	0.841	⋯

Table 6
(Continued)

3FGL Source Name (1)	Counterpart Name (2)	R.A. (°) (3)	Decl. (°) (4)	AngSep (°) (5)	θ_{95} (°) (6)	Optical Class (7)	SED Class (8)	$\log(\nu_{\rm peak}^{\rm S,meas})$ (9)	$\log(\nu_{\rm peak}^{\rm S})$ (10)	z (11)	Prob. Bay. (12)	Rel. $LR_{\rm RG}$ (13)	Rel. $LR_{\rm XG}$ (14)
J1741.9−2539	NVSS J174154−253743	265.47687	−25.62872	0.034	0.044	BCU III	...	...	...	...	0.994	0.813	...
J1744.9−1725	1RXS J174459.5−172640	266.24914	−17.44348	0.011	0.037	BCU III	...	...	...	...	...	0.837	0.963
J1802.6−3940	PMN J1802−3940	270.67783	−39.66886	0.006	0.017	FSRQ	LSP	12.445	12.810	1.31900	1.000	0.985	...
J1823.6−3453	NVSS J182338−345412	275.91079	−34.90334	0.009	0.024	BCU II	HSP	16.140	16.140	...	1.000	0.925	0.983
J1828.9−2417	1RXS J182853.8−241746	277.22879	−24.29344	0.015	0.053	BCU I	HSP	16.456	16.456	...	...	0.872	0.914
J1830.1+0617	TXS 1827+062	277.52475	6.32110	0.032	0.045	FSRQ	LSP	12.305	12.547	0.74500	0.999	0.920	...
J1831.0−2714	PMN J1831−2714	277.75019	−27.23505	0.012	0.114	BCU III	...	...	...	...	0.994	0.810	...
J1833.6−2103	PKS 1830−211	278.41619	−21.06126	0.007	0.014	FSRQ	LSP	12.585	13.130	2.50700	1.000	0.994	0.939
J1835.4+1349	TXS 1833+137	278.89730	13.81354	0.039	0.118	BCU III	...	...	...	...	0.991	...	...
J1844.3+1547	NVSS J184425+154646	281.10567	15.77940	0.022	0.039	BCU II	ISP	14.708	14.708	...	0.998	0.867	...
J1849.3−1645	1RXS J184919.7−164726	282.33110	−16.78999	0.026	0.053	BCU III	...	...	...	...	...	...	0.907
J1908.8−0130	NVSS J190836−012642	287.15393	−1.44532	0.086	0.074	BCU II	LSP	11.782	11.782	...	0.996	...	...
J1910.8+2855	1RXS J191053.2+285622	287.71764	28.93926	0.012	0.048	BCU II	HSP	16.910	16.910	...	...	...	0.942
J1912.0−0804	PMN J1912−0804	288.02970	−8.07275	0.010	0.077	BCU II	HSP	15.050	15.050	...	0.999	0.905	...
J1924.9+2817	NVSS J192502+281542	291.25942	28.26172	0.043	0.056	BCU II	HSP	15.850	15.850	...	...	0.800	0.906
J1925.7+1228	TXS 1923+123	291.42007	12.46058	0.011	0.115	BCU III	...	...	...	...	0.992	0.808	...
J1931.1+0937	RX J1931.1+0937	292.78819	9.62119	0.010	0.020	BLL	HSP	16.150	16.150	...	1.000	0.860	0.980
J1933.4+0727	1RXS J193320.3+072616	293.33459	7.43941	0.030	0.074	BCU II	HSP	15.980	15.980	...	0.998	0.823	0.899
J1942.7+1033	1RXS J194246.3+103339	295.69785	10.55753	0.009	0.023	BCU II	HSP	15.435	15.435	...	1.000	0.917	0.958
J1949.0+1312	87 GB 194635.4+130713	297.23037	13.24400	0.043	0.051	BCU II	HSP	15.450	15.450	...	...	0.836	...
J1955.1+1357	87 GB 195252.4+135009	298.79821	13.97118	0.017	0.052	FSRQ	LSP	12.865	13.106	0.74300	1.000	0.885	...
J2000.1+4212	MG4 J195957+4213	299.99487	42.22965	0.032	0.063	BCU II	LSP	12.550	12.550	...	0.997	0.897	...
J2001.1+4352	MG4 J200112+4352	300.30364	43.88134	0.005	0.012	BLL	HSP	15.205	15.205	...	1.000	0.944	...
J2012.0+4629	7C 2010+4619	303.02349	46.48216	0.020	0.026	BLL	ISP	14.958	14.958	...	1.000	0.954	0.967
J2015.6+3709	MG2 J201534+3710	303.86971	37.18320	0.038	0.027	FSRQ	LSP	12.743	13.012	0.85900	0.994	0.961	...
J2018.5+3851	TXS 2016+386	304.62927	38.85538	0.005	0.048	BCU II	LSP	13.508	13.508	...	0.998	0.910	...
J2023.2+3154	4C +31.56	305.82924	31.88397	0.028	0.090	BCU I	LSP	13.382	13.514	0.35600	0.998	0.967	...
J2025.2+3340	B2 2023+33	306.29518	33.71673	0.053	0.052	BCU I	LSP	12.305	12.391	0.21900	0.999	0.942	...
J2029.4+4923	MG4 J202932+4925	307.41614	49.43949	0.055	0.058	BLL	LSP	13.320	13.320	...	0.968	...	...
J2038.8+5113	3C 418	309.65431	51.32018	0.104	0.110	FSRQ	LSP	12.480	12.909	1.68600	0.996	0.962	...
J2039.5+5217	1ES 2037+521	309.84799	52.33056	0.043	0.062	BLL	HSP	16.448	16.470	0.05300	1.000	...	0.895
J2056.7+4938	RGB J2056+496	314.17808	49.66850	0.027	0.027	BCU II	HSP	15.742	15.742	...	0.995	0.894	0.957
J2108.0+3654	TXS 2106+367	317.02275	36.92404	0.018	0.059	BCU II	ISP	14.860	14.860	...	...	0.837	...
J2110.3+3540	B2 2107+35A	317.38283	35.54933	0.203	0.246	BCU II	ISP	14.048	14.048	...	0.989	0.862	0.836
J2201.7+5047	NRAO 676	330.43141	50.81566	0.016	0.042	FSRQ	LSP	12.515	12.977	1.89900	1.000	0.955	...
J2347.0+5142	1ES 2344+514	356.77015	51.70497	0.005	0.018	BLL	HSP	15.850	15.869	0.04400	1.000	0.953	0.980
J2347.9+5436	NVSS J234753+543627	356.97138	54.60754	0.007	0.066	BCU II	HSP	16.400	16.400	...	...	...	0.925

Note. Columns 1 and 2 are the 3FGL and counterpart names, columns 3 and 4 are the counterpart J2000 coordinates, column 5 gives the angular separation between the gamma-ray and counterpart positions, column 6 is the 95% error radius on the gamma-ray position, column 7 lists the optical class, column 8 is the spectral energy distribution (SED) class (depending on the synchrotron peak frequency given in column 9), column 10 is the synchrotron peak frequency corrected for the redshift shown in column 11, and columns 12–14 report the probability for the Bayesian method and the two reliability values, $LR_{\rm RG}$ and $LR_{\rm XG}$, for the radio–gamma-ray match and the X-ray–gamma-ray match, respectively.

(This table is available in machine-readable form.)

Table 7
Sources from Earlier FGL Catalogs Missing in 3LAC

Counterpart Name (1)	R.A. (°) (2)	Decl. (°) (3)	Optical Class (4)	SED Class (5)	Redshift (6)	1FGL Name (7)	2FGL Name (8)
CRATES J0009+0628	2.26638	6.47256	BLL	LSP	⋯	1FGL J0008.9+0635	⋯
CGRaBS J0011+0057	2.87667	0.96439	FSRQ	LSP	1.492	1FGL J0011.1+0050	⋯
GB6 J0013+1910	3.48509906	19.1782456	BLL	⋯	0.473	⋯	2FGL J0013.8+1907
PKS 0056−572	14.6940417	−56.98675	BCU	LSP	⋯	⋯	2FGL J0059.7−5700
PKS 0116−219	19.73858	−21.69167	FSRQ	LSP	1.165	1FGL J0118.7−2137	⋯
TXS 0154−244	29.1237238	−24.2146961	BCU	⋯	⋯	⋯	2FGL J0156.5−2419
S5 0159+723	30.8883864	72.5483361	BLL	LSP	⋯	1FGL J0203.5+7234	2FGL J0203.6+7235
B2 0200+30	30.93898	30.69142	⋯	⋯	⋯	1FGL J0203.5+3044	⋯
1RXS J021905.8−172503	34.772989	−17.4204904	BLL	HSP	0.128	⋯	2FGL J0219.1−1725
NGC 1068	40.6696759	−0.013268027	starburst	⋯	0.00419	⋯	2FGL J0242.5+0006
CRATES J0258+2030	44.53046	20.50044	BLL	LSP	⋯	1FGL J0258.0+2033	⋯
CRATES J0305−0607	46.25238	−6.12819	BLL	⋯	⋯	1FGL J0305.0−0601	⋯
NVSS J033223−111951	53.0970024	−11.3309802	BCU	HSP	⋯	⋯	2FGL J0332.5−1118
PMN J0413−5332	63.30629	−53.53361	FSRQ	⋯	1.027	1FGL J0413.4−5334	2FGL J0413.5−5332
PKS 0420+022	65.71754	2.32414	FSRQ	LSP	2.277	1FGL J0422.1+0211	⋯
GB6 J0437+6757	69.3862329	67.9544125	BCU	⋯	⋯	⋯	2FGL J0436.2+6759
PKS 0437−322	69.8915847	−32.169605	BCU	LSP	⋯	⋯	2FGL J0440.1−3211
TXS 0437+145	70.0879763	14.6324959	BCU	⋯	⋯	⋯	2FGL J0440.4+1433
PKS 0440−00	70.6609229	−0.295256342	FSRQ	LSP	0.844	⋯	2FGL J0442.7−0017
4C +06.21	74.28212	6.75203	FSRQ	LSP	0.405	1FGL J0457.9+0649	⋯
1WGA J0506.6−0857	76.6662037	−8.96713326	BLL	HSP	⋯	⋯	2FGL J0506.5−0901
PMN J0507−6104	76.9772083	−61.0786389	FSRQ	⋯	1.089	⋯	2FGL J0507.5−6102
PKS 0514−459	78.9367917	−45.9455	FSRQ	LSP	0.194	⋯	2FGL J0516.5−4601
OG 050	83.1625	7.54536	FSRQ	LSP	1.254	1FGL J0532.9+0733	⋯
PMN J0533−7216	83.4342917	−72.2730278	BCU	⋯	⋯	⋯	2FGL J0532.5−7223
FRBA J0536−3343	84.12131	−33.71737	BLL	HSP	⋯	1FGL J0536.2−3348	⋯
SUMSS J053748−571828	84.4532083	−57.3080278	BCU	ISP	⋯	⋯	2FGL J0537.7−5716
CRATES J0539−0356	84.81454	−3.94892	⋯	⋯	⋯	1FGL J0539.4−0400	⋯
PKS 0539−057	85.40867	−5.69706	FSRQ	LSP	0.839	1FGL J0540.9−0547	⋯
PMN J0608−1520	92.0062923	−15.3436112	FSRQ	LSP	1.094	1FGL J0608.0−1521	2FGL J0608.0−1521
PMN J0610−1847	92.5746761	−18.7944297	BLL	LSP	⋯	⋯	2FGL J0609.6−1847
CGRaBS J0634−2335	98.7459773	−23.5866986	FSRQ	⋯	1.535	⋯	2FGL J0635.0−2334
BZU J0645+6024	101.25571	60.41175	AGN	⋯	0.832	1FGL J0645.5+6033	⋯
PKS 0700−465	105.39392	−46.57683	FSRQ	LSP	0.822	1FGL J0702.0−4628	⋯
MG2 J071354+1934	108.482006	19.5837737	FSRQ	LSP	0.54	1FGL J0714.0+1935	2FGL J0714.0+1933
BZB J0723+5841	110.80817	58.68844	BLL	HSP	⋯	1FGL J0722.3+5837	⋯
4C +14.23	111.32004	14.42047	FSRQ	⋯	1.038	1FGL J0725.3+1431	⋯
1RXS J073026.0+330727	112.608899	33.1227122	BLL	HSP	0.112	1FGL J0730.0+3305	2FGL J0729.9+3304
CGRaBS J0814+6431	123.66329	64.52278	BLL	ISP	⋯	1FGL J0815.0+6434	⋯
RX J0817.9+3243	124.461462	32.7277131	BLL	HSP	⋯	⋯	2FGL J0817.9+3238
RX J0819.2−0756	124.822975	−7.9411836	BLL	HSP	⋯	⋯	2FGL J0819.6−0803
4C +39.23	126.230974	39.2782392	FSRQ	LSP	1.216	⋯	2FGL J0824.7+3914
BZB J0842+0252	130.6063	2.88131	BLL	HSP	0.425	1FGL J0842.2+0251	⋯
TXS 0845−068	131.986571	−7.05500701	BLL	ISP	⋯	⋯	2FGL J0848.1−0703
GB6 J0850+4855	132.501843	48.9162398	BLL	ISP	⋯	1FGL J0849.9+4852	2FGL J0849.8+4852
GB6 J0856+7146	134.228226	71.7735317	BCU	LSP	⋯	⋯	2FGL J0856.0+7136
B3 0908+416B	138.048527	41.4358885	FSRQ	LSP	2.563	1FGL J0912.3+4127	2FGL J0912.1+4126
OK 630	140.40096	62.2645	FSRQ	LSP	1.446	1FGL J0919.6+6216	⋯
GB6 J0922+0433	140.612897	4.56042681	BCU	⋯	⋯	⋯	2FGL J0922.7+0435
GB6 J0934+3926	143.527628	39.4424247	BLL	⋯	⋯	1FGL J0934.5+3929	2FGL J0934.7+3932
RX J0940.3+6148	145.093673	61.8069546	BLL	HSP	0.211	1FGL J0941.2+6149	2FGL J0941.4+6148
BZB J0952+3936	148.06129	39.60442	BLL	HSP	⋯	1FGL J0952.2+3926	⋯
OK 290	149.207825	25.2543968	FSRQ	LSP	0.707969	1FGL J0956.9+2513	2FGL J0956.9+2516
PKS 1004−217	151.69338	−21.989	FSRQ	LSP	0.33	1FGL J1007.1−2157	⋯
PKS 1008−01	152.715672	−2.00533479	FSRQ	⋯	0.887	1FGL J1011.0−0156	2FGL J1010.8−0158
4C +23.24	153.696062	23.0201609	FSRQ	LSP	0.566	⋯	2FGL J1014.1+2306
PKS 1021−323	156.001761	−32.570915	FSRQ	⋯	1.568	⋯	2FGL J1023.8−3248
S5 1039+81	161.096173	80.911074	FSRQ	LSP	1.26	1FGL J1048.7+8054	2FGL J1042.6+8053
GB6 J1049+1548	162.413685	15.8105625	BCU	⋯	⋯	⋯	2FGL J1049.4+1551
1RXS J112551.6−074219	171.466497	−7.70598752	BLL	HSP	0.279	1FGL J1126.0−0741	2FGL J1126.0−0743
PKS 1124−186	171.768399	−18.9550553	FSRQ	LSP	1.048	⋯	2FGL J1126.6−1856
PKS 1133−739	174.039417	−74.2635	BCU	⋯	⋯	⋯	2FGL J1134.4−7415

18

Table 7
(Continued)

Counterpart Name (1)	R.A. (°) (2)	Decl. (°) (3)	Optical Class (4)	SED Class (5)	Redshift (6)	1FGL Name (7)	2FGL Name (8)
S4 1144+40	176.742963	39.9763205	FSRQ	⋯	1.0882	1FGL J1146.8+4004	2FGL J1146.9+4000
PKS 1217+02	185.051316	2.06154225	FSRQ	ISP	0.241	⋯	2FGL J1219.7+0201
PMN J1226−1328	186.726778	−13.4774552	BLL	⋯	0.456	1FGL J1226.7−1332	2FGL J1226.7−1331
B2 1229+29	187.93158	28.79717	BLL	ISP	0.236	1FGL J1231.6+2850	⋯
5C 12.170	195.371521	33.6168978	BCU	⋯	1.00913	⋯	2FGL J1301.6+3331
NGC 4945	196.36446	−49.46806	AGN	⋯	0.002	1FGL J1305.4−4928	⋯
OP −034	200.65379	−9.62717	FSRQ	⋯	1.864	1FGL J1322.7−0943	⋯
1RXS 132928.0−053132	202.366669	−5.52568984	AGN	⋯	0.575868	⋯	2FGL J1329.3−0528
1ES 1421+582	215.66206	58.03208	BLL	HSP	⋯	1FGL J1422.2+5757	⋯
CLASS J1423+3737	215.76921	37.62516	BLL	⋯	⋯	1FGL J1422.7+3743	⋯
PMN J1509−4340	227.398167	−43.6753333	FSRQ	LSP	0.776	⋯	2FGL J1508.9−4342
CLASS J1537+8154	234.25036	81.90862	⋯	⋯	⋯	1FGL J1536.6+8200	⋯
1ES 1544+820	235.065419	81.918194	BLL	HSP	⋯	⋯	2FGL J1538.1+8159
4C -06.46	246.13717	−6.83047	⋯	⋯	⋯	1FGL J1624.7−0642	⋯
NGC 6251	248.13325	82.53789	AGN	⋯	0.025	1FGL J1635.4+8228	⋯
PMN J1657−1021	254.386346	−10.3545458	BCU	⋯	⋯	⋯	2FGL J1657.1−1027
CGRaBS J1703−6212	255.901667	−62.2111667	FSRQ	⋯	1.747	⋯	2FGL J1703.2−6217
PKS 1728+004	262.64583	0.41075	FSRQ	⋯	1.335	1FGL J1730.4+0008	⋯
CRATES J1803+0341	270.9845	3.68544	FSRQ	⋯	1.42	1FGL J1804.1+0336	⋯
87 GB 181007.0+533142	272.797216	53.5403097	BCU	⋯	⋯	⋯	2FGL J1811.0+5340
NVSS J181118+034114	272.825356	3.68726303	BLL	HSP	⋯	⋯	2FGL J1811.3+0339
PMN J1814−6412	273.65	−64.2148056	BCU	⋯	⋯	⋯	2FGL J1815.6−6407
PMN J1816−4943	274.233125	−49.7291389	BCU	⋯	⋯	⋯	2FGL J1816.7−4942
87 GB 182712.0+272717	277.308371	27.4841929	BCU	⋯	⋯	⋯	2FGL J1829.1+2725
B2 1846+32A	282.09208	32.31739	FSRQ	LSP	0.798	1FGL J1848.5+3224	⋯
TXS 1918−126	290.349727	−12.5317721	BLL	⋯	⋯	1FGL J1921.1−1234	2FGL J1921.3−1231
CRATES J1925−1018	291.26333	−10.30344	BLL	⋯	⋯	1FGL J1925.1−1018	⋯
NGC 6814	295.668824	−10.322184	Seyfert	⋯	0.0052	⋯	2FGL J1942.5−1024
3C 407	302.10161	−4.30814	AGN	⋯	0.589	1FGL J2008.6−0419	⋯
4C +72.28	302.468826	72.4887054	BLL	LSP	⋯	1FGL J2009.1+7228	2FGL J2009.7+7225
PKS 2012−017	303.81317	−1.62569	BLL	⋯	⋯	1FGL J2015.3−0129	⋯
CGRaBS J2022+7611	305.64829	76.19061	BLL	⋯	⋯	1FGL J2020.4+7608	⋯
CGRaBS J2025−2845	306.47337	−28.76353	⋯	LSP	⋯	1FGL J2025.9−2852	⋯
SDSS J205528.20−002117.2	313.86749	−0.35472	BLL	HSP	⋯	1FGL J2055.5−0023	⋯
PKS 2130−654	323.554542	−65.227	BCU	⋯	⋯	⋯	2FGL J2134.5−6513
RBS 1769	324.719865	−20.8962717	BLL	HSP	0.29	⋯	2FGL J2139.1−2054
4C +06.69	327.022834	6.96092391	FSRQ	LSP	0.999	1FGL J2148.5+0654	2FGL J2148.2+0659
CRATES J2212+0646	333.21183	6.76908	FSRQ	⋯	1.121	1FGL J2212.9+0654	⋯
NVSS J222329+010226	335.8732293	1.04070536	BCU	⋯	⋯	⋯	2FGL J2223.4+0104
1RXS 224642.0−520638	341.67575	−52.1114167	BCU	HSP	0.194	⋯	2FGL J2246.8−5203
PKS 2244−002	341.875756	0.001971181	BLL	ISP	0.949	1FGL J2247.3+0000	2FGL J2247.2−0002
PKS 2320−021	350.76929	−1.84669	FSRQ	⋯	1.774	1FGL J2322.3−0153	⋯
PKS 2325−408	352.080917	−40.5858333	BCU	⋯	⋯	⋯	2FGL J2327.9−4037
PKS 2329−16	352.911061	−15.949355	FSRQ	LSP	1.153	⋯	2FGL J2331.8−1607
CGRaBS J2345−1555	356.30192	−15.91883	FSRQ	LSP	0.621	1FGL J2344.6−1554	⋯

Note. Column 1 is the counterpart name, columns 2 and 3 are the counterpart J2000 coordinates, column 4 lists the optical class, column 5 is the spectral energy distribution (SED) class (depending on the synchrotron peak frequency), column 6 is the counterpart redshift, and columns 7 and 8 show the names in previous *Fermi*-LAT catalogs.

(This table is available in machine-readable form.)

and 9 other AGNs or BCUs detected in flaring, hardening, or enhanced activity states. Only one, PKS 1915−458 ($z = 2.47$, ATel#2666 and ATel#2679) is not listed in the 3FGL/3LAC or in previous LAT catalogs. This high-redshift FSRQ appears to only emit gamma-rays sporadically within short time intervals.

In addition, three LAT sources announced in ATels and not present in the 3LAC might have extragalactic source associations: *Fermi* J0052+1110 located at high Galactic latitude), PMN J1626−2426 (FSRQ in the vicinity of 3FGL J1626.2−2428 but outside its error ellipse and located behind an H II region), and PMN J0623−3350 (flat spectrum radio source reported as *Fermi* J0623−3351). A fourth LAT ATel source tentatively associated there with the FSRQ PKS 2136−642 is listed as 3FGL J2141.6−6412 in 3FGL but is now associated with the BCU PMN J2141−6411 that is separated ∼15′ from the former.
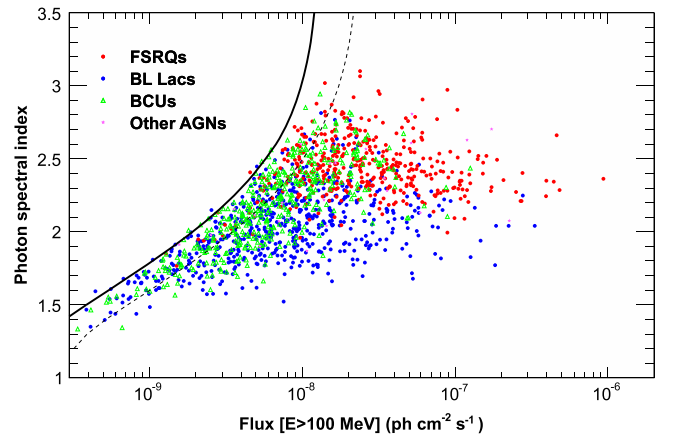
Figure 8. Photon spectral index vs. photon flux above 100 MeV for blazars in the Clean Sample. Red circles: FSRQs; blue circles: BL Lacs; green triangles: blazars of unknown type; magenta stars: other AGNs. The solid (dashed) curve represents the approximate 3FGL (2FGL) detection limit based on a typical exposure.
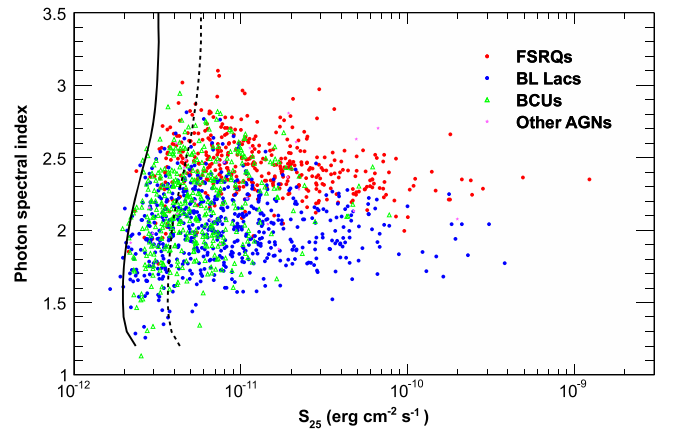

Figure 9. Photon spectral index vs. energy flux between 100 MeV and 100 GeV, S_{25}. Red circles: FSRQs; blue circles: BL Lacs; green triangles: blazars of unknown type; magenta stars: other AGNs. The solid (dashed) curve represents the approximate 3FGL (2FGL) detection limit based on a typical exposure.

Figure 7. Photon spectral index distributions. Top: FSRQs (solid: 2LAC sources; dashed: new 3LAC sources). Second from top: BL Lacs (solid: 2LAC sources; dashed: new 3LAC sources). Third from top: 3LAC LSP-BL Lacs (green), ISP-BL Lacs (light blue), and HSP-BL Lacs (dark blue). Bottom: blazars of unknown type (solid: 2LAC sources; dashed: new 3LAC sources).

5. PROPERTIES OF 3LAC SOURCES

5.1. Flux and Photon Spectral Index

Figure 7 displays the photon index distributions for the different blazar classes both for the sources previously listed in 2LAC and the newly detected sources. The newly detected FSRQs are slightly softer than the 2LAC ones (2.53 ± 0.03 versus 2.41 ± 0.01), indicating that the LAT gradually detects more lower energy-peaked blazars. In contrast, there is no significant spectral difference between the two sets of BL Lacs. For BCUs, the distribution of the new sources extends further out on the high-index end ($\Gamma > 2.4$), where the overlap with the BL Lac distribution becomes very small. The corresponding sources seem likely to be FSRQs.

Figures 8 and 9 show the photon index versus the photon flux and energy flux, respectively, together with estimated flux limits. As noted in 2LAC, the strong bias observed toward hard sources in the photon-flux limit essentially vanishes when considering the energy-flux limit above 100 MeV instead. (Note that this feature holds only for a lower bound of 100 MeV; other lower energy limits will bring about a dependence of the energy-flux limit on the spectral index.)

Figure 10 shows the position of the synchrotron peak $\nu^{\mathrm{S}}_{\mathrm{peak,meas}}$ versus the photon spectral index for FSRQs and BL Lacs with measured redshifts. The strong anticorrelation already observed in 1LAC and 2LAC is confirmed. Fitting a linear function $\Gamma = A + B \log(\nu^{\mathrm{S}}_{\mathrm{peak,rest}}/10^{14}\,\mathrm{Hz})$ yields $A = 2.25 \pm 0.04$ and $B = -0.18 \pm 0.03$. The mean and rms of the Γ distributions are 2.44 ± 0.20, 2.01 ± 0.25, 2.21 ± 0.18, 2.07 ± 0.20, and 1.87 ± 0.20 for FSRQs, the whole BL Lac sample, LSP-, ISP- and HSP-BL Lacs, respectively. FSRQs are overwhelmingly of the LSP class, so no distinction between SED-based classes will be made for them in figures and tallies. Only 37 FSRQs are of the ISP class and only 2 of the HSP class (BZB J0202+0849 and NVSS J025037+171209 associated with 3FGL J0202.3+0851 and 3FGL J0250.6+1713, respectively). As is visible in Figure 10, most ISP-FSRQs have softer spectra than the bulk of ISP-BL Lacs ($\langle\Gamma\rangle = 2.40 \pm 0.04$ versus 2.07 ± 0.02). In contrast, the two HSP-FSRQs have spectra ($\langle\Gamma\rangle = 2.01$) on par with the HSP-BL Lacs and thus much harder than the spectra of most other FSRQs. A similar trend is actually observed for BCUs, as can be seen in Figure 11, where the photon spectral index is plotted versus
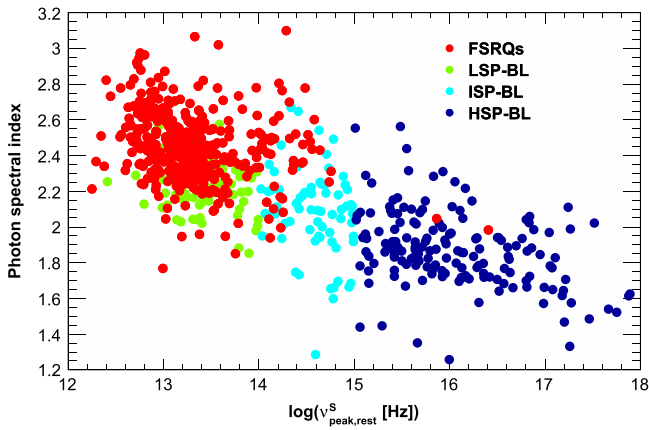
Figure 10. Photon index vs. frequency of the synchrotron peak $\nu^S_{peak,rest}$. Red: FSRQs, green: LSP-BL Lacs, light blue: ISP-BL Lacs, dark blue: HSP-BL Lacs.

Figure 11. Photon index vs. frequency of the synchrotron peak $\nu^S_{peak,obs}$ for blazars of unknown types (BCUs). For comparison, the orange bars show the average index for different bins in $\nu^S_{peak,rest}$ for blazars with known types, as displayed in Figure 10.

$\nu^S_{peak,obs}$. In this figure, the orange bars show the average index for different bins in $\nu^S_{peak,rest}$ obtained from the data plotted in Figure 10 for blazars of known types. This comparison supports the idea that BCUs with low ν^S_{peak} and high Γ are likely FSRQs, while the rest would mostly be BL Lacs.[86]

5.2. Redshift

Figure 12 compares the redshift distributions for FSRQs and BL Lacs in the 2LAC Clean Sample and those for the new 3LAC Clean-Sample sources (note that 50% of the BL Lacs do not have measured redshifts; see below). The distributions are fairly similar, although the newly detected FSRQs are located at a slightly higher redshift than the 2LAC ones ($\langle z \rangle = 1.33 \pm 0.08$ versus 1.17 ± 0.03). The maximum redshift for an FSRQ is still 3.1 (four FSRQs have $2.94 < z < 3.1$) and has not changed since the 1LAC. This trend allowed the conclusion that the number density of FSRQs grows dramatically up to redshift $\simeq 0.5$–2.0 and declines thereafter (Ajello et al. 2012).

The redshift distribution of new BL Lacs is somewhat narrower than that of the 2LAC sources, with a maximum near $z = 0.3$. The redshift distributions gradually spread out to higher redshifts when moving from HSP-BL Lacs to LSP-BL Lacs, a feature already seen in 2LAC. However, the HSP distribution extends to higher redshifts relative to 2LAC, with six HSP-BL Lacs having measured redshifts greater than 1 and one (MG4 J000800+4712) having a redshift greater than 2. Five of these six HSPs were already included in 2LAC but either lacked measured redshifts or were classified differently.

Among BL Lacs, 309 have a measured redshift, while 295 do not. The fraction of BL Lacs without redshift is 55%, 61%, and 40% for LSPs, ISPs, and HSPs, respectively. However, Shaw et al. (2013) have provided redshift constraints for 134 2LAC BL Lacs: upper limits from the absence of Lyα absorption for all of them and lower limits from non-detection of the host galaxy or from intervening absorption line systems for a subset of 54 objects. It was noted by these authors that the average lower limit exceeded the average measured redshift for BL Lacs, indicating that the measured redshifts are biased low. The allowed redshift ranges for the 54 sources with both lower
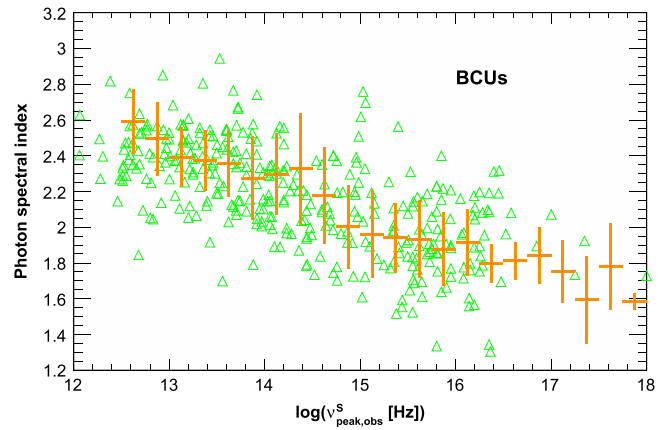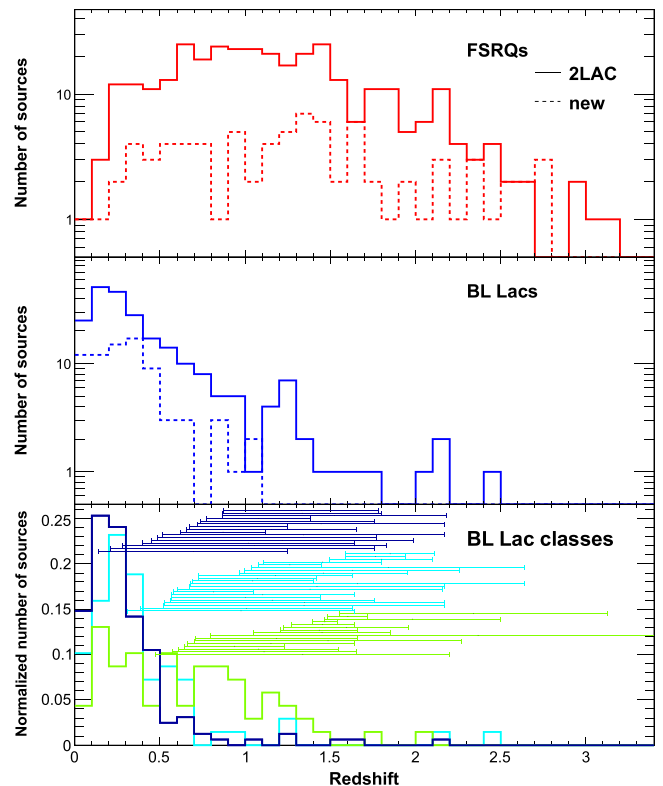
Figure 12. Redshift distributions (solid: 2LAC sources; dashed: new 3LAC sources) for FSRQs (top), BL Lacs (middle), and different types of BL Lacs (bottom): LSPs (green), ISPs (light blue), and HSPs (dark blue). The ranges between the lower and upper limits are also depicted in the bottom panel when both limits are available.

and upper limits are plotted in the bottom panel of Figure 12, confirming that they are in tension with the measured redshift distributions, in particular for HSPs. Kolmogorov–Smirnov tests (K–S) yield probabilities of 2×10^{-2}, 1×10^{-7}, and 1×10^{-6} that the distributions of measured redshifts and lower limits are drawn from the same underlying population for LSPs, ISPs and HSPs, respectively. The redshift ranges are very similar for the different subclasses and all cluster at high redshifts, with a median around $z = 1.2$. This is in good agreement with the predictions of Giommi et al. (2013), which

---

[86] Note that Figure 11 plots $\nu^S_{peak,obs}$ while Figure 10 shows $\nu^S_{peak,rest}$. The $(1 + z)$ correction, not applied in the latter case, is not expected to have a significant effect on the correlation strength.
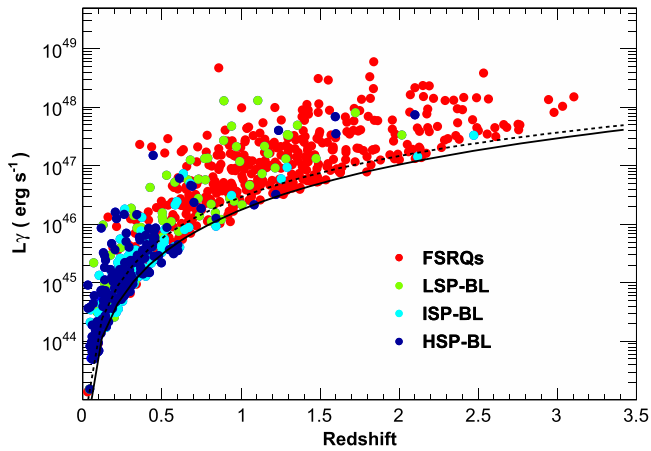
Figure 13. Gamma-ray luminosity vs. redshift. Red: FSRQs; green: LSP-BL Lacs; light blue: ISP-BL Lacs; dark blue: HSP-BL Lacs. The solid (dashed) curve represents the approximate detection limit for $\Gamma = 1.8$ ($\Gamma = 2.2$).

posit that most LAT-detected BL Lacs are actually FSRQs with their emission lines swamped by the non-thermal continuum hampering determination of their redshifts.

5.3. Luminosity

The gamma-ray luminosity has been computed from the 3FGL energy flux between 100 MeV and 100 GeV, obtained by spectral fitting. Figure 13 displays the gamma-ray luminosity plotted against redshift, together with the sensitivity limits calculated for $\Gamma = 1.8$ and 2.2. The Malmquist bias already reported in previous catalog papers is clearly visible. Low-luminosity BL Lacs ($<10^{45}$ erg s^{-1}) cannot be detected at $z > 0.4$. Note that sources with a luminosity greater than 5×10^{47} erg s^{-1} (64 are in 3LAC) could still be detected at $z > 3.2$.

Figure 14 shows the LAT photon index versus the gamma-ray luminosity for the different blazar classes. This correlation has been widely discussed in the context of the "blazar divide" or "blazar sequence" (Ghisellini et al. 2009, 2012; Meyer et al. 2012; Padovani et al. 2012; Finke 2013; Giommi et al. 2013). The features are similar to 2LAC, namely a branch of MAGNs separate from the bulk of blazars and a correlated trend of both luminosity and photon index as ν_{peak}^{S} decreases. Figure 15 shows the LAT photon index versus the gamma-ray luminosity for the 57 BL Lacs with both lower and upper limits on their redshifts or only upper limits (134 sources). Because of the bias mentioned above, the HSPs with both limits are more luminous on average than those with measured redshifts, thus populating a previously scarcely occupied area in the L_γ–Γ diagram. This observation has profound consequences for the blazar sequence. Note that Ajello et al. (2014) found a small but significant correlation between gamma-ray luminosity and spectral index when including the redshift constraints from Shaw et al. (2013).

5.4. Spectral Curvature

First observed for 3C 454.3 (Abdo et al. 2009b) early in the *Fermi* mission, a significant curvature in the energy spectra of many bright FSRQs and some bright LSP-/ISP-BL Lacs is now a well-established feature (Abdo et al. 2010f, 2010g). The break energy obtained from a broken power-law fit has been found to be remarkably constant as a function of flux, at least
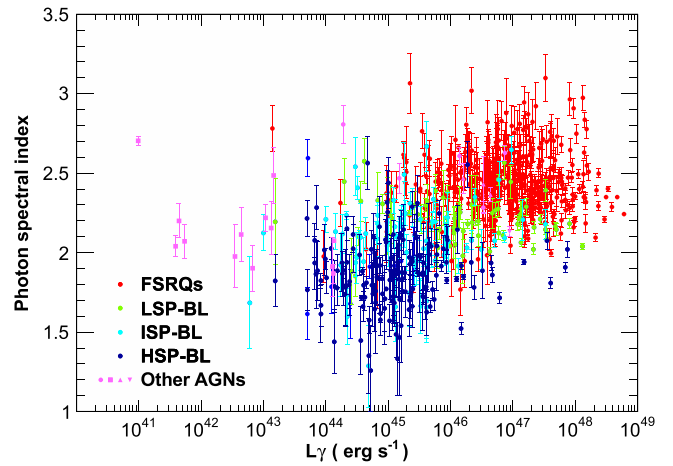
Figure 14. Photon index vs. gamma-ray luminosity. Red: FSRQs; green: LSP-BL Lacs; light blue: ISP-BL Lacs; dark blue: HSP-BL Lacs; magenta: other AGNs (circles: NLSy1s; squares: radio galaxies; up triangles: SSRQs; down triangles: AGNs of other types).
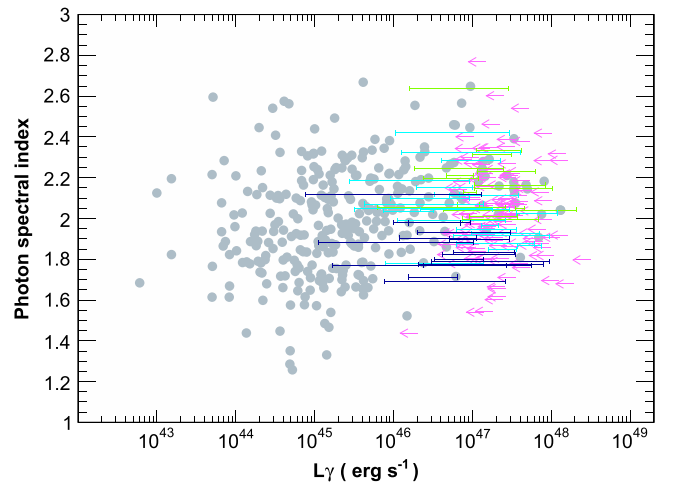
Figure 15. Photon index vs. gamma-ray luminosity for BL Lacs. Segments are plotted for sources having both lower- and upper-limits on their redshifts. Green: LSP-BL Lacs; light blue: ISP-BL Lacs; dark blue: HSP-BL Lacs. Magenta arrows are used for sources with upper limits only. BL Lacs with measured redshifts are depicted in gray, regardless of their SED classes.

for 3C 454.3 (Abdo et al. 2011). Several explanations have been proposed to account for this feature, including $\gamma\gamma$ attenuation from He II line photons (Poutanen & Stern 2010), intrinsic electron spectral breaks (Abdo et al. 2009b), Lyα scattering (Ackermann et al. 2010), Klein-Nishina effects taking place when jet electrons scatter BLR radiation in a near-equipartition approach (Cerruti et al. 2013), and hybrid scattering (Finke & Dermer 2010). The level of curvature has been observed to diminish during some flares (e.g., Pacciani et al. 2014).

In the 3FGL analysis, a switch is made from a power-law model to a log-parabola model whenever $TS_{curve} > 16$. The spectrum of the FSRQ 3C 454.3 cannot be well fitted with a log-parabola model, a power-law+exponential cutoff being a better model. A total of 91 FSRQs (57 in 2LAC), 32 BL Lacs (12 in 2LAC) and 8 BCUs show significant curvature at a confidence level >99%. Figure 16 shows the log-parabola β parameter plotted against gamma-ray flux and luminosity. At a given flux or luminosity the spectra of BL Lacs are less curved
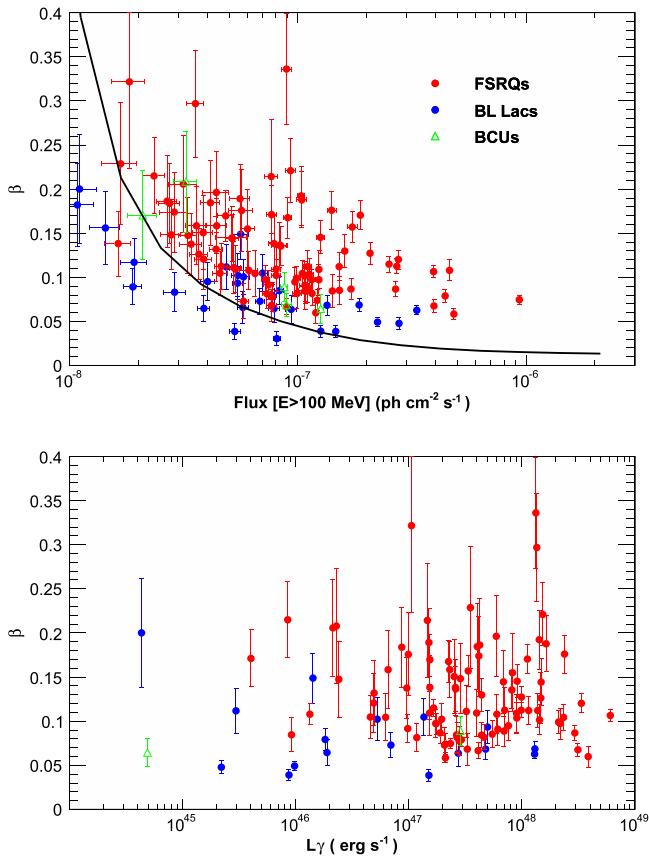
Figure 16. Log-parabola parameter β plotted vs. photon flux above 100 MeV (top, the line depicts the analysis limit $TS_{curve} = 16$ estimated for FSRQs) and gamma-ray luminosity (bottom). Red circles: FSRQs; blue circles: BL Lacs; green triangles: AGNs of unknown type.
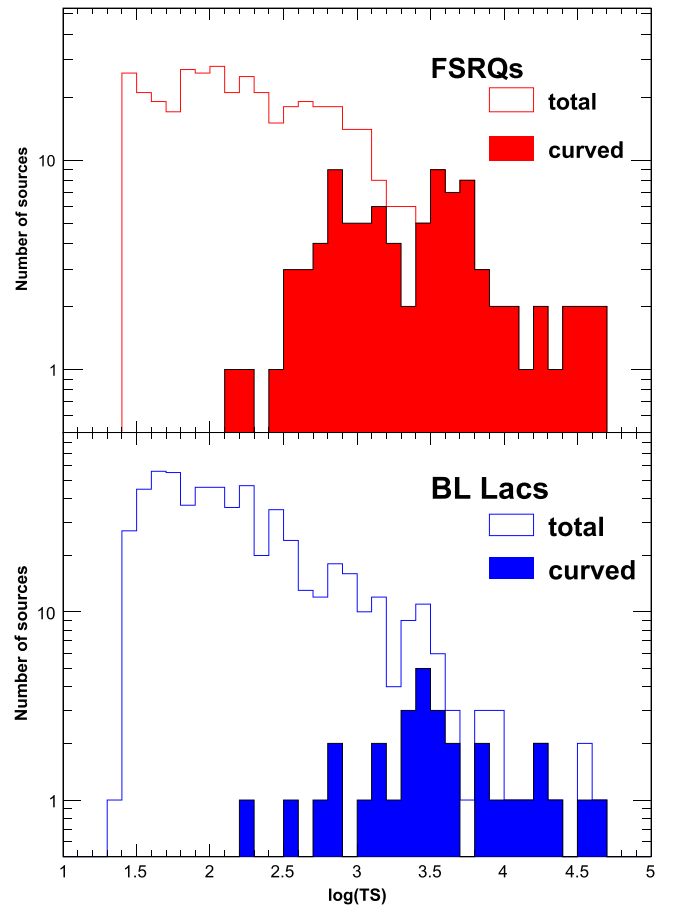

Figure 17. TS distributions of FSRQs (top) and BL Lacs (bottom). Solid histograms: total; filled histograms: sources with significant spectral curvatures.

than those of FSRQs, a feature already reported in 2LAC. Figure 17 compares the TS distributions for sources with curved spectra and those for the whole samples of FSRQs and BL Lacs. All bright FSRQs have curved spectra. For BL Lacs, the situation is more diverse. For BL Lac sources with TS > 1000, the fraction of sources with curved spectra is 16/23 (70%) for LSPs, 6/19 (32%) for ISPs, and 5/28 (18%) for HSPs. Note that because the latter have harder spectra than LSPs/ISPs on the average, potential spectral curvature is easier to detect for them. The average β is lower for HSPs (0.05) than for LSPs and ISPs (0.08).

5.5. Variability

Variability is a key feature of blazars. The 3FGL monthly averaged light curves provide a baseline reference against which other analyses can be cross-checked and enable cross-correlation studies with data obtained at other wavelengths. Although variability at essentially all timescales has been observed in blazars, the monthly binning represents a trade off between a shorter binning needed to resolve flares in bright sources and a longer binning required to detect faint sources. Even so, only 15 sources are detected in all 48 bins with monthly significance TS > 25, while this number becomes 46 if a relaxed condition TS > 4 is required. The 15 sources include 11 BL Lacs (7 HSPs), only 3 FSRQs (PKS 1510−08, 4C +55.17, B2 1520+31) and the radio galaxy NGC 1275. The 46 sources comprise 28 BL Lacs (14 HSPs),

15 FSRQs, one BCU and two radio galaxies, NGC 1275 and Centaurus A.

We will focus here on the variability index defined in Section 2; a value of 72.44 for this index indicating variability at the 99% confidence level (while the average index for non-variable sources is 47). Recall that this index can be large only for sources that are both variable and relatively bright. This index is plotted versus the synchrotron peak frequency in Figure 18. The features already reported in 2LAC are again visible, with a large fraction of FSRQs found to be variable (69%), with the fraction for BL Lacs much lower on average (23%) and with a steadily decreasing trend as ν_{peak}^S rises (39%, 23%, 15% for LSPs, ISPs and HSPs respectively). These fractions are quite similar to those reported in 2LAC, despite the larger population and longer time span of the light curves. A similar trend between variability index and ν_{peak}^S is observed for BCU (Figure 18 bottom), with 21% of them found to be variable.

The variability index is plotted versus TS for different bins in the photon spectral index in Figure 19. A distinct trend is visible: for a given TS the mean variability index increases as the spectrum becomes softer (the spectral index increases) up to $\Gamma = 2.4$ where this effect saturates. A net difference between FSRQs and BL Lacs is also apparent, confirming the behavior reported above. For $\Gamma > 2.2$, 72% of FSRQs and 25% of BL Lacs are variable above the 99% confidence level.
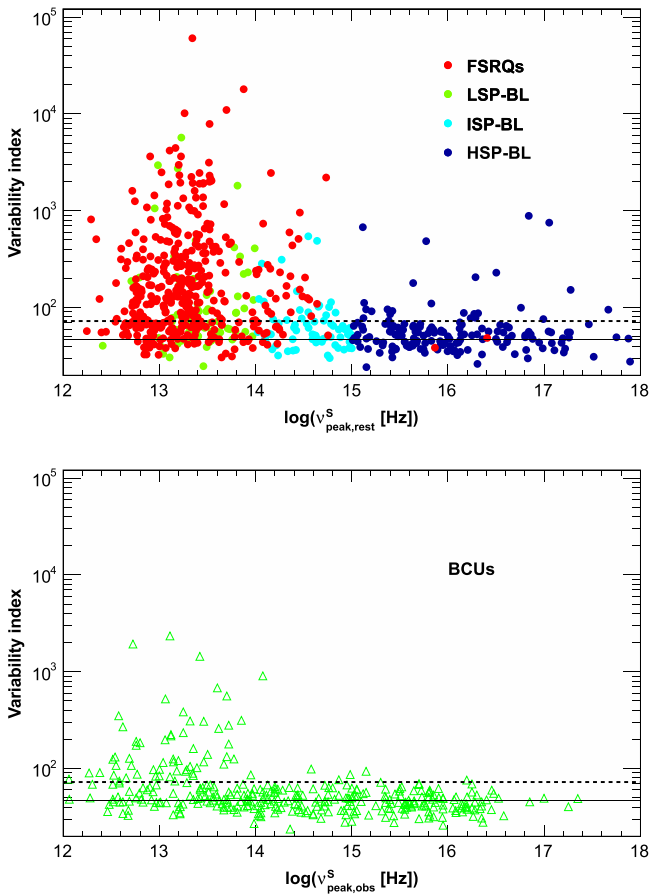
Figure 18. Top: variability index vs. rest-frame synchrotron peak frequency. Red: FSRQs; green: LSP-BL Lacs; light blue: ISP-BL Lacs; dark blue: HSP-BL Lacs. The solid line depicts the average variability index expected for non-variable sources. The dashed line corresponds to the 99% confidence level for a source to be variable. Bottom: variability index vs. observed synchrotron peak frequency for BCUs. The lines are the same as in the upper panel.

Figure 19. Top: variability index vs. TS for 6 bins in the photon spectral index Γ. Red: FSRQs; blue: BL Lacs. The dashed line corresponds to the 99% confidence level for a source to be variable.
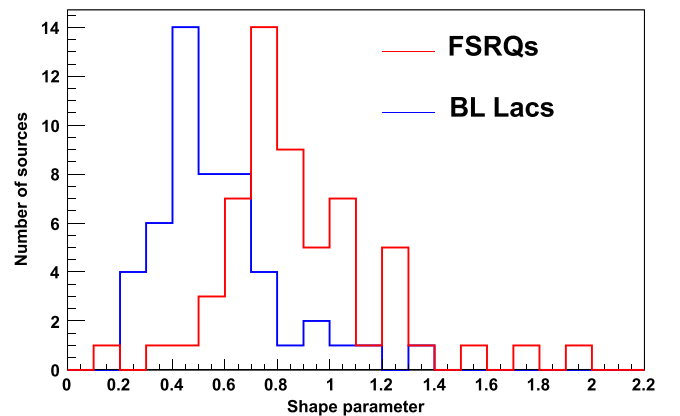
Figure 20. Log-normal-function shape parameters σ_{Ln} obtained from the monthly flux distributions of TS > 1000 FSRQs (red) and BL Lacs (blue).

For each source, we fit the distribution of monthly photon fluxes with a lognormal function

$$f_{Ln}(x) = \frac{N_{Ln}}{x \, \sigma_{Ln} \, \sqrt{2\pi}} \, \exp\left[-\frac{\left(\log(x) - u_{Ln}\right)^2}{2\sigma_{Ln}^2}\right], \qquad (1)$$

treating the flux values returned by the maximum-likelihood algorithm as if they were always significant, for simplicity. The lognormal function has commonly been used to model blazar flux distributions (e.g., Giebels & Degrange 2009; Tluczykont et al. 2010) and provides reasonable fits for most sources of our large sample. This distribution is expected for a process involving a large number of multiplicative, independently varying parameters. Figure 20 compares the distributions of shape parameters σ_{Ln} of FSRQs and BL Lacs that have been detected in 48 months above a TS of 1000 and had a monthly TS above 4 in at least 24 monthly periods. These distributions are distinct. The modes are about 0.8 and 0.4 for FSRQs and BL Lacs, respectively, confirming a larger flux variability for the former.

To further illustrate the detection variability and how the sample of brightest blazars renews itself, we compare the samples of brightest sources detected during the first and the last three-month periods of the 4 year-long data accumulation time. We applied the same TS cut used to select the LBAS sample (Abdo et al. 2009a), namely TS > 100 (simply adding up the monthly TS values). The two samples include similar numbers of sources (128 versus 134), but have only 50% (65) of the sources in common.

Table 8
3LAC Sources: Fluxes (High-latitude Sources)

3FGL Source Name (1)	Counterpart Name (2)	Radio Flux (mJy) (3)	Radio Flag (4)	X-ray Flux $(10^{-13}$ erg cm^{-2} s$^{-1})$ (5)	USNO B1 V mag (6)	SDSS V mag (7)	$\alpha_{\rm ox}$ (8)	$\alpha_{\rm ro}$ (9)
J0001.2−0748[a]	PMN J0001−0746	209.17	N	8.100	17.612	17.210	0.50	1.38

Notes. Column 1 is the 3FGL name, column 2 is the candidate counterpart name, column 3 is the radio flux measured in the survey indicated in column 4: N for NVSS (1.4 GHz), S for SUMSS (845 MHz), A for ATCA (20 GHz), P indicates PMN (4.8 GHz), and F indicates FIRST at 1.4 GHz. Column 5 is the X-ray flux between 0.1 and 2.4 keV from the RASS survey (Voges et al. 1999, 2000), columns 6–7 shows the USNO and SDSS V magnitudes, respectively. Columns 8 and 9 show the broadband indices between 5000 Å and 1 keV ($\alpha_{\rm ox}$) and between 5 GHz and 5000 Å ($\alpha_{\rm ro}$).
[a] Refers to sources in the Clean Sample.

(This table is available in its entirety in machine-readable form.)

6. MULTIWAVELENGTH PROPERTIES OF 3LAC SOURCES

It was shown in 2LAC that the LAT-detected blazars display on average larger radio fluxes than non-detected blazars and that they are all bright in the optical. Tables 8 and 9 give archival data for the 3LAC and low-latitude sources, respectively. Below we focus on the connection with the two neighboring bands, namely the hard X-rays and the VHE bands.

6.1. Sources Detected in Hard X-Rays

A total of 85 3LAC sources are in common with the *Swift* BAT 70 months survey (Baumgartner et al. 2013) in the 14–195 keV band performed between December 2004 and September 2010 (there were 47 in 2LAC). These 85 sources include 34 FSRQs with an average redshift of 1.37 ± 0.15. Only 9 BAT FSRQs are missing from 3LAC. The average LAT photon index of BAT-detected FSRQs is 2.57, i.e., somewhat softer than the overall average photon index of LAT FSRQs (2.43), a clue that their high-energy hump is located at slightly lower energies than the bulk of the FSRQs. Out of 37 BAT BL Lacs, 30 have now been detected with the LAT. These BL Lacs comprise 3 LSPs, 2 ISPs, and 19 HSPs, while 4 others are still unclassified. The large fraction of HSPs in this sample is not surprising, as the detection of LSPs and ISPs in the hard X-ray band is hampered by their SEDs exhibiting a valley between the low- and high-energy humps in this band (see Böttcher 2007). Figure 21 displays the LAT photon index versus the BAT photon index. Despite large error bars in the BAT photon index and non-simultaneous measurements, a remarkable anticorrelation (Pearson correlation factor −0.69), already noted in 2LAC, is observed. For the HSP-BL Lacs considered here, BAT probes the high-frequency (falling) part of the νF_ν synchrotron peak while the LAT probes the rising side of the inverse-Compton peak (assuming a leptonic scenario). For FSRQs, which are all LSPs in the common sample, BAT and LAT probe the rising and falling sides of the inverse-Compton peak, respectively.

It is also worth noting that 96 3LAC sources (5 Radio Galaxies, 53 FSRQs, 33 BL Lacs, 4 BCUs, 1 NLSy1) are present in the V38 *INTEGRAL* source catalog[87] (based on 3–200 keV data taken since 2002), which includes 540 AGNs located at $|b| > 10°$.

6.2. Sources Detected at Very High Energies

At the time of this writing, 56 AGNs that have been detected at TeV energies are listed in TeVCat.[88] Among them, 55 are present in 3FGL (see Table 10), which is a remarkable result underscoring the level of synergy that has now been achieved between the high-energy and VHE domains. Only HESS J1943+213 (a HSP BL Lac located at $b = -1°.3$, affecting the possible LAT detection) is still missing from the 3FGL, but an analysis of five years of LAT data resulted in a >1 GeV detection (Peter et al. 2014). There are 15 newly detected sources relative to 2FGL and six relative to the first *Fermi*-LAT catalog of sources above 10 GeV (1FHL, Ackermann et al. 2013, based on 3 years of data): SHBL J001355.9 −185406, 1ES 0229+200, 1ES 0347−121, RX J0847.1+1133 (aka RBS 0723), MS 1221.8+2452, and 1 H 1720+117.

Not all of the 55 sources are included in the 3LAC Clean Sample, either because they are located at low Galactic latitudes or because they are flagged for different reasons. The average photon index for HSP BL Lacs (representing 39 of the 55 AGNs) is 1.78 ± 0.13 (rms), slightly harder than that for the whole 3LAC sample (1.88 ± 0.22). Only 28 out of the 55 3FGL sources are seen to be variable in the LAT energy range at a significance greater than 99%.

7. DISCUSSION

7.1. Gamma-Ray Detected versus Non-detected Blazars

The blazars detected in gamma-rays after 4 years of LAT operation represent a sizeable fraction of the whole population of known blazars as listed in BZCAT. BZCAT represents an exhaustive list of sources ever classified as blazars but is by no means complete. Although a comparison between the gamma-ray detected and non-detected blazars within that sample has no strong statistical meaning in terms of relative weights, it is nevertheless useful to look for general trends.

The overall LAT-detected fraction is 24% (409/1707) for FSRQs, 44% (543/1221) for BL Lacs and 27% (59/221) for BCUs. A comparison between the normalized redshift distributions of the BZCAT blazars either included or not included in 3LAC is given in Figure 22, as well as the fraction of 3LAC sources relative to the total for a given redshift. A K–S test gives a probability of 3×10^{-8} that the two redshift distributions are drawn from the same population. The distribution shapes are quite similar for the two subsets

---

[87] http://www.isdc.unige.ch/integral/science/catalogue

[88] http://tevcat.uchicago.edu

Table 9
3LAC Sources: Fluxes (Low-latitude Sources)

3FGL Source	Counterpart	Radio Flux	Radio Flag	X-ray Flux (10^{-13} erg cm^{-2} s^{-1})
Name	Name	(mJy)		
(1)	(2)	(3)	(4)	(5)
J0012.4+7040	TXS 0008+704	639	N	⋯
J0014.6+6119	4C +60.01	4040	N	⋯
J0014.7+5802	1RXS J001442.2 +580201	7.7	N	104
J0015.7+5552	GB6 J0015+5551	85	N	152
J0035.9+5949	1ES 0033+595	148	N	318
J0047.0+5658	GB6 J0047+5657	190	N	⋯
J0047.9+5447	1RXS J004754.5 +544758	13.9	N	31.2
J0102.8+5825	TXS 0059+581	849	N	⋯
J0103.4+5336	1RXS J010325.9 +533721	30.9	N	63.7
J0109.8+6132	TXS 0106+612	305	N	⋯
J0110.2+6806	4C +67.04	1715	N	23.2
J0131.2+6120	1RXS J013106.4 +612035	19.7	N	471
J0131.3+5548	TXS 0128+554	175	N	21.9
J0135.0+6927	TXS 0130+691	202	N	⋯
J0137.8+5813	1RXS J013748.0 +581422	171	N	252
J0148.3+5200	GB6 J0148+5202	44.5	N	⋯
J0153.4+7114	TXS 0149+710	578	N	48.3
J0211.7+5402	TXS 0207+538	448	N	⋯
J0214.4+5143	TXS 0210+515	295	N	177
J0217.3+6209	TXS 0213+619	155	N	⋯
J0223.3+6820	NVSS J022304 +682154	20	N	⋯
J0223.5+6313	TXS 0219+628	124	N	⋯
J0228.5+6703	GB6 J0229+6706	27	N	⋯
J0241.3+6542	TXS 0237+655	191	N	41.6
J0250.6+5630	NVSS J025047 +562935	35.8	N	34.3
J0253.8+5104	NVSS J025357 +510256	429	N	⋯
J0302.0+5335	GB6 J0302+5331	187	N	⋯
J0303.6+4716	4C +47.08	963	N	⋯
J0304.9+6817	TXS 0259+681	1208	N	⋯
J0332.0+6308	GB6 J0331+6307	42.8	N	⋯
J0333.9+6538	TXS 0329+654	288	N	16.6
J0352.9+5655	GB6 J0353+5654	58.3	N	⋯
J0354.1+4643	B3 0350+465	759	N	⋯
J0358.8+6002	TXS 0354+599	953	N	38.8
J0418.5+3813	3C 111	7731	N	142
J0423.8+4150	4C +41.11	1756	N	⋯
J0425.2+6319	1RXS J042523.0 +632016	25.2	N	44.3
J0444.5+3425	B2 0441+34	238	N	⋯
J0501.8+3046	1RXS J050140.8 +304831	35.2	N	62.7
J0502.7+3438	MG2 J050234+3436	176	N	⋯
J0503.4+4522	1RXS J050339.8 +451715	34.9	N	75.2
J0512.2+2918	B2 0509+29	204	N	19.5
J0512.9+4038	B3 0509+406	877	N	⋯
J0517.4+4540	4C +45.08	1336	N	⋯
J0519.3+2746	4C +27.15	1702	N	⋯
J0521.7+2113	TXS 0518+211	530	N	60.2
J0526.0+4253	NVSS J052520 +425520	41.6	N	⋯
J0528.3+1815		21.5	N	163

Table 9
(Continued)

3FGL Source	Counterpart	Radio Flux	Radio Flag	X-ray Flux (10^{-13} erg cm^{-2} s^{-1})
Name	Name	(mJy)		
(1)	(2)	(3)	(4)	(5)
	1RXS J052829.6 +181657			
J0533.2+4822	TXS 0529+483	435	N	10.8
J0539.8+1434	TXS 0536+145	433	N	⋯
J0601.0+3837	B2 0557+38	705	N	⋯
J0603.8+2155	4C +22.12	2772	N	⋯
J0611.7+2759	GB6 J0611+2803	22.2	N	⋯
J0620.4+2644	RX J0620.6+2644	82.6	N	214
J0622.9+3326	B2 0619+33	240	N	⋯
J0623.3+3043	GB6 J0623+3045	52.2	N	⋯
J0631.2+2019	TXS 0628+203	317	N	⋯
J0640.0−1252	TXS 0637−128	225	N	312
J0641.8−0319	TXS 0639−032	820	N	⋯
J0643.2+0859	PMN J0643+0857	543	N	⋯
J0648.1+1606	1RXS J064814.1 +160708	25.0	N	34.6
J0648.8+1516	RX J0648.7+1516	64.8	N	381
J0648.8−1740	TXS 0646−176	1046	N	⋯
J0650.4−1636	PKS 0648−16	1778	N	⋯
J0650.5+2055	1RXS J065033.9 +205603	6.90	N	18.2
J0654.5+0926	RX J0654.3+0925	44.4	N	50.3
J0656.2−0323	TXS 0653−033	403	N	⋯
J0658.6+0636	NVSS J065844 +063711	25	N	⋯
J0700.0+1709	TXS 0657+172	648	N	⋯
J0700.2+1304	GB6 J0700+1304	78	N	⋯
J0702.7−1952	TXS 0700−197	527	N	⋯
J0709.7−0256	PMN J0709−0255	153	N	⋯
J0721.4+0404	PMN J0721+0406	313	N	12.9
J0723.2−0728	1RXS J072259.5−073131	85	N	150
J0725.8−0054	PKS 0723−008	1400	N	⋯
J0729.5−3127	NVSS J072922−313128	38	N	⋯
J0730.2−1141	PKS 0727−11	2760	N	⋯
J0730.5−0537	TXS 0728−054	168	N	⋯
J0744.1−3804	PMN J0743−3804	223	N	⋯
J0744.8−4028	PMN J0744−4032	65	A	⋯
J0746.6−0706	PMN J0746−0709	55	N	⋯
J0747.2−3311	PKS 0745−330	726	N	⋯
J0748.0−1639	TXS 0745−165	803	N	⋯
J0754.4−1148	TXS 0752−116	881	N	⋯
J0804.0−3629	NVSS J080405−362919	57	N	⋯
J0816.7−2421	PMN J0816−2421	191	N	⋯
J0825.8−3217	PKS 0823−321	393	N	⋯
J0825.9−2230	PKS 0823−223	520	N	36.9
J0828.8−2420	NVSS J082841−241850	249	N	⋯
J0841.3−3554	NVSS J084121−355506	74	N	⋯
J0845.1−5458	PMN J0845−5458	916	A	9.04
J0849.5−2912	NVSS J084922−291149	21.3	N	⋯
J0849.9−3540	PMN J0849−3541	376	N	⋯
J0852.6−5756	PMN J0852−5755	403	N	16.2
J0853.0−3654	NVSS J085310−365820	206	N	⋯
J0858.1−3130		5.6	N	111

Table 9
(Continued)

3FGL Source	Counterpart	Radio Flux	Radio Flag	X-ray Flux (10^{-13} erg cm^{-2} s^{-1})
Name	Name	(mJy)		
(1)	(2)	(3)	(4)	(5)
	1RXS J085802.6–313043			
J0904.8–3516	NVSS J090442–351423	279	N	…
J0904.8–5734	PKS 0903–57	1434	A	…
J0922.8–3959	PKS 0920–39	2616	N	16.6
J0940.7–6102	MRC 0939–608	491	A	…
J0956.7–6441	AT20G J095612–643928	70	A	…
J1005.0–4959	PMN J1006–5018	1177	A	…
J1015.2–4512	PMN J1014–4508	542	A	…
J1038.9–5311	MRC 1036–529	1675	A	…
J1047.8–6216	PMN J1047–6217	2285	A	…
J1051.5–6517	PKS 1049–650	220	A	…
J1103.9–5357	PKS 1101–536	539	A	…
J1123.2–6415	AT20G J112319–641735	280	A	…
J1136.6–6826	PKS 1133–681	585	A	…
J1229.8–5305	AT20G J122939–530332	56	A	…
J1233.9–5736	AT20G J123407–573552	59	A	…
J1256.1–5919	PMN J1256–5919	72	A	…
J1304.3–5535	PMN J1303–5540	905	A	…
J1308.1–6707	PKS 1304–668	611	A	…

Note. Column 1 is the 3FGL name, column 2 is the candidate counterpart name, column 3 is the radio flux measured in the survey indicated in column 4: N for NVSS (1.4 GHz), S for SUMSS (845 MHz), A for ATCA (20 GHz), P indicates PMN (4.8 GHz), and F indicates FIRST at 1.4 GHz. Column 5 is the X-ray flux between 0.1 and 2.4 keV from the RASS survey (Voges et al. 1999, 2000). Parameters in columns 6–9 of Table 8 have been omitted here since they are all blank for this sample.

(This table is available in machine-readable form.)

although the distribution for the blazars undetected by the LAT extends to significantly higher redshifts. Note that in contrast to TeV sources, the detection of high-z sources in the LAT energy range is not strongly affected by gamma–gamma attenuation from the EBL. The highest-redshift BZCAT sources (56 have $z > 3.1$ reaching $z = 5.47$) are still eluding detection by the LAT. Figure 23 compares the distributions of radio flux at 1.4 GHz, optical R-band magnitude, and X-ray (0.1–2.4 keV) flux between the BZCAT LAT-detected and non-LAT detected blazars, as well as the fraction of 3LAC sources relative to the total for a given flux. The gamma-ray loud blazars are somewhat brighter on average in all bands, confirming previous findings (Ackermann et al. 2011c; Lister et al. 2011). K–S tests give probabilities of 2×10^{-11}, 2×10^{-22}, and 4×10^{-19} that the 3LAC and non-3LAC distributions are drawn from the same population for the radio, optical, and X-ray cases, respectively. The fraction of gamma-ray loud blazars steadily decreases with decreasing radio, optical, and X-ray fluxes but remains non-negligible at the faint ends of the distributions. Figure 24 displays these radio-flux distributions broken down according to optical class. It is worth noting that some radio-
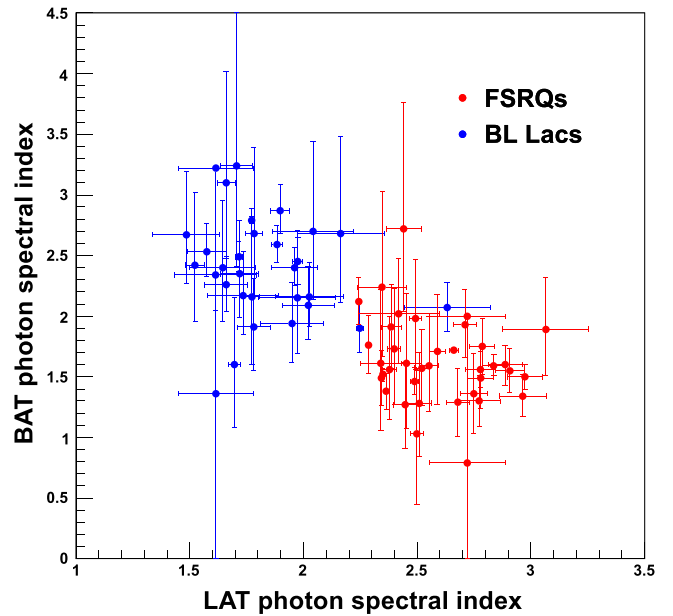
Figure 21. Photon spectral index in the BAT band (14–195 keV) vs. photon spectral index in the LAT band. Red: FSRQs; blue: BL Lacs.

bright blazars have not yet been detected by the LAT and that the detection fraction drops off with decreasing radio flux in a log-linear fashion.

In Figure 25, the gamma-ray energy flux is plotted against the radio flux density at 1.4 GHz. A significant correlation is observed (Pearson correlation factor = 0.52), confirming the findings in Ghirlanda et al. (2011) and Ackermann et al. (2011b). The best-fit power-law relation is $F_\gamma \simeq F_r^{0.34 \pm 0.05}$. Note that a stronger correlation is found if one uses the gamma-ray photon flux instead of the energy flux (Pearson correlation factor = 0.72), but this results from the photon-index dependence of the flux detection threshold in the gamma-ray band already discussed above. Radio-bright FSRQs have soft spectra in the LAT band and thus high detection thresholds, reinforcing the apparent correlation between radio flux density and gamma-ray fluxes.

The absence of a strong difference in the redshift or flux distributions between the detected and non-detected sets of blazars supports the conjecture that they belong to the same population of sources intermittently shining in gamma-rays. One can test the assumption that the fraction of non-detected sources is consistent with the variability properties assessed in Section 5.5 from the monthly light curves or if longer-term variability is required. Selecting BZCAT sources with high radio luminosity, $F_\nu > 316$ mJy, we obtain the gamma-ray energy flux distribution plotted in Figure 26. While 401 sources have been detected by the LAT, 706 sources with radio flux in the same range have not. Computing the dispersion of the 48 month flux average expected from the lognormal monthly flux distributions presented in Section 5.5 and using the central-limit theorem, one obtains a typical value of 20% (illustrated by the blue arrows in Figure 26). This dispersion is obviously insufficient to account for the observed ratio between detected and non-detected blazars. Considerably longer timescales than those probed over the 4 year period (associated with physical or geometrical parameter(s) governing the observed jet gamma-ray/radio loudness ratio) must be in play. Since the fraction of

Table 10
Properties of the 3FGL VHE AGNs

3FGL Name	VHE Name	Source Class	SED Type	Redshift	Spectral Index	Variability Index
J0013.9–1853	SHBL J001355.9–185406	BLL	HSP	0.094	1.935 ± 0.167	36.46
J0033.6–1921	KUV 00311–1938	BLL	HSP	0.610	1.715 ± 0.035	64.62
J0035.9+5949[a]	1ES 0033+595	BLL	HSP	⋯	1.898 ± 0.042	69.55
J0136.5+3905	RGB J0136+391	BLL	HSP	⋯	1.696 ± 0.025	62.30
J0152.6+0148	RGB J0152+017	BLL	HSP	0.080	1.887 ± 0.103	51.76
J0222.6+4301	3C 66A	BLL	ISP	0.444	1.880 ± 0.017	885.04
J0232.8+2016	1ES 0229+200	BLL	HSP	0.139	2.025 ± 0.150	49.16
J0303.4–2407	PKS 0301–243	BLL	HSP	0.260	1.918 ± 0.022	676.85
J0316.6+4119	IC 310	RDG	HSP	0.019	1.902 ± 0.143	38.74
J0319.8+1847	RBS 0413	BLL	HSP	0.190	1.572 ± 0.102	76.33
J0319.8+4130	NGC 1275	RDG	ISP	0.018	1.985 ± 0.014	622.21
J0349.2–1158	1ES 0347–121	BLL	HSP	⋯	1.734 ± 0.156	44.26
J0416.8+0104	1ES 0414+009	BLL	HSP	0.287	1.745 ± 0.114	55.85
J0449.4–4350	PKS 0447–439	BLL	HSP	0.205	1.849 ± 0.015	230.17
J0508.0+6736	1ES 0502+675	BLL	HSP	0.340	1.523 ± 0.040	77.94
J0521.7+2113[a]	VER J0521+211	BLL	ISP	0.108	1.923 ± 0.024	239.79
J0550.6–3217	PKS 0548–322	BLL	HSP	0.069	1.615 ± 0.164	48.44
J0648.9+1516[a]	VER J0648+152	BLL	HSP	0.179	1.831 ± 0.071	36.04
J0650.7+2503	1ES 0647+250	BLL	HSP	0.203	1.721 ± 0.047	63.85
J0710.3+5908	RGB J0710+591	BLL	HSP	0.125	1.661 ± 0.094	55.54
J0721.9+7120	S5 0716+714	BLL	ISP	0.127	1.948 ± 0.012	1818.04
J0809.8+5218	1ES 0806+524	BLL	HSP	0.138	1.876 ± 0.024	485.15
J0847.1+1134	RX J0847.1+1133	BLL	HSP	0.199	1.740 ± 0.115	44.90
J1010.2–3120	1RXS J101015.9–311909	BLL	HSP	0.143	1.576 ± 0.100	86.30
J1015.0+4925	1ES 1011+496	BLL	HSP	0.212	1.833 ± 0.017	110.46
J1103.5–2329	1ES 1101–232	BLL	HSP	0.186	1.645 ± 0.145	36.51
J1104.4+3812	Markarian 421	BLL	HSP	0.031	1.772 ± 0.008	755.10
J1136.6+7009	Markarian 180	BLL	HSP	0.045	1.824 ± 0.047	43.04
J1217.8+3007	1ES 1215+303	BLL	HSP	0.130	1.974 ± 0.023	206.36
J1221.3+3010	1ES 1218+304	BLL	HSP	0.182	1.660 ± 0.038	92.45
J1221.4+2814	W Comae	BLL	ISP	0.103	2.102 ± 0.027	204.24
J1224.5+2436	MS 1221.8+2452	BLL	HSP	0.218	1.887 ± 0.094	54.19
J1224.9+2122	4C +21.35	FSRQ	LSP	0.435	2.185 ± 0.012	18067.45
J1230.9+1224	M 87	RDG	LSP	0.004	2.040 ± 0.066	54.28
J1256.1–0547	3C 279	FSRQ	LSP	0.536	2.233 ± 0.014	4198.44
J1314.7–4237	1ES 1312–423	BLL	HSP	⋯	2.082 ± 0.214	45.02
J1325.4–4301	Centaurus A	RDG	⋯	0.002	2.703 ± 0.029	59.33
J1427.0+2347	PKS 1424+240	BLL	ISP	⋯	1.760 ± 0.022	210.25
J1428.5+4240	H 1426+428	BLL	HSP	0.129	1.575 ± 0.085	59.46
J1442.8+1200	1ES 1440+122	BLL	HSP	0.163	1.796 ± 0.117	50.46
J1512.8–0906	PKS 1510–089	FSRQ	LSP	0.360	2.305 ± 0.009	11014.00
J1517.6–2422	AP Lib	BLL	LSP	0.048	2.112 ± 0.026	60.31
J1555.7+1111	PG 1553+113	BLL	HSP	⋯	1.604 ± 0.025	123.55
J1653.9+3945	Markarian 501	BLL	HSP	0.034	1.716 ± 0.016	251.47
J1725.0+1152	1 H 1720+117	BLL	HSP	⋯	1.885 ± 0.045	79.88
J1728.3+5013	1ES 1727+502	BLL	HSP	0.055	1.960 ± 0.065	54.08
J1743.9+1934	1ES 1741+196	BLL	HSP	0.084	1.777 ± 0.108	38.27
J2000.0+6509	1ES 1959+650	BLL	HSP	0.047	1.883 ± 0.022	158.37
J2001.1+4352[a]	MAGIC J2001+435	BLL	ISP	⋯	1.971 ± 0.022	341.11
J2009.3–4849	PKS 2005–489	BLL	⋯	0.071	1.773 ± 0.031	131.06
J2158.8–3013	PKS 2155–304	BLL	HSP	0.116	1.750 ± 0.018	618.50
J2202.7+4217	BL Lacertae	BLL	ISP	0.069	2.161 ± 0.017	2340.22
J2250.1+3825	B3 2247+381	BLL	HSP	0.119	1.912 ± 0.074	52.42
J2347.0+5142[a]	1ES 2344+514	BLL	HSP	0.044	1.782 ± 0.039	100.97
J2359.3–3038	H 2356–309	BLL	HSP	0.165	2.022 ± 0.115	40.97

Note.
[a] Refers to low-latitude sources (not in 3LAC).

(This table is available in machine-readable form.)

LAT-detected FSRQs relative to the BZCAT total is less than that for BL Lacs (20% versus 40%), a larger amplitude variability of FSRQs is necessary to allow sources currently below the threshold to shine in gamma-rays at LAT-detection levels. This feature (a larger variability of FSRQs relative to BL Lacs) is compatible with the observations mentioned above.
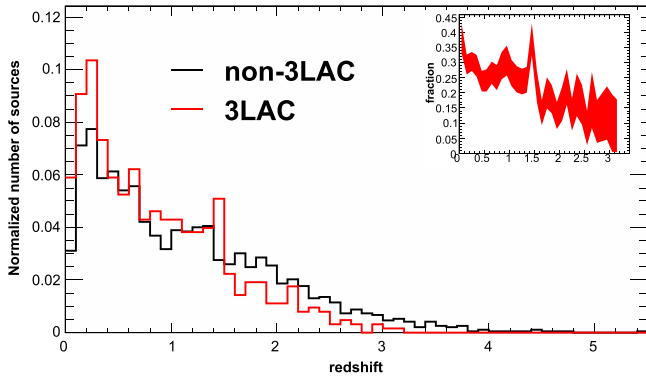
Figure 22. Redshift distributions for 3LAC (red) and non-3LAC (black) BZCAT sources. The inset shows the fraction of 3LAC sources relative to the total for a given redshift.

Figure 24. Radio flux density at 1.4 GHz for 3LAC (dashed) and non-3LAC (solid) BZCAT sources. The inset displays the fraction of 3LAC sources relative to the total. Red: FSRQs; blue: BL Lacs.

Figure 23. From top to bottom: radio flux density at 1.4 GHz, optical R magnitude, X-ray flux (0.1–2.4 keV) distributions for 3LAC (red), and non-3LAC (black) BZCAT sources. The insets show the fraction of 3LAC sources relative to the total for a given flux.
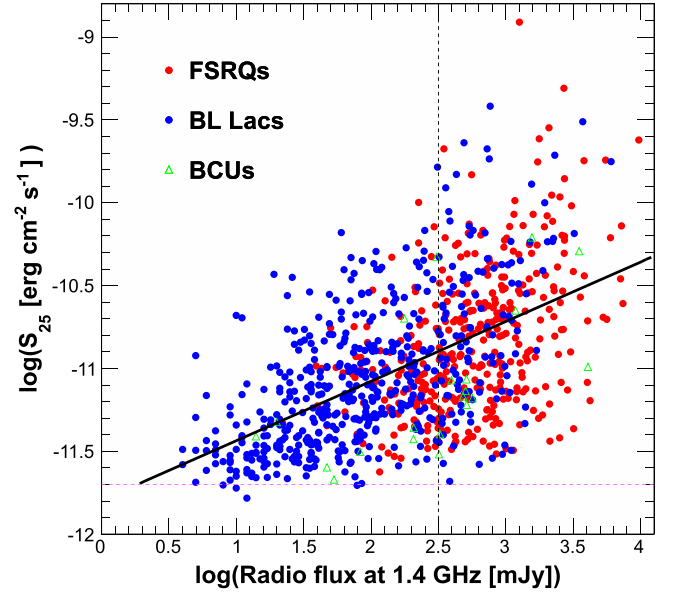
Figure 25. Gamma-ray energy flux plotted against the radio flux density at 1.4 GHz. Red circles: FSRQs; blue circles: BL Lacs; green triangles: BCUs. The horizontal dashed line depicts the approximate LAT detection limit and the vertical dashed line the lower limit of the selection used in Figure 26. The solid line depicts the result of the power-law fit described in the text.

7.2. Compton Dominance

We consider here the Compton dominance ratio (CD), i.e., the ratio between the peak νF_ν for the high- and low-frequency SED humps, computed as described in Abdo et al. (2010a) and Finke (2013). The top panel of Figure 27 shows this ratio plotted against ν_{peak}^S (similar to Figure 5 in Finke (2013), using 2LAC data). It is found that logCD has a mean and rms of (0.60, 0.65) for FSRQs and (−0.11, 0.48) for LSP-BL Lacs, while it has (−0.39, 0.42) for ISP-BL Lacs, and (−0.78, 0.39) for HSP-BL Lacs.

The spread in CD is partially driven by variability. The SED data are not simultaneous, especially for FSRQs, as some of them have displayed flux variations in gamma-rays greater than two orders of magnitude during the *Fermi* mission. However, as shown in Figure 26, the overall effect of variability on the mean gamma-ray flux is quite limited (see more below).

The combination of different beaming factors for the two humps (as expected if inverse-Compton off an external
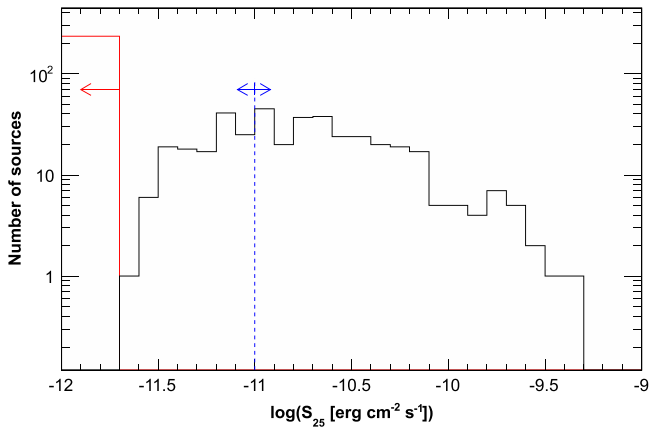
Figure 26. Distribution of gamma-ray energy flux for LAT-detected blazars with radio flux density at 1.4 GHz above 316 mJy (black). The arrows represent the 1σ deviation expected for the 48 month average flux, assuming a log-normal energy-flux distribution with $\sigma_{Ln} = 1$ and a mean of 10^{-11} erg cm^{-2} s^{-1}. The red upper-limit histogram schematically represents the 706 non-LAT detected BZCAT blazars with radio fluxes in the same range.
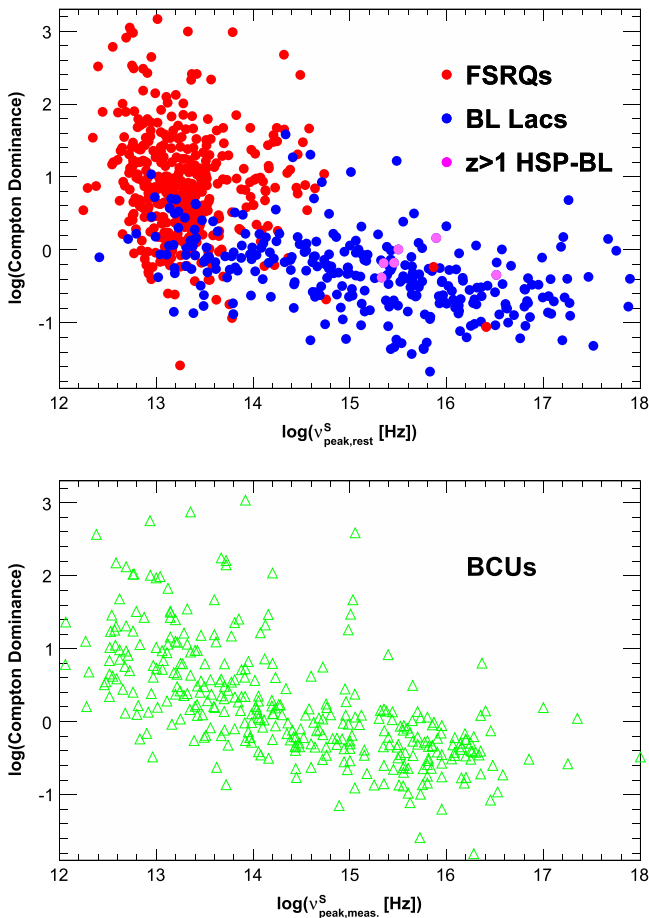
Figure 27. Top: Compton dominance vs. rest-frame peak synchrotron position. Red: FSRQs; blue: BL Lacs; magenta: $z > 1$ HSP-BL Lacs. Bottom: Compton dominance vs. observer-frame peak synchrotron position for BCUs.

radiation field is important, e.g., in FSRQs, Dermer [1995]) and different jet angles relative to the line of sight within the 3LAC sample are likely to add to this spread. FSRQs have on average higher Compton dominance than BL Lacs, which exhibit a trend toward lower CD values with increasing ν_{peak}^S. Interestingly, as can be seen from Figure [27], the six luminous HSP-BL
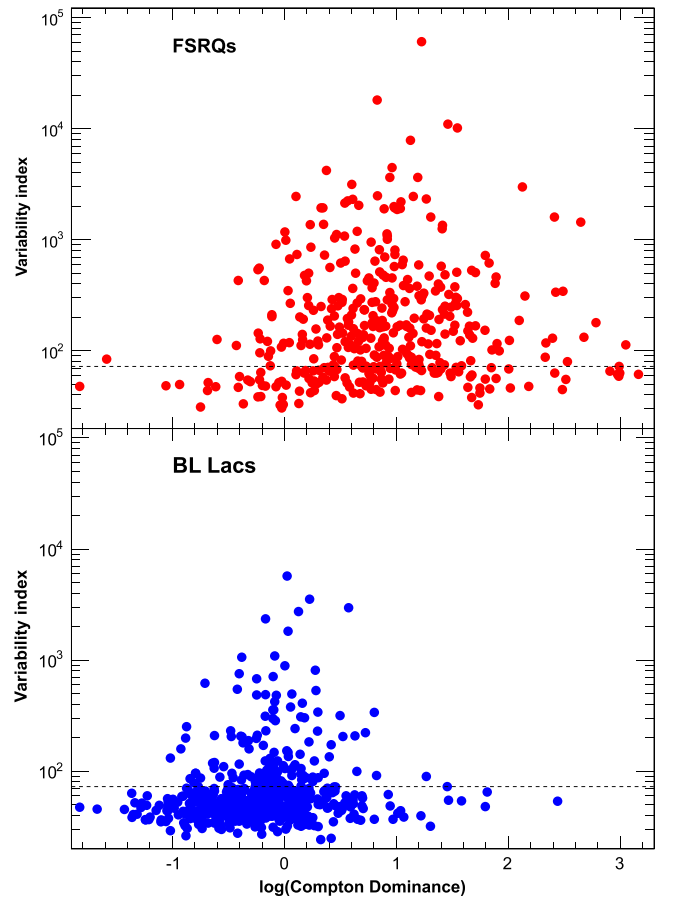
Figure 28. Variability index vs. Compton dominance. Top: FSRQs; bottom: BL Lacs. The dashed line corresponds to the 99% confidence level for a source to be variable.

Lacs located at redshifts greater than 1 show CD values very similar to those located at low redshifts. These objects have a mean photon index of 1.94, comparable to the mean value of the whole HSP sample (1.88). Together, these features indicate that the overall SED shape of HSP-BL Lacs is not strongly dependent on redshift and thus neither on luminosity.

The lower panel of Figure [27] shows the corresponding plot for BCUs. Although ν_{peak}^S has not been corrected by $(1 + z)$ for most sources as their redshifts are unknown, the observed trend is very similar to that of blazars with known types.

An interesting point regards the comparison between LSP-BL Lacs and FSRQs. The gamma-ray properties of the former being intermediate between those of FSRQs and of HSP-BL Lacs, they could be FSRQs "in disguise" where the emission lines are swamped by a strong non-thermal continuum as suggested by Giommi et al. ([2013]). Figure [28] shows the variability index plotted against CD for FSRQs and BL Lacs. It is seen that the regions occupied by the BL Lacs and FSRQs have moderate overlap.

7.3. log N–log S

Figure [29] shows the log N–log S (S being the gamma-ray energy flux and N the cumulative number of sources above this flux) plot for the full 1LAC, 2LAC, and 3LAC catalogs, as well as for FSRQs, BL Lacs, and BCUs in the respective Clean Samples, uncorrected for coverage. Note that the LAT limiting
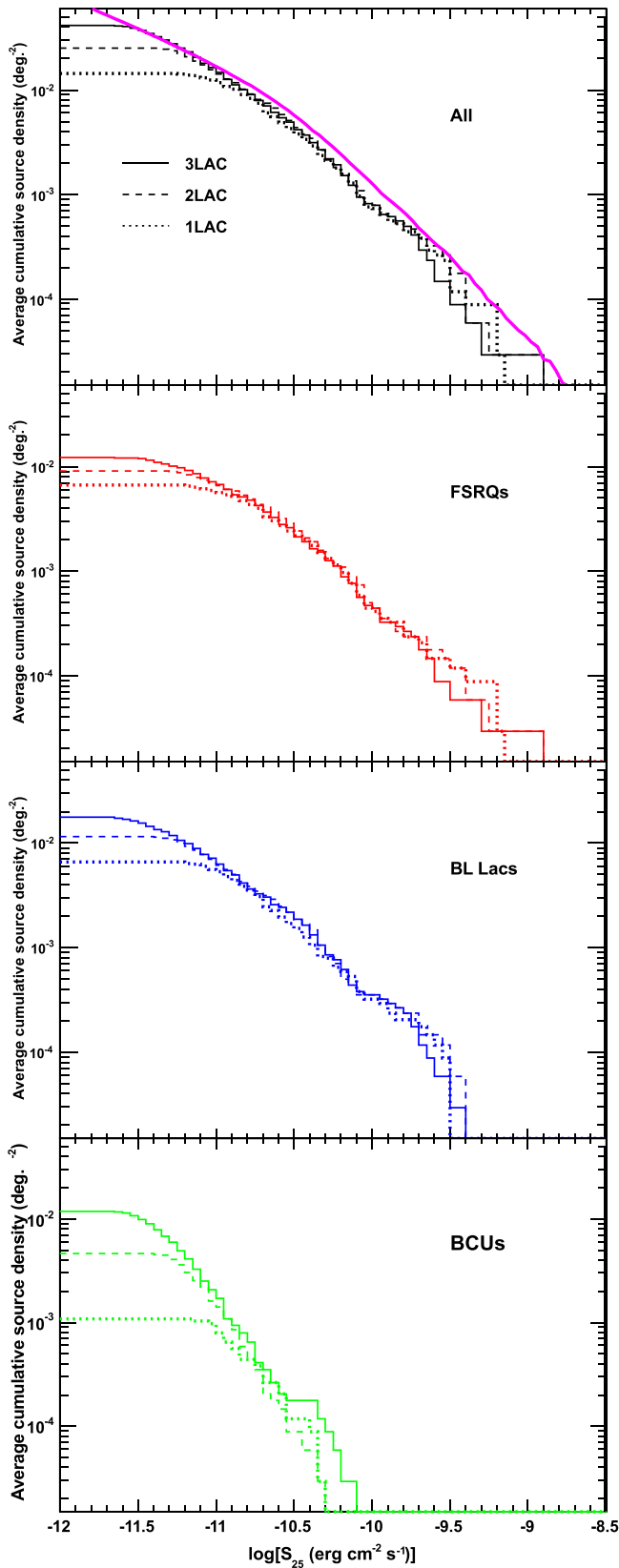
Figure 29. Cumulative energy flux distributions (uncorrected for non-uniform sensitivity and detection/association efficiency) for blazars in Clean Samples. Solid: 3LAC; dashed: 2LAC; dotted: 1LAC. Top: Total. The magenta curve corresponds to the predictions derived from Ackermann et al. (2012d). Second: FSRQs. Third: BL Lacs. Bottom: blazars of unknown type.

energy flux is essentially independent of the photon index and thus of the blazar class as illustrated in Figure 9. A steady increase in the number of sources is observed for all classes, with the 3LAC being roughly in line with extrapolations from the 2LAC. Power-law fits performed on the 3LAC distributions between somewhat arbitrary energy-flux limits (see Figure 29) yield slopes of 1.23, 1.22, and 1.09 for the whole set, FSRQs, and BL Lacs, respectively. Integrating the energy-flux distributions above 100 MeV in the range 10^{-11}–10^{-9} erg cm^{-2} s^{-1} gives gamma-ray intensities for all sources and FSRQs of 1.4×10^{-6} GeV cm^{-2} s^{-1} sr^{-1} and 4.7×10^{-7} GeV cm^{-2} s^{-1} sr^{-1}, respectively. These results can be compared to those obtained in assessing the diffuse gamma-ray emission (Ackermann et al. 2012d) : the intensity for all resolved sources at $|b| > 20°$ is estimated to be 9.5×10^{-7} GeV cm^{-2} s^{-1} sr^{-1}. This corresponds to 1.2×10^{-6} GeV cm^{-2} s^{-1} sr^{-1} after applying the geometrical correction (from $|b| > 20°$ to $|b| > 10°$), in reasonable agreement with the 3LAC-based estimate.

8. CONCLUSIONS

We have presented the third catalog of LAT-detected AGNs (3LAC), based on 48 months of LAT data. This is an improvement over the 1LAC (11 months of data) and 2LAC (24 months of data) in terms of data quality and analysis methods. Key results from the 3LAC sample include the following.

1. An increase of 71% in the number of blazars relative to 2LAC stems from the two-fold increase in exposure and the use of improved counterpart catalogs. The energy-flux distributions of the different blazar populations are in good agreement with extrapolation from earlier catalogs.

2. A significant increase of the non-blazar population is found with respect to previous catalogs. The new sources include: two FRIIs (Pictor A, 3C 303), three FRIs (4C +39.12, 3C 189, 3C 264 plus one possible association, Fornax A), and four SSRQs (TXS 0826+091, 4C +0.40, 3C 275.1, 3C 286). However, other sources (3C 407, NGC 6951, NGC 6814) reported in previous catalogs are now missing.

3. A large fraction (>75%) of *Swift* hard X-ray BAT-detected blazars and all but one TeV-detected AGNs have now been detected by the *Fermi*-LAT.

4. The most distant 3LAC blazar is the same as in 1LAC and 2LAC: PKS 0537−286, lying at $z = 3.1$. Many BZCAT blazars at higher redshifts have yet to be detected by the LAT. Although 50% of the BL Lacs still do not have measured redshifts, upper limits have recently been obtained for 134 2LAC sources and lower limits as well for 57 of them. These constraints indicate that the measured redshifts are biased low for BL Lacs. Using the luminosities derived from these constraints, the sources populate a previously scarcely occupied area in the L_γ–Γ diagram, somewhat undermining the picture of the blazar sequence.

5. Along the same lines, a few rare outliers (four high-luminosity HSP BL Lacs and two HSP FSRQs) are included in the 3LAC, while they were missing in 2LAC.

The high-luminosity HSP-BL Lacs exhibit Compton dominance values similar to the bulk of that class.

6. The main properties of blazars previously reported in 1LAC and 2LAC are confirmed. The average photon index, gamma-ray luminosity, flux variability, and spectral curvature monotonically evolve from FSRQs to HSP BL Lacs, with LSP- and ISP-BL Lacs showing intermediate behavior.

7. The fraction of 3LAC blazars in the total population of blazars listed in BZCAT remains non-negligible even at the faint ends of the BZCAT-blazar radio, optical, and X-ray flux distributions, which is a clue that even the faintest, and thus possibly all, known blazars could eventually shine in gamma-rays at LAT-detection levels. A larger fraction (44%) of the known BL Lacs than FSRQs (24%) has been detected so far. The duty cycle of FSRQs appears to be longer than four years if most of them are eventual gamma-ray emitters.

The 3LAC catalog is intended to serve as a valuable resource for a better understanding of the gamma-ray loud AGNs. The next LAT AGN catalog will benefit from the improved Pass 8 data selection and IRFs (Atwood et al. 2013). Pass 8 is the result of a comprehensive revision of the entire event-level analysis, based on the experience gained in the prime phase of the mission. The gain in effective area at the low end of the LAT energy range will be particularly notable. The 4LAC catalog is thus expected to include a non-incremental number of new, especially soft-spectrum AGNs.

APPENDIX
NOTE ON CONVENTION FOR SOURCE ASSOCIATION COUNTERPART NOMENCLATURE

In this paper we have tentatively adopted a history-based rationale for the names of blazar and other AGN source counterparts associated with 3LAC sources, as reported in the 3FGL catalog FITS file.[89] This naming rationale is already working as the source name resolver in NED (NASA/IPAC Extragalactic Database), and was already in use, in part, in the 2LAC paper. It is possible to retrieve an approximate knowledge about the chronological appearance of a radio/optical/X-ray point source in past catalogs thanks to NED, Simbad-Vizier, and ADS databases. The best-known (widely used) naming rationale is more arbitrary and more difficult to reconstruct, it suffers more from subjectivity, and applies only to a minority of the brightest blazars/AGNs.

AGNs and blazars were first discovered as optical non-starlike/nebula objects (i.e., galaxies, M, NGC, IC catalogs published between 1781 and 1905), as optical variable stars (Argelander designations for BL Lac, W Com, AP Lib), unusually optically blue starlike objects (Ton, PHL, Mkn catalogs all published between about 1957 and 1974), and subsequent catalogs of normal or peculiar galaxies (CGCG, MCG, CGPG, UGC, Ark, Zw/I-V, Tol catalogs all published between about 1961 and 1976). Subsequent optical catalogs like the PG, PB, US, SBS, PGC, LEDA, HS, and SDSS are

---

[89] http://fermi.gsfc.nasa.gov/ssc/data/access/lat/4yr_catalog/gll_psc_v16.fit

also used in our 3LAC associations naming rationale.[90] In parallel, most blazars and AGNs were detected as new discrete point sources in the first radio observations and surveys (sources like Vir A, Cen A, Cen B, Per A, etc., in the early 1950s, then the 3C, CTA, PKS, 4C, O[+letter], VRO, NRAO, AO, DA, B2, GC, S1/S2/S3 catalogs all published between about 1959 and 1974). Other subsequent radio catalogs like the TXS, 5C, S4/S5, MRC, B3 (all about 1974–1985) and MG1/MG2/MG4, 87 GB, 6C/7C, JVAS, PMN, EF, CJ2, FIRST, Cul, GB6, FBQS, WN, NVSS, CLASS, IERS, SUMSS, CRATES (all after 1986) are also used in our work. Other catalogs of interest at IR or UV frequencies for purposes of 3LAC association names are the KUV, *EUVE*, 2MASSi, and 2MASS. Additional blazars that are fainter in the radio/optical bands were discovered directly thanks to the first X-ray observations (2A, 4U, XRS, EXO, H/1 H, MS, 1E, 1ES, 2E, and RX all published from about 1978 to the mid 1990s). The subsequent (after 1997) reanalysis and catalog constructions based mainly on the *ROSAT* survey and radio-X-ray source cross correlations are also used in the 3LAC (RGB, RBS, RHS, 1RXS, XSS catalogs).

The most common source counterpart roots in 3LAC associations have origins in the 3C, 4C, PKS, O[+letter], B2, S2/S3/S5, TXS, MG1/MG2, PMN, GB6, SDSS, 1ES, RX, RBS, and 1RXS catalogs. PKS (Parkes Radio Catalog, Australia) chronologically is the source name preferred for southern celestial radio sources, over almost all the other epoch-overlapping radio catalogs. The survey for northern celestial radio sources at Parkes likely started after the more easily observable southern sources, therefore later than the O [+letter] (Ohio State University Radio Survey Catalog, USA) observations, and certainly after the 3C and 4C catalogs. The procedure for selecting source counterpart names is tuned to the most-used/known criterion for the most famous sources (for example OJ 287 instead of PKS 0851+202/ PG 0851+202, but PKS 0735+17 instead of OI 158 / DA 237). Other famous blazars/AGN sources are more likely to follow the best-known criterion (example: Cen A is more frequently used than NGC 5128, even though this galaxy was first discovered in the NGC catalog). For the northern celestial hemisphere the preferred radio source name chosen following the approximate chronological criterion follows the sequence of radio catalogs reported above (3C, CTA, 4C, O[+letter], NRAO, AO, DA, B2, GC, S1/S2/S3, TXS, MG1/MG2/MG4, etc.). Some catalog designations (like the 87 GB and rare optical names) are essentially not used in the 3LAC. RBG names have been preferred to RBS and 1RXS names, and the NVSS names have been preferred to the SDSS names. We do not have a preference between GB6 and RX names or between RBS and 1RXS names, as all are being used arbitrarily.

REFERENCES

Abdo, A. A., Ackermann, M., Agudo, I., et al. 2010a, ApJ, 716, 30
Abdo, A. A., Ackermann, M., Ajello, M., et al. 2009a, ApJ, 700, 597
Abdo, A. A., Ackermann, M., Ajello, M., et al. 2009b, ApJ, 699, 817
Abdo, A. A., Ackermann, M., Ajello, M., et al. 2009c, ApJ, 699, 31
Abdo, A. A., Ackermann, M., Ajello, M., et al. 2009d, ApJ, 707, 55
Abdo, A. A., Ackermann, M., Ajello, M., et al. 2009e, ApJS, 183, 46
Abdo, A. A., Ackermann, M., Ajello, M., et al. 2010b, Sci, 328, 725

Abdo, A. A., Ackermann, M., Ajello, M., et al. 2010c, ApJ, 723, 1082
Abdo, A. A., Ackermann, M., Ajello, M., et al. 2010d, ApJS, 188, 405
Abdo, A. A., Ackermann, M., Ajello, M., et al. 2010e, ApJ, 720, 912
Abdo, A. A., Ackermann, M., Ajello, M., et al. 2010f, ApJ, 710, 1271
Abdo, A. A., Ackermann, M., Ajello, M., et al. 2010g, ApJ, 715, 429
Abdo, A. A., Ackermann, M., Ajello, M., et al. 2011, ApJL, 733, L26+
Abramowski, A., Acero, F., Akhperjanian, A. G., et al. 2013, A&A, 552, A118
Ackermann, M., Ajello, M., Allafort, A., et al. 2011a, ApJ, 741, 30
Ackermann, M., Ajello, M., Allafort, A., et al. 2011b, ApJ, 741, 30
Ackermann, M., Ajello, M., Allafort, A., et al. 2011c, ApJ, 743, 171
Ackermann, M., Ajello, M., Allafort, A., et al. 2012a, ApJ, 755, 164
Ackermann, M., Ajello, M., Allafort, A., et al. 2012b, ApJ, 747, 104
Ackermann, M., Ajello, M., Allafort, A., et al. 2012c, Sci, 338, 1190
Ackermann, M., Ajello, M., Allafort, A., et al. 2013, ApJS, 209, 34
Ackermann, M., Ajello, M., Allafort, A., et al. 2015, ApJ, 806, 1
Ackermann, M., Ajello, M., Atwood, W. B., et al. 2012d, ApJ, 750, 3
Ackermann, M., Ajello, M., Baldini, L., et al. 2010, ApJ, 721, 1383
Ahn, C. P., Alexandroff, R., Allende Prieto, C., et al. 2012, ApJS, 203, 21
Ajello, M., Romani, R. W., Gasparrini, D., et al. 2014, ApJ, 780, 73
Ajello, M., Shaw, M. S., Romani, R. W., et al. 2012, ApJ, 751, 108
Aleksić, J., Ansoldi, S., Antonelli, L. A., et al. 2014, Sci, 346, 1080
Arsioli, B., Fraga, B., Giommi, P., Padovani, P., & Marrese, M. 2015, arXiv:1504.02801
Atwood, W., Albert, A., Baldini, L., et al. 2013, arXiv:1303.3514
Atwood, W. B., Abdo, A. A., Ackermann, M., et al. 2009, ApJ, 697, 1071
Baumgartner, W. H., Tueller, J., Markwardt, C. B., et al. 2013, ApJS, 207, 19
Böttcher, M. 2007, Ap&SS, 309, 95
Brown, A. M., & Adams, J. 2012, MNRAS, 421, 2303
Burgess, A. M., & Hunstead, R. W. 2006, AJ, 131, 114
Cerruti, M., Dermer, C. D., Lott, B., Boisson, C., & Zech, A. 2013, ApJL, 771, L4
Cheung, C. C. 2007, in ASP Conf. Ser. 373, The Central Engine of Active Galactic Nuclei, ed. L. C. Ho & J.-W. Wang (San Francisco, CA: ASP), 255
Chiang, J. 2012, in Advances in Machine Learning and Data Mining for Astronomy, ed. M. J. Way et al. (London: Taylor & Francis)
Ciprini, S., & Thompson, D. J. 2013, in IV Fermi Symp. Proc., eConf C121028 17, arXiv:1303.4054
Condon, J. J., Cotton, W. D., Greisen, E. W., et al. 1998, AJ, 115, 1693
D'Abrusco, R., Massaro, F., Ajello, M., et al. 2012, ApJ, 748, 68
D'Abrusco, R., Massaro, F., Paggi, A., et al. 2013, ApJS, 206, 12
D'Ammando, F., Orienti, M., Finke, J., et al. 2012, MNRAS, 426, 317
D'Ammando, F., Orienti, M., Finke, J., et al. 2013, MNRAS, 436, 191
de Ruiter, H. R., Arp, H. C., & Willis, A. G. 1977, A&AS, 28, 211
Dermer, C. D. 1995, ApJL, 446, L63
Donato, D., & Perkins, J. 2011, ATel, 3452, 1
Fanaroff, B. L., & Riley, J. M. 1974, MNRAS, 167, 31P
Fermi-LAT Collaboration 2015, arXiv:1501.02003
Finke, J. D. 2013, ApJ, 763, 134
Finke, J. D., & Dermer, C. D. 2010, ApJL, 714, L303
Fomalont, E. B., Ebneter, K. A., van Breugel, W. J. M., & Ekers, R. D. 1989, ApJ, 346, 17
Georganopoulos, M., Sambruna, R. M., Kazanas, D., et al. 2008, ApJL, 686, L5
Ghirlanda, G., Ghisellini, G., Tavecchio, F., Foschini, L., & Bonnoli, G. 2011, MNRAS, 413, 852
Ghisellini, G., Haardt, F., della Ceca, R., Volonteri, M., & Sbarrato, T. 2013, MNRAS, 432, 2818
Ghisellini, G., Maraschi, L., & Tavecchio, F. 2009, MNRAS, 396, L105
Ghisellini, G., Tavecchio, F., Foschini, L., et al. 2012, MNRAS, 425, 1371
Giebels, B., & Degrange, B. 2009, A&A, 503, 797
Giommi, P., Padovani, P., & Polenta, G. 2013, MNRAS, 431, 1914
Giommi, P., Polenta, G., Lähteenmäki, A., et al. 2012, A&A, 541, A160
Giovannini, G., Cotton, W. D., Feretti, L., Lara, L., & Venturi, T. 2001, ApJ, 552, 508
Grandi, P., Torresi, E., & Stanghellini, C. 2012, ApJL, 751, L3
Hartman, R. C., Bertsch, D. L., Bloom, S. D., et al. 1999, ApJS, 123, 79
Hartman, R. C., Kadler, M., & Tueller, J. 2008, ApJ, 688, 852
Hayashida, M., Stawarz, Ł., Cheung, C. C., et al. 2013, ApJ, 779, 131
Healey, S. E., Romani, R. W., Taylor, G. B., et al. 2007, ApJS, 171, 61
Hough, D. H. 2013, European Physical Journal Web of Conferences, 61, 08009
Jones, D. H., Read, M. A., Saunders, W., et al. 2009, MNRAS, 399, 683
Kadler, M., Eisenacher, D., Ros, E., et al. 2012a, A&A, 538, L1
Kataoka, J., Stawarz, Ł., Cheung, C. C., et al. 2010, ApJ, 715, 554
Kataoka, J., Stawarz, L., Takahashi, Y., et al. 2011, ApJ, 740, 29
Katsuta, J., Tanaka, Y. T., Stawarz, L., et al. 2013, A&A, 550, A66
Kovalev, Y. Y., Aller, H. D., Aller, M. F., et al. 2009, ApJL, 696, L17

---

[90] For all catalogs cited in this appendix, the pertaining literature and bibliographic references can be directly retrieved through the NED web database at ned.ipac.caltech.edu/cgi-bin/catdef?prefix=XYZ, where "XYZ" is the catalog/list code or prefix (e.g., "B2").

Kovalev, Y. Y., Petrov, L., Fomalont, E. B., & Gordon, D. 2007, AJ, 133, 1236
Laing, R. A., Riley, J. M., & Longair, M. S. 1983, MNRAS, 204, 151
Landt, H. 2012, MNRAS, 423, L84
Lenain, J.-P., Ricci, C., Türler, M., Dorner, D., & Walter, R. 2010, A&A, 524, A72
Lister, M. L., Aller, M., Aller, H., et al. 2011, ApJ, 742, 27
Lister, M. L., Aller, M. F., Aller, H. D., et al. 2013, AJ, 146, 120
Lister, M. L., Homan, D. C., Kadler, M., et al. 2009, ApJL, 696, L22
Lonsdale, C., Conrow, T., Evans, T., et al. 1998, in IAU Symp. 179, New Horizons from Multi-Wavelength Sky Surveys, ed. B. J. McLean et al. (Dordrecht: Kluwer Academic Publishers), 450-+
Masci, F. J., Condon, J. J., Barlow, T. A., et al. 2001, PASP, 113, 10
Massaro, E., Giommi, P., Leto, C., et al. 2009, A&A, 495, 691
Massaro, E., Perri, M., Giommi, P., & Nesci, R. 2004, A&A, 413, 489
Massaro, F., D'Abrusco, R., Tosti, G., et al. 2012, ApJ, 750, 138
Mauch, T., Murphy, T., Buttery, H. J., et al. 2003, MNRAS, 342, 1117
McConville, W., Ostorero, L., Moderski, R., et al. 2011, ApJ, 738, 148
Meyer, E. T., Fossati, G., Georganopoulos, M., & Lister, M. L. 2012, ApJL, 752, L4
Mukherjee, R., Halpern, J., Mirabal, N., & Gotthelf, E. V. 2002, ApJ, 574, 693
Murphy, T., Sadler, E. M., Ekers, R. D., et al. 2010, MNRAS, 402, 2403
Myers, S. T., Jackson, N. J., Browne, I. W. A., et al. 2003, MNRAS, 341, 1
Neronov, A., Semikoz, D., & Vovk, I. 2010, A&A, 519, L6
Nolan, P. L., Abdo, A. A., Ackermann, M., et al. 2012, ApJS, 199, 31
Ojha, R., Kadler, M., Böck, M., et al. 2010, A&A, 519, A45
Pacciani, L., Tavecchio, F., Donnarumma, I., et al. 2014, ApJ, 790, 45
Padovani, P., Giommi, P., & Rau, A. 2012, MNRAS, 422, L48
Planck Collaboration, Ade, P. A. R., Aghanim, N., et al. 2011, A&A, 536, A7
Planck Collaboration, Ade, P. A. R., Aghanim, N., et al. 2014, A&A, 571, A16
Peter, D., Domainko, W., Sanchez, D. A., van der Wel, A., & Gässler, W. 2014, A&A, 571, A41
Petrov, L., Mahony, E. K., & Edwards, P. G. 2013, MNRAS, 432, 1294
Piner, B. G., Pushkarev, A. B., Kovalev, Y. Y., et al. 2012, ApJ, 758, 84
Poutanen, J., & Stern, B. 2010, ApJL, 717, L118
Prestage, R. M., & Peacock, J. A. 1983, MNRAS, 204, 355
Ruan, J. J., Anderson, S. F., Plotkin, R. M., et al. 2014, ApJ, 797, 19
Shaw, M. S., Romani, R. W., Cotter, G., et al. 2013, ApJ, 764, 135
Sokolovsky, K. V., Schinzel, F. K., Tanaka, Y. T., et al. 2014, A&A, 565, 26
Sreekumar, P., Bertsch, D. L., Hartman, R. C., Nolan, P. L., & Thompson, D. J. 1999, APh, 11, 221
Strong, A. W., & Bignami, G. F. 1983, ApJ, 274, 549
Sutherland, W., & Saunders, W. 1992, MNRAS, 259, 413
Takeuchi, Y., Kataoka, J., Stawarz, Ł., et al. 2012, ApJ, 749, 66
Tanaka, Y. T., Cutini, S., Ciprini, S., et al. 2014, ATel, 6529, 1
Tavecchio, F., Pacciani, L., Donnarumma, I., et al. 2013, MNRAS, 435, L24
Teng, S. H., Mushotzky, R. F., Sambruna, R. M., Davis, D. S., & Reynolds, C. S. 2011, ApJ, 742, 66
Tluczykont, M., Bernardini, E., Satalecka, K., et al. 2010, A&A, 524, A48
Véron-Cetty, M.-P., & Véron, P. 2010, A&A, 518, A10+
Voges, W., Aschenbach, B., Boller, T., et al. 1999, A&A, 349, 389
Voges, W., Aschenbach, B., Boller, T., et al. 2000, yCat, 9029, 0
Wilkinson, P. N., Akujor, C. E., Cornwell, T. J., & Saikia, D. J. 1991, MNRAS, 248, 86
Wright, A. E., Griffith, M. R., Hunt, A. J., et al. 1996, ApJS, 103, 145